Brigham Young University

BYU ScholarsArchive

Relative Infrasound Calibration of Microphones with Application to Outdoor Vector Intensity Measurements

Francisco Javier Irarrazabal Oliva
Brigham Young University

Relative Infrasound Calibration of Microphones with Application to

Outdoor Vector Intensity Measurements

Francisco J. Irarrazabal Oliva

A thesis submitted to the faculty of
Brigham Young University
in partial fulfillment of the requirements for the degree of

Master of Science

Kent L. Gee, Chair
Scott D. Sommerfeldt
Timothy W. Leishman

Department of Physics and Astronomy

Brigham Young University

ABSTRACT

Relative Infrasound Calibration of Microphones with Application to
Outdoor Vector Intensity Measurements

Francisco J. Irarrazabal Oliva
Department of Physics and Astronomy, BYU
Master of Science

This thesis describes the phase and amplitude correction of 12.7 mm diameter, Type-1 microphones for three frequency bands, including within the infrasound regime, and its application to acoustic measurements. Previous data stem from acoustic intensity measurements using two-dimensional, four-microphone probes, which emphasized the requirement of having the acoustic phase and amplitude difference be much greater than the interchannel mismatch. Although correcting the amplitude/phase is well-known, obtaining the necessary transfer functions in the infrasound regime is challenging because (1) signal-to-noise ratios are often poor, (2) long measurement times are required for averaging, and (3) microphone responses vary significantly across these low frequencies. In this paper, a convenient infrasound source previously studied for infrasound adverse effects on humans is intended for performing a relative calibration.

Table of Contents

iii

iv

List of Figures

List of Tables

1 Chapter 1: Introduction

1.1 Introduction

Acoustic intensity measurement has great relevance in the study of acoustic source characteristics. Acoustic intensity is a vector quantity defined as the product of the particle velocity and pressure[1,2]. Intensity measurements help map the acoustic field generated by a source, which is important in several areas such as noise control, product development, construction, musical instruments and halls, and vibration analysis. The application of these energy methods is used, for instance, in the national standard ANSI S12.12 and the international standard ISO 3740 to determine the sound power level.

Acoustic intensity measurements using ½" free-field microphones have been improved using the phase and amplitude gradient estimator or PAGE method[3]. As is shown in Figure 1.1.1, the main advantage of the improvement is to extend the frequency range for a given probe spacing. Typically, PAGE reduces bias errors near and beyond the spatial Nyquist frequency, which is defined as the frequency with wavelength equal to twice the microphone spacing. Infrasound sources commonly give continuous energy into the low-audio region, making the vector intensity frequency extension highly convenient. This thesis shows the PAGE method's application into infrasonic acoustic intensity measurements.

Previous research by Gee et al. [4] showed the PAGE method's application benefits on intensity levels calculation, as shown in Figure 1.1.1. The acoustic intensity magnitude was measured for multiple probe spacings, as is shown on the right side. The bias errors increase as the probe spacing increases for the traditional method. The PAGE method showed almost zero bias errors for all microphone spacing in plane wave fields. Also, the phase unwrapping is displayed in

1

the bottom-left part of Figure 1.1.1. The complex pressure phase unwrapping help to avoid a 180˚ phase shift (dotted lines) and erroneous intensity directions.
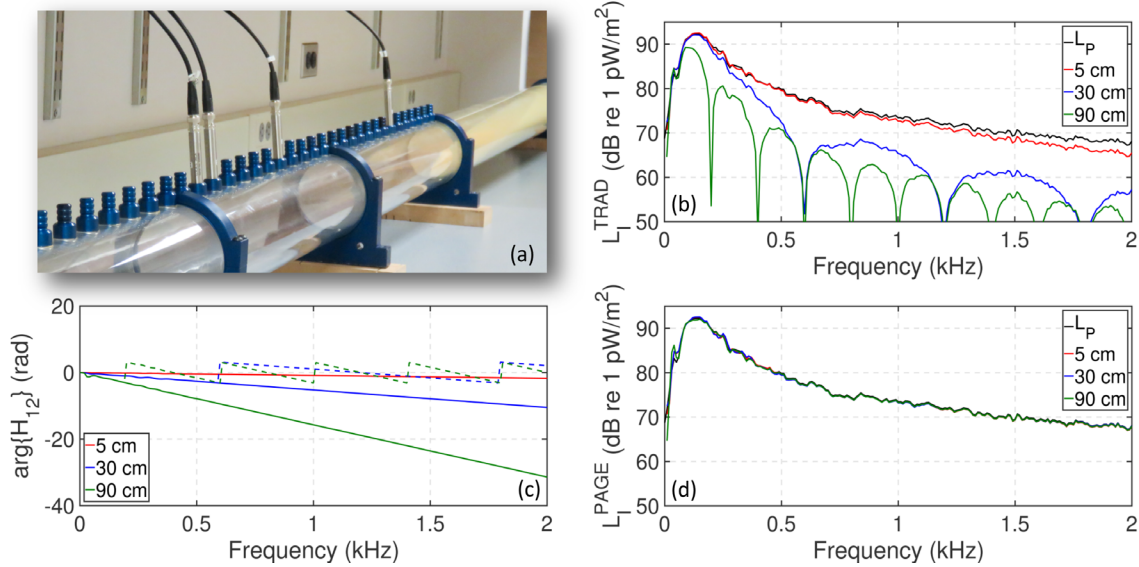
Figure 1.1.1 Main advantage given by the PAGE method. The bias error near and beyond the spatial Nyquist limit is improved. (a) Experiment setup in the planewave tube. (b) Intensity level for multiple microphone spacing using the traditional method. (c) Phase unwrapping. (d) Intensity level for multiple microphone spacing using the PAGE method.

Measuring infrasound using free-field microphones is challenging since most microphones have a frequency response higher than the infrasonic limits. Besides, the need for more than one sensor introduces the instrument mismatch complication when measuring infrasonic intensity. Finally, noise present in the acoustic field is a challenge because it affects the signal coherence. This thesis focuses on measuring the infrasonic instrument mismatch and applying the calibration to outdoor intensity measurements.

2

1.2 Intensity

The acoustic intensity is the time-averaged product of the particle velocity and pressure. Acoustic intensity is a vector quantity having direction and magnitude and can be used to measure the acoustic energy flow. In this section, the traditional and PAGE methods are explained.

1.2.1 Traditional method

The traditional estimation of acoustic intensity involves measuring the sound pressure and particle velocity simultaneously at the same position. The pressure-based method for vector intensity uses an array of microphones and then finite sums and differences between microphones' pressures to obtain the required pressure and particle velocity[5,6]. Euler's equation establishes the connection between the pressure gradient and the particle velocity.

$$\frac{\partial u}{\partial t} = -\frac{1}{\rho_0}\nabla p \qquad \qquad \textit{Equation 1.2-1}$$

The pressure across the microphone array is directly averaged taking the pressure at every microphone, for simplicity let us take two microphones separated by a distance "d".

$$p \approx \frac{p_1 + p_2}{2} \qquad \qquad \textit{Equation 1.2-2}$$

Vector intensity measurements using a particle velocity sensor are also possible, but when flow is present, such as wind outdoors, these sensors are less robust than microphones[7,8,9].

The intensity calculation is then completed by the product between the averaged amplitude of the pressure and the estimated complex conjugate of the particle velocity. As it was shown by Thomas et al.[3] the intensity in the frequency domain is given by:

$$\hat{I}_c = -\frac{j}{\rho_0 \omega} p_0 \widehat{\nabla p} \qquad \qquad \textit{Equation 1.2-3}$$

Equation 1.2-3 gives the complex intensity, the hut means time average, and p_0 is the pressure at the center of the array.

3

1.2.2 PAGE method

The Phase and Amplitude Gradient Estimator (PAGE) method estimate the least-squares gradient of the sound pressure phase across a multimicrophone probe to calculate the acoustic intensity. The calculations are made with the phase gradient and amplitude obtained from the microphones. Complex pressure is expressed as a function of position, r, by:

$$\boldsymbol{p(r)} = \boldsymbol{P(r)}e^{-j\phi(r)} \qquad \text{Equation 1.2-4}$$

The bold notation indicates a vector quantity. The separation vector for every possible microphone pair is arranged into a matrix where every row corresponds to each separation vector. Then, the matrix is represented according to

$$\boldsymbol{X} = [\boldsymbol{r_2} - \boldsymbol{r_1}, \dots, \boldsymbol{r_N} - \boldsymbol{r_{N-1}}]^T \qquad \text{Equation 1.2-5}$$

On the other hand, the vector of pairwise phase differences is given by the pairwise transfer function as follows:

$$\Delta\boldsymbol{\phi} = -[arg\{\boldsymbol{H_{1,2}}\}, \dots, arg\{\boldsymbol{H_{N-1,N}}\}]^T \qquad \text{Equation 1.2-6}$$

Particle velocity is obtained from the estimation of pressure gradient according to Euler's equation. Then, the time-average active intensity (defined as the real part of the complex intensity given by Equation 1.2-3) can be found as

$$\widehat{\boldsymbol{I}}_a = \frac{1}{\omega\rho_0} P_0^2 \widehat{\nabla\phi} \qquad \text{Equation 1.2-7}$$

P_0^2 is the mean-square pressure. This is the pressure at the center or the average of the pressure magnitudes across the probe. The least-squares phase gradient is calculated from N microphones with $r_{1\dots N}$ positions as

$$\widehat{\nabla\phi} = (\boldsymbol{X}^T\boldsymbol{X})^{-1}\boldsymbol{X}^T\Delta(\boldsymbol{\phi}) \qquad \text{Equation 1.2-8}$$

4

The PAGE method reduces the active intensity bias errors up to the Nyquist frequency. For signals with a smooth variation of $\nabla\phi$ in the frequency domain, the phase can be unwrapped, extending the upper-frequency limit above the Nyquist frequency.

Only two-dimensional probes will be used in this research for the intensity measurements. However, the vector quantity considers three coordinates, padding with zeroes the coordinate not contained in the probe plane. The intensity direction using this type of arrays is estimated by taking the four-quadrant arctangent of the non-zero components' ratio.

$$I_{dir} = atan2(I_y, I_x)$$ *Equation 1.2-9*

1.3 Intensity errors:

The pressure-based vector intensity method has limitations. The first source of error is the instrument amplitude and phase mismatch. The second source is the bias errors produced when the sensor spacing is no longer small relative to a wavelength. The finite sums between microphone data show bias error when the spacing distance is near or larger than half wavelength for a given frequency (spatial Nyquist frequency limit).

The acoustic phase of a plane wave increases as the microphone spacing increases for a given wavelength. Figure 1.3.1 shows the effect of microphone spacing for a given wavelength. A larger spacing distance helps to reduce the random error due to microphone mismatch by improving the ratio of instrument mismatch and acoustic phase, as is shown in Figure 1.3.2. According with Equation 1.3-1 the error level for the intensity magnitude[2] is inversely proportional to wavenumber, k, and proportional to the instrument mismatch, φ.

5
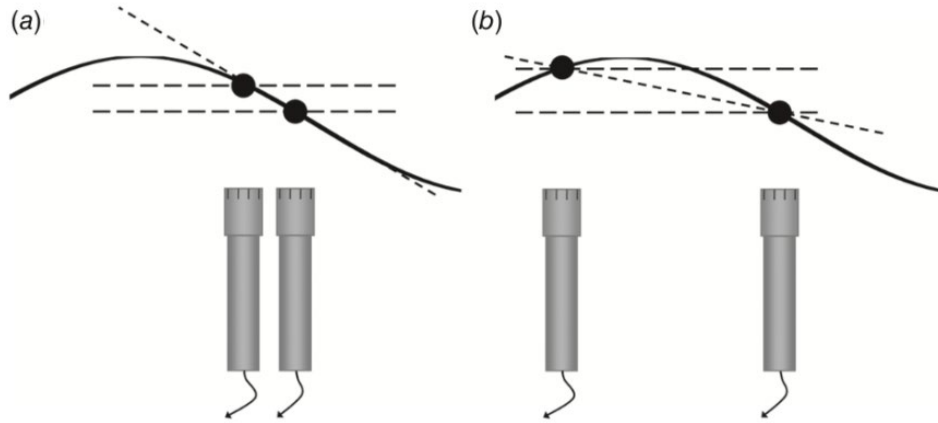
Figure 1.3.1 Effect of microphone spacing for a given wavelength, by increasing distance the acoustics phase also increases.

The math for the estimation of intensity magnitude error is given by:

$$L_e = 10 \, log_{10} \left[\frac{sin(kd - \varphi)}{kd} \right]$$ *Equation 1.3-1*

And the acoustic phase is given by:

$$\theta = kd \; or \; \frac{2\pi f}{c} d$$ *Equation 1.3-2*
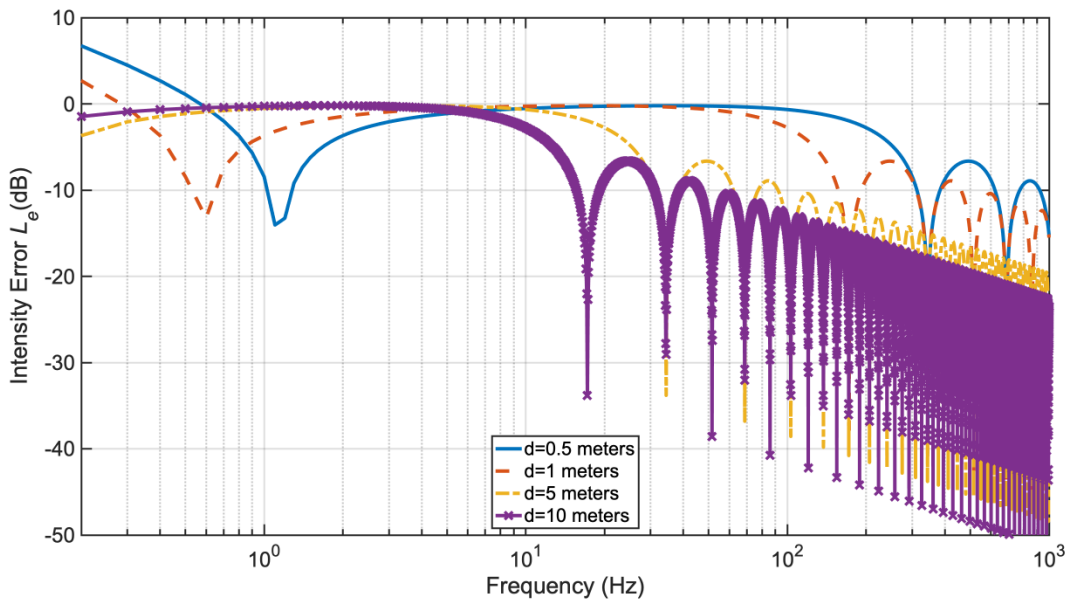
Figure 1.3.2 Intensity magnitude error using Equation 1.3-1 for a phase mismatch $\varphi = 0.6°$.

The phase mismatch affects the intensity calculations in the low-frequency region, where

the acoustic phase is smaller than the phase mismatch. Figure 1.3.2 shows the intensity error with

6

a constant phase mismatch of 0.6˚. The smaller distance spacing probes (0.5 and 1 m) show significant errors from 2 Hz and below. Meanwhile, bigger distance spacing probes show errors close to zero below 2 Hz. Therefore, the intensity error due to instrument phase mismatch is going to be bigger for low frequencies.

The finite-difference error depends on the sensor separation distance and the acoustic wavelength. The error in intensity calculations due to the finite-difference has been shown[2] to be related with the following:

$$\hat{I}_r \Big/ I_r = \frac{\sin k\Delta r}{k\Delta r} \qquad \qquad \textit{Equation 1.3-3}$$

Figure 1.3.2 shows the effect of finite-difference errors on intensity calculations. The errors are larger for frequencies with a wavelength near or small than twice the spacing distance, which means the frequencies near or higher than spatial Nyquist show big errors.

Note that using larger spacing probes could raise another error source due to a coherence drop. Depending on the source intensity level and the acoustic field, a spacing distance too big could introduce extraneous noise on the signal, affecting the coherence and bringing random signals to the measurement. Such noise might be wind noise, highway noise, terrain scatter randomly arriving at microphones. The errors for intensity measurements and their limitations are reasonably well known,[10,11] and addressing them gives frequency band limits for accurate calculations.

1.4 Infrasound

Sound is a pressure disturbance in some medium[1]. Sound propagation travels as waves at several frequencies, and the acoustic waves under 20 Hz are classified as infrasound. Infrasound sources are generated by natural phenomena and man-made sources, such as rocket, wind turbines,

7

volcano, seismic movement, oceans movements, aircrafts noise, industrial equipment, etc[12] and are not perceptible by human ear. An infrasonic wavelength is usually a large value, i.e., at 20 Hz the wavelength is 17 meters, and for 1 Hz is 343 meters. The infrasonic wave involves large physical spaces, and the acoustic phase would have a small variation between a pair of microphones placed within a small distance.

The initial interest in detecting infrasound was focused on natural phenomena[13], although literature would show the infrasound's interest in different transport vehicles[14]. The scientific community was interested in the effect of infrasound on drivers and passengers[15,16,17]. Still, the significant development in sensors came when more interest emerged in sonic booms and other man-made infrasonic sources. Nowadays, more and more free-field microphones with infrasonic capability are commercially available. Modern equipment, including portable-high sampling rate acquisition systems, allows for measuring the infrasound and getting more information.

The most common infrasound measurement is the volcano and weather-related fields[18,19]. Several arrays of sensors have been developed for explosions, volcano, and weather monitoring[20]. Such arrays involve a group of sensors with a spatial separation of hundreds to thousands of meters. The sensors typically have a bulky setup, including windscreen and manifold devices such as a porous hose.

The calibration required for the sensors has been a developing matter of study. Infrasound generators[21,22] have been tested to access a reliable source that allows calibrating sensors in the infrasound. Producing an infrasonic source is a big challenge because it involves significant air volume movement. Two devices in the literature[21,22] use pneumatic modulators to produce infrasonic waves from pulsating air stream pulses.

1.5 Challenges

The long wavelengths associated with infrasound makes it a challenge to measure the intensity. Probe spacing will be a small fraction of the wavelength, and the instrument mismatch would be much higher than the acoustic phase. Also, most of the microphone responses are beyond the infrasound limits.

Microphone phase mismatch becomes a particular problem in infrasound applications because of the rapid variation in the relative phase between microphones near the microphone corner frequency. A considerable separation distance will cause the acoustic phase difference to be more significant than the instrument mismatch, giving a better response for low frequencies, but this will lower the probe's upper-frequency limit. On the other hand, having a small separation distance will improve the accuracy of high frequencies' calculations and reduce the instrument's accuracy at low frequencies. Thus, there is a frequency band limitation using the vector intensity method.

M. Pawlaczyk-Luszczynska in his article[23] showed vector intensity measurements into the infrasound region using a three-microphone probe. According to this paper, the optimum distance between microphones ranges from 3.4-85m to determine noise in the 2-50 Hz range. The intensity direction angle's uncertainty is around ±3˚ using regular devices for the installation measurements such as tape measure and flagpoles.

1.6 Thesis scope

This thesis describes a free-field microphone calibration for intensity and applies it to real infrasonic sources' intensity measurements. The calibration consists of finding the instrument

mismatch for two sets of 1/2" free-field microphones, as shown in Chapter 2. The calibration requires finding a real or laboratory infrasound source to calibrate microphones. This work also seeks to elaborate recommendations for probe spacing, averages or length recordings, and instrument mismatch.

The last two chapters show the PAGE method application in infrasonic sources. Those chapters have the intensity measurements using free-field microphones with larger separation distances than commercial intensity probes but compact compared to state of the art in infrasonic arrays.

2 Chapter 2: Phase and amplitude correction of microphones for infrasound vector intensity using three methods

This chapter describes the phase and amplitude correction of 12.7 mm diameter, Type-1 microphones for three frequency bands, including within the infrasound regime, and its application to acoustic measurements. Previous data stem from acoustic intensity measurements using two-dimensional, four-microphone probes[24], which emphasized the requirement of having the acoustic phase and amplitude difference be much greater than the interchannel mismatch. Although correcting the amplitude/phase is well-known, obtaining the necessary transfer functions in the infrasound regime is challenging because (1) signal-to-noise ratios are often poor, (2) long measurement times are required for averaging, and (3) microphone responses vary significantly across these low frequencies. In this paper, a convenient infrasound source previously studied for infrasound adverse effects on humans[15,17,25,26] is intended for performing a relative calibration.

2.1 Microphone Calibration

Acoustics measurements should be performed with devices that are accurate enough to give valuable data. A calibration involves exciting the microphones with a known input and determining the relationship between the microphone responses[27]. The relationship obtained is the calibrated sensitivity. There are several standards to specify the microphone calibration, although the infrasound is not well covered. While some microphone manufacturers have developed infrasound calibration for amplitude response[28], infrasound vector intensity measurements require finding the instrument mismatch.

2.1.1 Absolute Calibration

This method implies the accurate control of the input and the measurement of its fundamental units. There are three ways to perform absolute calibration: low-frequency correction, reciprocity, and electrostatic actuation. The low-frequency correction will be applied in this work.

2.1.1.1 Low-frequency correction

The primary purpose of absolute calibration is to measure an instrument's output while excited to a known input. For microphones, the known input is the acoustic pressure applied to the diaphragm. The most frequent way to apply the known acoustic pressure is done inside a pistonphone which contains a rigid-walled chamber. The cavity dimensions are smaller than the low-frequency wavelength to avoid the pressure variations due to the microphone's body scatter at high frequencies. An oscillating piston drives the pistonphone's cavity with a known area and displacement. The resulting acoustic pressure is supposed to be uniform inside the chamber. The sensitivity is given by the ratio of microphone output voltage and the known free-field pressure applied in the cavity.

$$M_o(f) = \frac{\hat{e}_{oc}(f)}{\hat{p}_f(f)} \qquad \textit{Equation 2.1-1}$$

The most common excitation is at 250 Hz and 114 dB with 10 Pa (RMS value) pressure. This excitation is convenient because of the flat microphone response in that region. Also, excitation at 1 kHz and 94 dB (1 Pa RMS) is convenient because the input is not affected by signal weightings. In addition, the barometric pressure for the pistonphone should be taken into account to have consistency with the assumed pressure distributed inside the cavity volume.

2.1.2 Relative microphone calibration

The calibration could also be accomplished using two transducers, making the calibration of one microphone relative to another. This calibration enables one transducer to replicate those measurements that would have been made with the other. If the second transducer is a reference standard, the relative calibration provides convenient means to precise measurements. The practical reason for relative calibration in intensity measurements is enhanced because of the required number of similar transducers.

Some of the relative calibration techniques are substitution, standard source, equal excitation, and switching technique. The work presented in this paper is the application of equal excitation and switching techniques.

2.1.2.1   Equal excitation

This technique consists of having two or more transducers simultaneously subject to the same acoustic excitation. Then, measuring the frequency response function from their outputs will give the calibration.

Considering an array of two microphones will conduct to the following situation:

$$H_{cal,12} = \frac{G_{12}}{G_{11}} = \frac{\hat{e}_2}{\hat{e}_1} = \frac{\hat{p}_o M_2 E_2}{\hat{p}_o M_1 E_1} = \frac{M_2 E_2}{M_1 E_1} \qquad \textit{Equation 2.1-2}$$

Here $\hat{e}_1$ and $\hat{e}_2$ are the complex output voltage, M_1 and M_2 are the microphone sensitivities and E_1 and E_2 are the gain response.

The correction consists of knowing the transfer function and then calibrate the measurement made by one microphone as the measurement that would have been made by the other. This is accomplished by multiplying or dividing the output signal of one microphone by $H_{cal,12}$

13

$$\hat{e}_1 H_{cal,12} = \hat{p} M_1 E_1 \left(\frac{M_2 E_2}{M_1 E_1} \right) = \hat{p} M_2 E_2 \equiv \hat{e}_2 \qquad \textit{Equation 2.1-3}$$

2.1.2.2 Interchange method

Following the work of Chung & Blaser[29] a sensor-switching calibration it is possible to relative calibrate a microphone to another and removing the electroacoustics difference between those microphones.

Consider the situation shown in Figure 2.1.1. Microphone M1 is at position 1 for configuration I and microphone 2 is at position 2. Then, microphones M1 and M2 swap position for configuration II and the geometric mean of each transfer function is the desired calibration.

$$H_{I,12} = \frac{G_{I,12}}{G_{I,11}} = \frac{\hat{e}_{I,2}}{\hat{e}_{I,1}}, \ H_{II,12} = \frac{G_{II,12}}{G_{II,11}} = \frac{\hat{e}_{II,2}}{\hat{e}_{II,1}} \qquad \textit{Equation 2.1-4}$$

$$H_{cal,12} = \sqrt{H_{I,12} H_{II,12}} \qquad \textit{Equation 2.1-5}$$
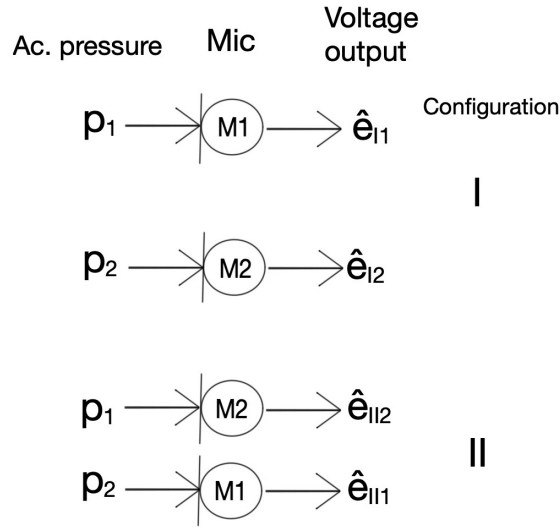
Figure 2.1.1. Switching calibration sketch

2.2 Calibration methods

2.2.1 Overview

One of the biggest challenges is to find an infrasonic source to run measurements. According to Gabrielson et al.[30], to maintain the pressure amplitude at 0.1 Hz, it is required to move an air volume increased by 1000 times the necessary volume for 100 Hz for a simple source in a free field. Several trials were made during this research work to find a coherent and sufficient infrasonic source. Among the experiments, there was an in-field switching calibration using the noise field of a large rocket motor, a vertical position variation using a robot arm, ambient measurements inside large buildings, and wind turbine acoustic measurements. Although those experiments contained infrasonic energy, there was low consistency and another noise presence. An ideal calibrator would be a laboratory enclosure driven by a large excursion subwoofer or similar, although it was not explored for this research. Finally, two infrasound sources were suitable for longer recordings and useful signals to apply an equal excitation calibration.

The first infrasound source was ambient measurements inside a moving passenger car. Results showed high sound pressure levels, high coherence, and enough consistency for different conditions. The second significant source of infrasound was the acoustic field caused by a hot air balloon gas burner. The train of pulses at specific periods gave a coherent and robust signal in the infrasonic range.

Although infrasonic sources showed useful broadband signals in that region, finding how well match the microphones are at mid and high frequencies is necessary. Therefore, the calibration is divided into three ranges: the infrasound regime, the low audio, and the audible region. The

infrasound and low audio ranges were calibrated using an equal excitation, whereas an interchange method was applied for the audio range.

Equal excitation calibration is applied to find the instrument mismatch between a microphone "x" and other "y" being tested, as shown in Figure 2.2.1. Finding the instrument mismatch consists of representing the complex pressure in the frequency domain and obtaining the transfer function (or the frequency response function) to analyze the phase and magnitude between microphones "x" and "y".
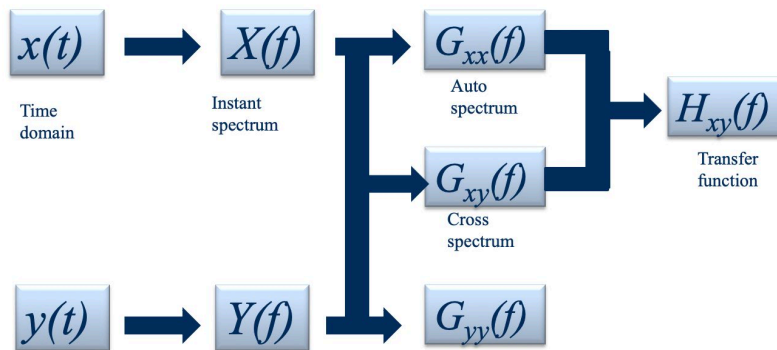
Figure 2.2.1. Signal processing scheme

The transfer function determined under equal excitation using a known infrasonic field will count for amplitude and phase instrument mismatch for each pair. The calibrated transfer function is applied to correct the transfer function measured with the same pair in any other field by dividing the current measurement transfer function by the instrument mismatch transfer function, as denoted by Equation 2.2-1. This is valid only for the PAGE method equations.

$$H_{calibrated} = (H_{current})/(H_0) \qquad \textit{Equation 2.2-1}$$

H_0 is the instrument mismatch, and $H_{current}$ is the transfer function from any field measurement.

The instrument mismatch is considered frequency-dependent and stable for different measurements. The mismatch transfer function application is expected to improve intensity results, including far-field static rocket test and near-field balloon burner measurements. Recordings were longer than 1 minute, and results are shown in chapter 3 and 4. Each event provides a known propagation direction and expected equivalence of significant, low-frequency amplitudes, which allows for correction comparison of the microphone transfer functions at low frequencies.

2.2.2 Microphone characteristics

Two models of 12.7 mm diameter type-I microphones were used, namely GRAS 47AC and GRAS 46AE. The GRAS 47AC microphone set has four units with serials numbers 327344, 327345, 327346, and 327347. This microphone model is specially designed for infrasound measurements and is furnished with a low-frequency adaptor and dedicated preamplifier. The frequency range (±3dB) is 0.1Hz, sensitivity is 8mV/Pa, and the dynamic range upper limit is 148 dB.

The GRAS 46AE set also has 4 units; the first one is labeled B1 with serial number 245983, the second one is B2 serial number 234275. The third unit is C1 with serial number 245934, and the fourth is C2 with serial number 245936. The GRAS 46AE is optimized for all acoustics applications where the primary source's location is known, and the microphone can be pointed to have 0° incidence angle. This microphone set has a dynamic range upper limit of 138 dB. The frequency range (±2dB) is ~3.15 Hz, and the sensitivity is 50 mV/Pa. This particular set of 4 units has been phase-matched for the audio range.

All eight microphones were subjected to an absolute calibration at 250 Hz using the GRAS 90CA calibration system at Brigham Young University, Provo. The following Table 2.2-1 shows the microphone sensitivity values obtained by the level calibration.

Microphone type, serial number, and label	Sensitivity	Date
46AE, 245983 "B1"	50.70 mV/Pa	4/7/21 5:01 pm
46AE, 234275 "B2"	53.69 mV/Pa	4/7/21 5:26 pm
46AE, 245934 "C1"	50.07 mV/Pa	4/7/21 5:35 pm
46AE, 245936 "C2"	53.22 mV/Pa	4/7/21 5:43 pm
47AC, 327344 "44"	9.36 mV/Pa	4/8/21 3:33 pm
47AC, 327345 "45"	9.33 mV/Pa	4/8/21 3:47 pm
47AC, 327346 "46"	8.89 mV/Pa	4/8/21 5:09 pm
47AC, 327347 "47"	8.66 mV/Pa	4/8/21 5:20 pm

Table 2.2-1 Microphone sensitivity values from absolute level calibration made with GRAS 90CA calibration system at Brigham Young University, Provo.

2.2.3 Car measurement

This calibration experiment took place inside a moving vehicle. The microphones were placed in a probe with a small spacing to approach an equal excitation setting. The probe has the microphones in a line abreast array spaced by 2 diameters (½") apart and was located on the vehicle's floor. Figure 2.2.2 shows the configuration of the probe and the location inside the car. The probe configuration design allows a high ratio between the acoustic wavelength and microphone distance ($\lambda/d \gg 1$) for low frequencies. The frequency range to be covered in this part is between 0.1 to 20 Hz.

18
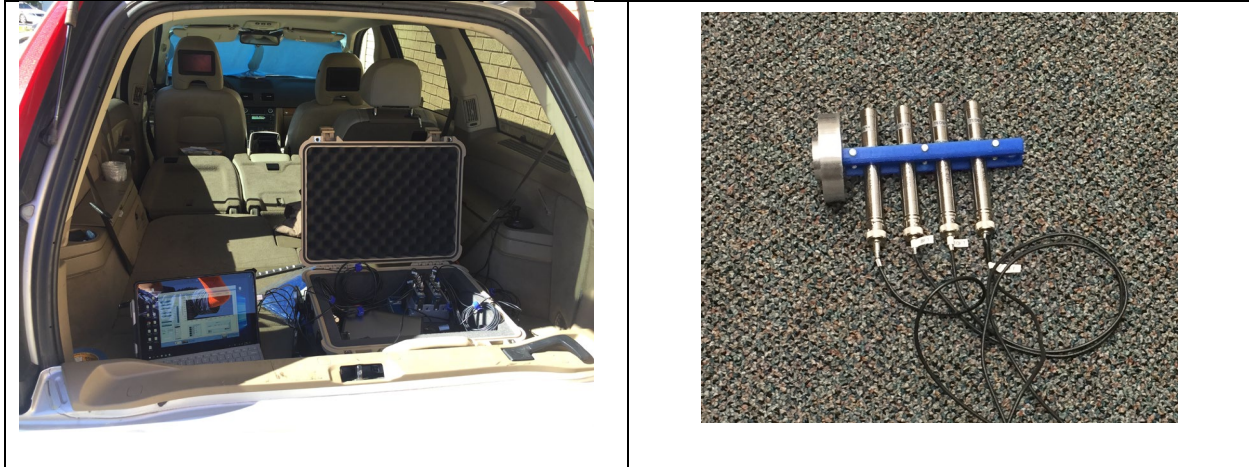
Figure 2.2.2 Microphone probe setup inside a passenger car. The probe was placed on the floor of the cargo area. Each microphone was spaced by 12.5 mm having a maximum of 75 mm between first and last in line.

In the past decades, there was a high scientific interest in the infrasound presence inside transport vehicles. Several articles[13,14,15,16,17,25,31] showed the infrasonic generation in transport, and they tried to address the adverse effects on drivers and passengers. The interest in transport vehicles' infrasound generation leverages using a passenger car as an infrasound source for a microphone relative calibration.

The source is originated from the aerodynamics forces and the car body vibration[17,32]. Car's body interaction with the airstream generates vortex-shedding, leading to lift and drag and surface vibration. According to Burton and Blevins[32] the acoustic response would not be much dependent on surface vibration amplitude as on aerodynamic forces amplitude (high-speed drives has higher sound level than low-speed drive). The dimensionless number describing the oscillating flow mechanisms is the Strouhal Number. This quantity relates the frequency corresponding to vortex shedding and is given by the Strouhal number S, flow velocity V, and diameter D of the body, as Equation 2.2-2.

$$\omega = 2\pi * S * \frac{V}{D} \qquad \textit{Equation 2.2-2}$$

19

In a resonance condition, the aerodynamic forces and the surface vibration will radiate sound power at or near the vortex shedding angular frequency. For example, a car moving at V=75mph~33.3 m/s and the exterior width D~2 m, the angular frequency would be ~25.3 rad/s or 4~5 Hz, considering a Strouhal number of 0.22.

Another study by Moreau et al.[33] found tonal noise coming from a sharp trailing edge flat plate, with the fundamental at 244 Hz. The far-field acoustic spectral analysis showed increased noise levels centered at the tone harmonics. The correlation between vortex shedding and far-field noise demonstrates the acoustic radiation generated by vortex-shedding, although in that case, the fundamental was out of the infrasound regime.

In a book[13] concerned with the environmental aspects of infrasound and low-frequency vibration, Tempest et al. made a summary of infrasonic measurements in transportation, including passenger cars, commercial vehicles, and other vehicles. This text focused on the infrasound exposure effects on human beings, although it showed high infrasonic inside vehicles depending on vehicle speed and size.

The calibration measurements are based and limited to the assumption that the microphone distance is near two orders of magnitude lower than the wavelength. Only the infrasonic and low audio range calibration will assume the high ratio for this work's scope. For example, the wavelength of a 50 Hz wave is ~6.86 meters in standard air, and the maximum microphone spacing considered in this case is 0.075 meter. The ratio between both is 91.5, not exactly two order of magnitude but enough for the purpose of this calibration.

This section shows 3 measurements to illustrate the effect of driving speed on sound pressure levels. The 3 measurements are the city, mixed, and highway traffic. City traffic measurement was made with the car going at low speed (below 50 MPH) and several stops. The

mixed traffic involves driving high and low speed, and some stops. Highway traffic measurement was made with no stops and a driving speed of 70 MPH on average. All of the measurement's recordings were 20 minutes in length.

2.2.3.1 Sound Pressure Level, Coherence and Transfer Function for GRAS 47AC

The spectra shown in Figure 2.2.3 highlight the relation between the vehicle average speed and the sound levels. The levels are the average across the probe. Also, the curves shown a broadband noise contribution in the infrasound with small peak at 4-5 Hz and a second and more clearly visible peak at 12-15 Hz. These values are believed to be related to vortex shedding and with the resonance frequency of the car cabin[17].
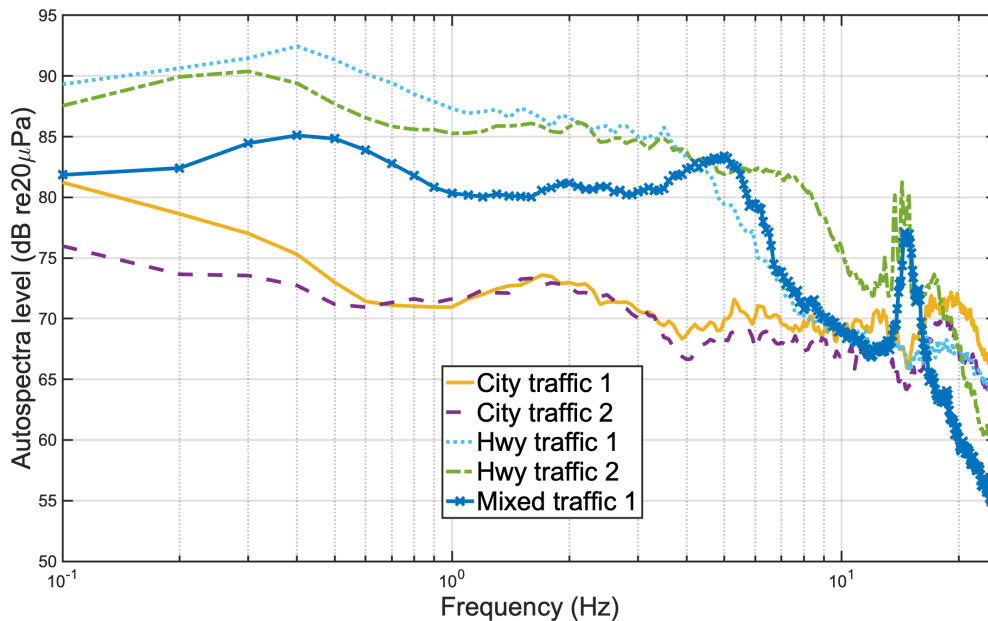
Figure 2.2.3. Autospectra levels averaged across the probe for GRAS 47AC set. Five measurements are shown with different driving conditions. Frequency resolution 0.1 Hz.

Figure 2.2.4 shows coherence plots corresponding to GRAS 47AC set, where high coherence is found for this set of microphones at lower frequencies. Note that only 3 of the 15 measurements are shown for convenience.
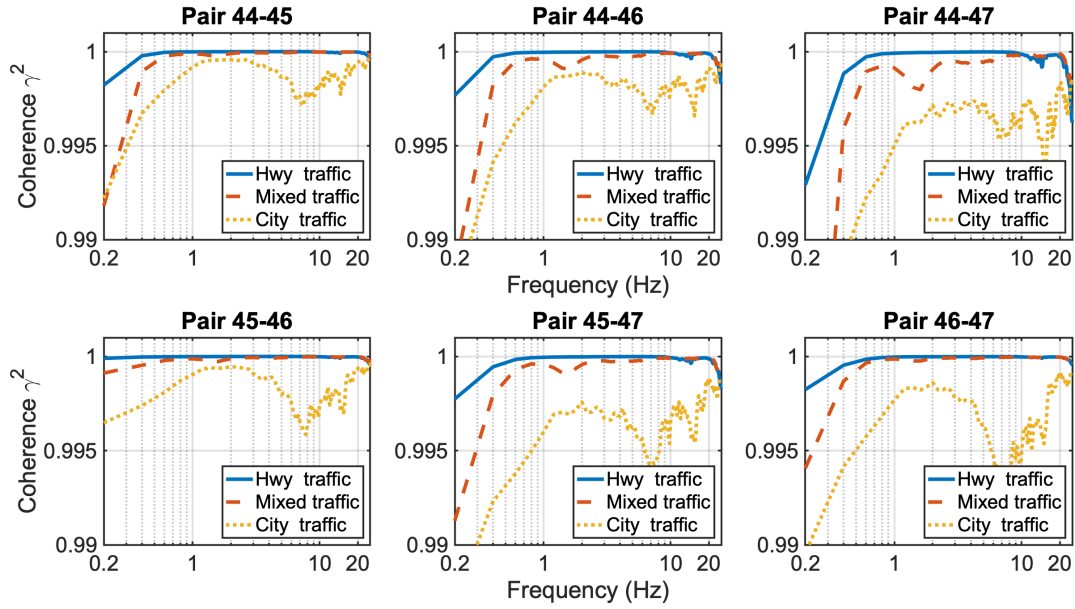
***Figure 2.2.4 Coherence for the six pairs combination of the Gras 47AC microphone set.
Frequency resolution 0.2 Hz.***

The transfer function for the GRAS 47AC set is shown in Figure 2.2.5 and Figure 2.2.6, phase and magnitude respectively.
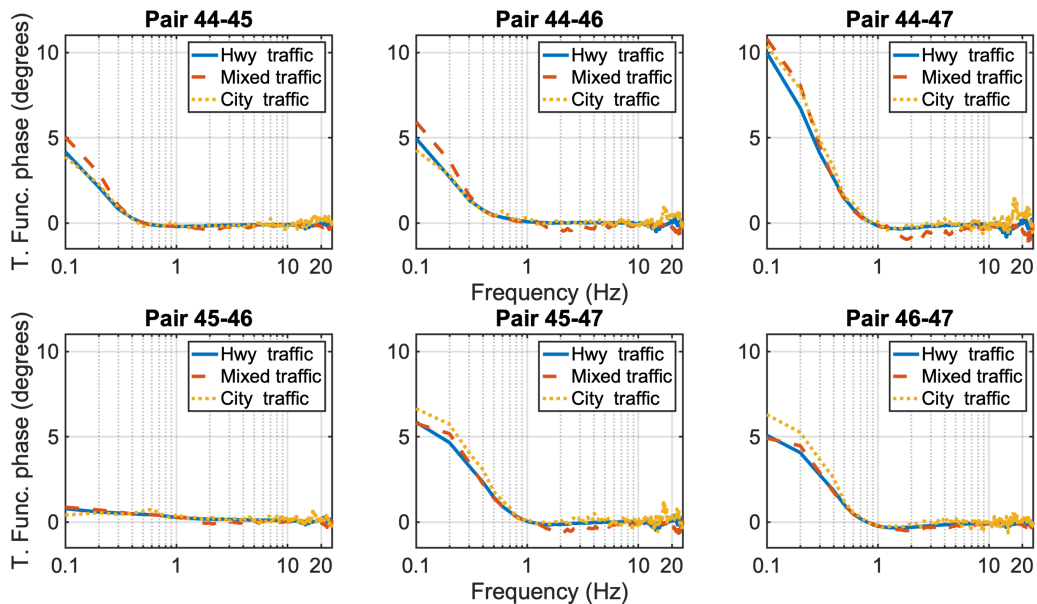
***Figure 2.2.5 Transfer function <u>phase</u> for GRAS 47AC microphone set. 3 of 15 measurements
are shown. Frequency resolution 0.1 Hz.***

22
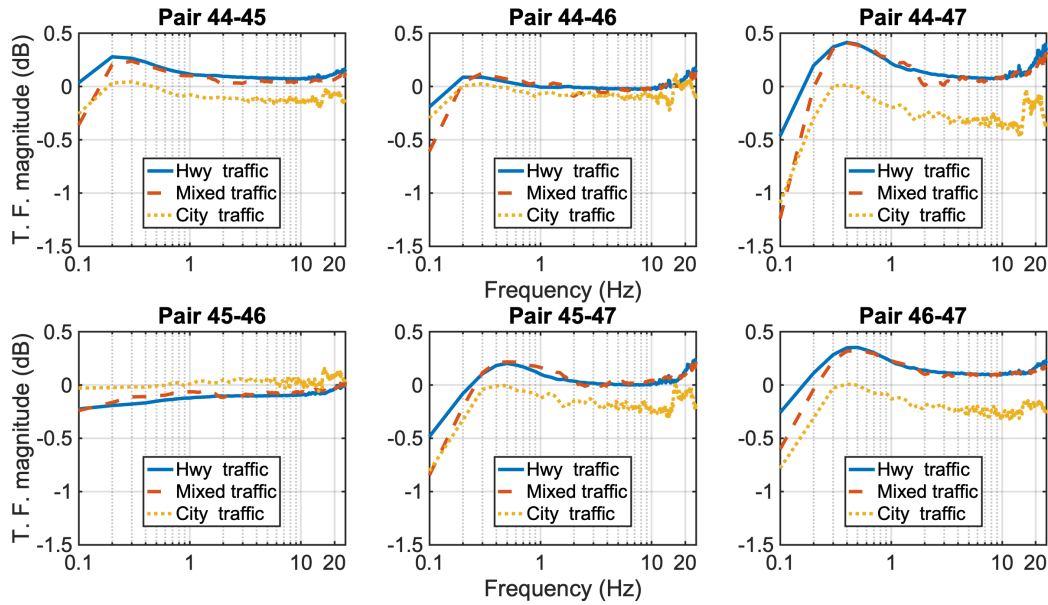
Figure 2.2.6 Transfer function magnitude for GRAS 47AC microphone set. 3 of 15 measurements are shown. Frequency resolution 0.1 Hz.

The transfer function for the 47AC microphones is consistent for different measurement conditions. Phase values are below 6° of mismatch except for 44-47 pairs that start at 10° and then decay near zero degrees. The 45-46 pair is the best phase-matched for this set, having a maximum mismatch lower than 1° at 0.1 Hz. The magnitude plot shows the close similarity for mixed and highway traffic conditions related to the higher vehicle speed. Also, note the magnitude deviation is lower than 0.5 dB for all microphone pairs from 0.2 Hz and above. Although there were 15 measurements in the infrasonic range, only the data with a coherence higher than 0.99 builds the instrument mismatch's average curve.

2.2.3.2 Sound Pressure Level, Coherence, and Transfer Function for GRAS 46AE

Figure 2.2.7 shows the autospectra level averaged across the probe using GRAS 46AE set. Each measurement was made driving at different traffic and speed conditions. There were 9 measurements done with GRAS 46AE, although only three are shown for convenience.
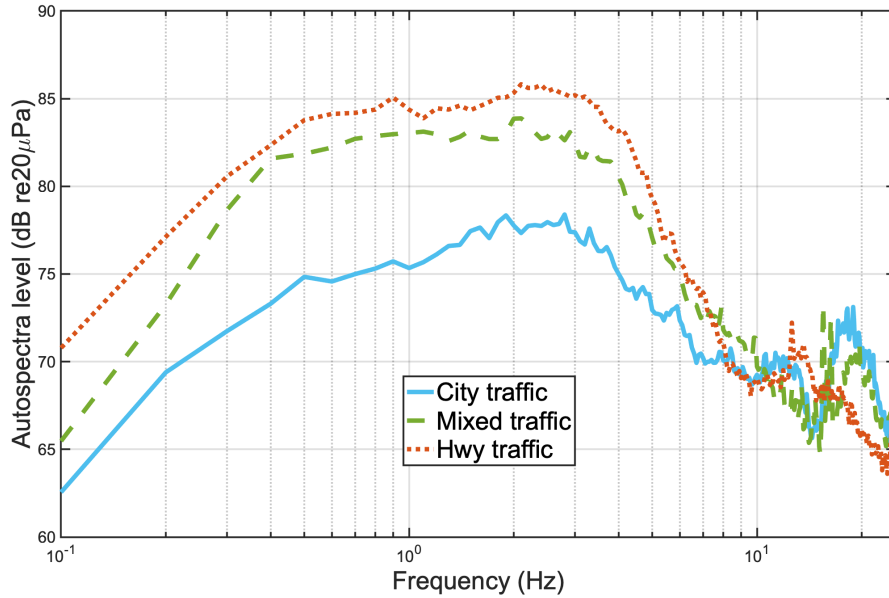
Figure 2.2.7 Autospectra level averaged across the probe for 46AE microphones. Mixed traffic (dash line) is almost the same as highway (dot line) but a lower speed.

The levels in Figure 2.2.7 are over 65 dB on average for the infrasound portion. Each line represents a different time and traffic condition. The microphones are sensing the maximum energy in the 0.5 to 4 Hz range, although there is still energy over 65 dB up to 25 Hz.
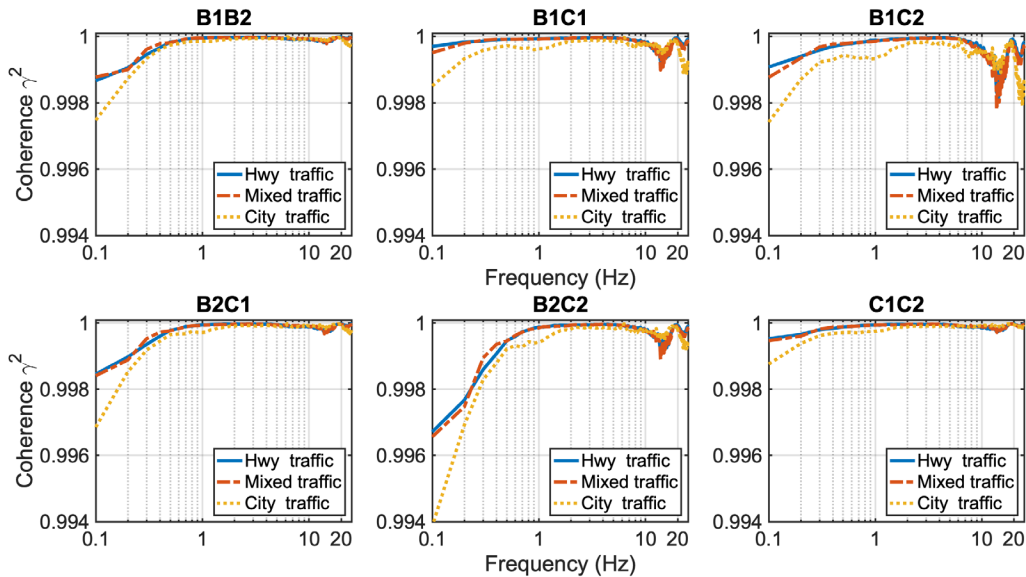
Figure 2.2.8 Coherence for GRAS 46AE six pairs combination. The measurement on highway traffic shows a slightly higher coherence values in general. The speed for the highway driving was 70 MPH on average for 20 minutes recording.

24

Figure 2.2.8 shows high coherence values for the infrasound range. The high coherence and autospectra levels measured at the moving car experiment confirm the vortex-shedding's infrasonic source.

The GRAS 46AE pair combination's transfer function is shown in Figure 2.2.9 and Figure 2.2.10, phase and magnitude, respectively. Transfer function plots show a consistent relationship for different trials.
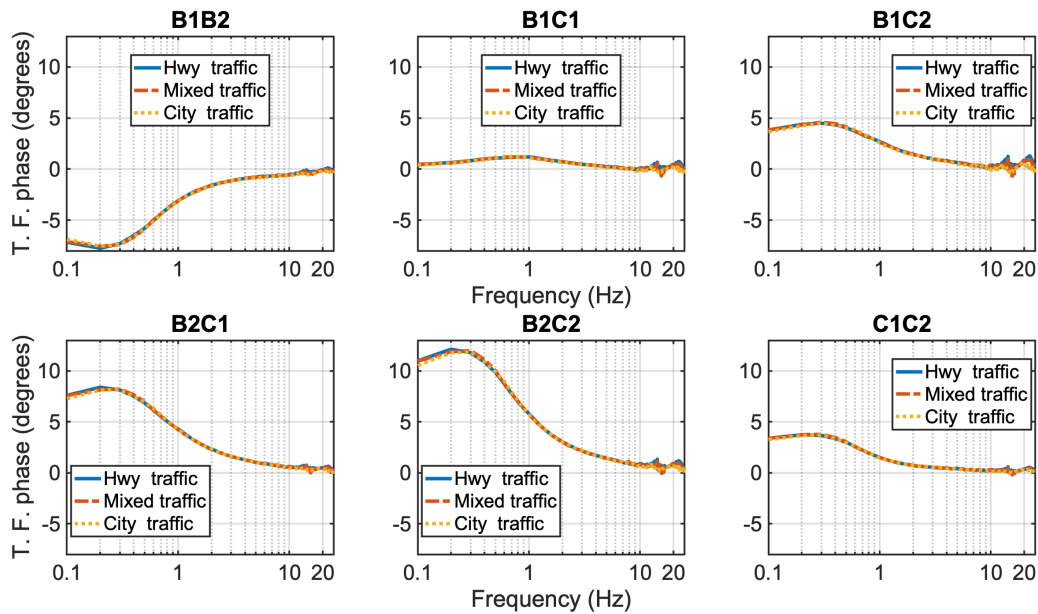
Figure 2.2.9 Transfer function phase for six pair combination of GRAS 46AE and 3 driving condition. Frequency resolution 0.1 Hz.
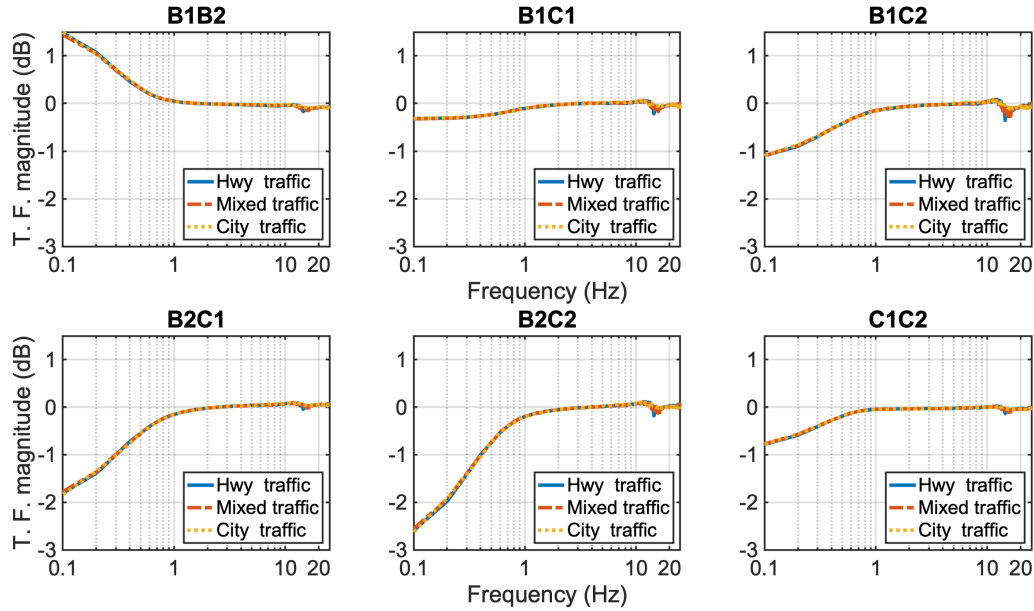
Figure 2.2.10 Transfer function magnitude for six pair combination of GRAS 46AE and 3 driving condition. Frequency resolution 0.1 Hz.

2.2.4 Reverberation chamber

The next frequency range in this research is the low audio. This experiment was designed to find the instrument mismatch for selected frequencies in the range of 15 to 50 Hz. Any source inside the reverberation chamber will be boosted by the standing wave field inside the room. The wavelength for this frequency range is 22.8 to 6.9 meters, and the ratio with microphone distance is still within the initial assumption. Measurements were taken using two subwoofers playing a sinewave input at several frequencies in the range of interest. There was an extensive number of recordings with the tonal signal corresponding to a sinewave between 15-50 Hz. The microphones were located in one of the room's corners and placed near together (about 2 diameters spaced). Although a small acoustic phase is expected to be present, the acoustic phase is negligible because the room's larger dimension is the height, and the probe places the microphones at the same level. Figure 2.2.11 shows the experiment layout in the reverberation chamber at Brigham Young University.

www.manaraa.com

Figure 2.2.11 Reverberation chamber experiment layout. Two subwoofers were placed in the corner of the room facing against the wall. Microphones were located on the floor at the other corner of the room using the same array configuration used in the car.

The maximum spacing in this probe (with line-abreast array) will be 5 times the diameter, corresponding to the first and last microphone in the line. The wavelength for both frequency limits is 22.9 meters for 15 Hz and 6.9 meters for 50 Hz; those values are much larger than the maximum microphone separation distance.

The tonal signal is meant to find the instrument mismatch at the sinewave frequency played at each recording. Although the subwoofers' flat response does not extend below 40 Hz, its output is amplified by the reverberation room, giving a reasonable amount of energy for frequencies below the subwoofer specification, as is shown in Figure 2.2.12. The frequency sequence for the recordings is 15, 18, 20, 22, 25, 27, 30, 32, 35 37, 40, 42, 44, 47 and 50 Hz.

2.2.4.1 SPL, Coherence and Transfer Function for GRAS 47AC
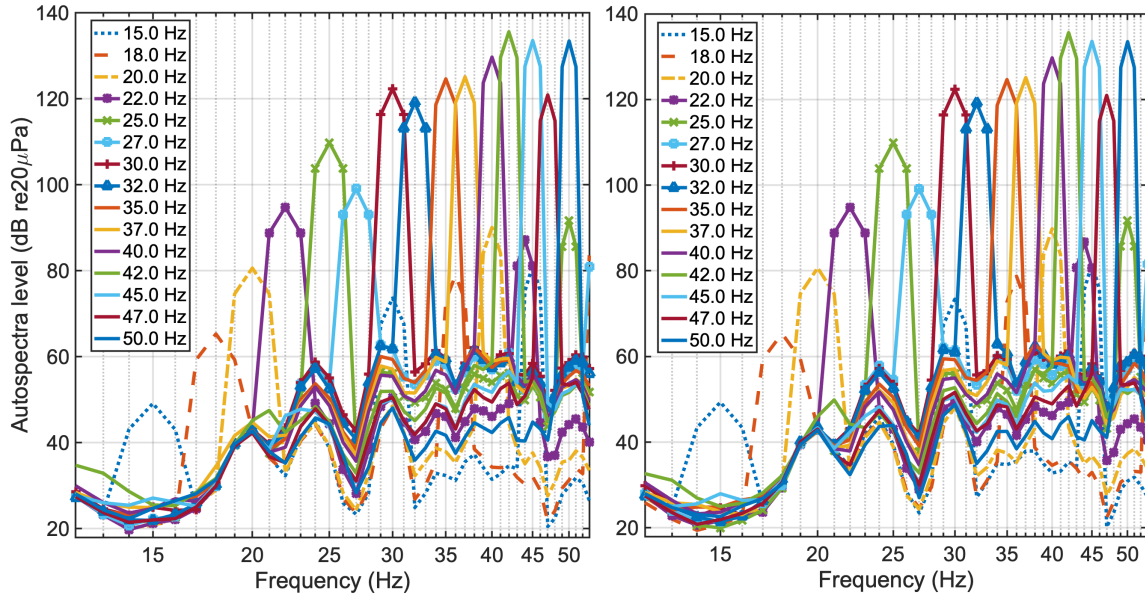
Figure 2.2.12 Autospectra for the sinewave tones played at the reverberation chamber.

The left side of Figure 2.2.12 shows the tonal levels for one measurement, and right side shows a different measurement time. Both results show consistency for each frequency mode. Figure 2.2.13 shows the coherence for the GRAS 47AC microphone pair combinations and for the frequency corresponding to each tone signal. The coherence is consistently high and proves the source's presence with a sufficiently strong acoustic field inside the reverberation chamber.
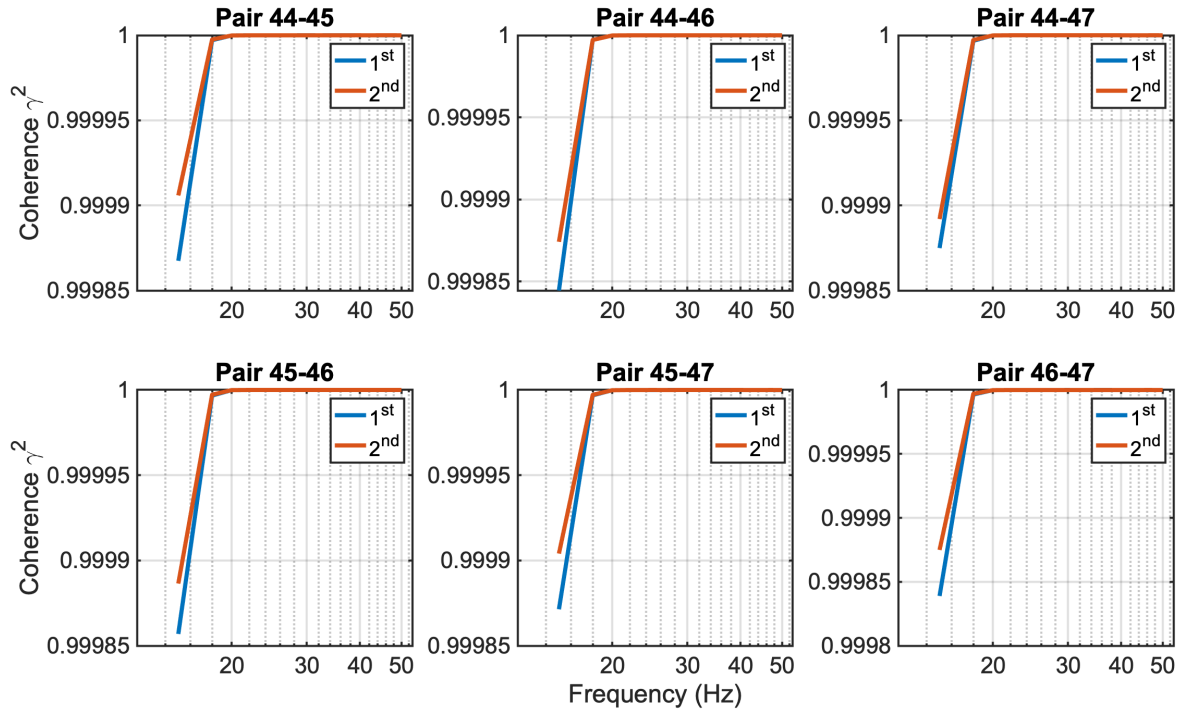
Figure 2.2.13 Coherence for the six GRAS 47AC microphone pairs. The plots were made drawing the line between each tonal value.

Figure 2.2.14 and Figure 2.2.15 show the phase and amplitude for each microphone pair from the GRAS 47AC set. These plots were also made by joining the values at each fundamental frequency for each tonal signal. Therefore, any value between tonal signal shown on the plot are interpolated. There are two measurement set shown labeled as 1st and 2nd. Also, in Figure 2.2.14, a dip is observed at 27 Hz which is related with the height mode of the room.

29
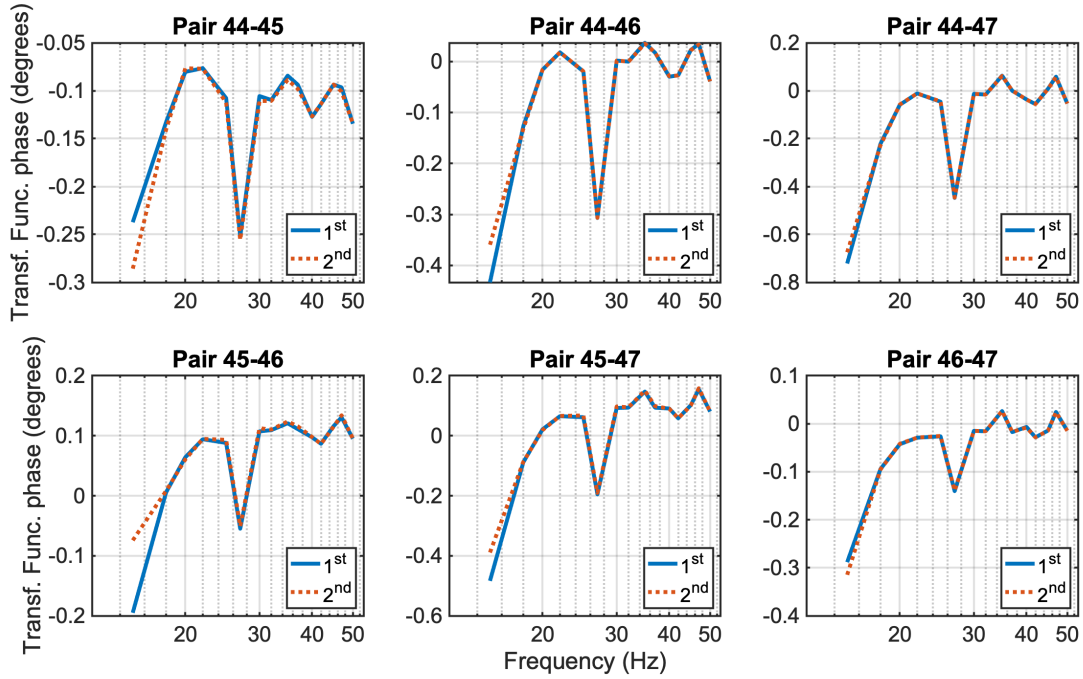
Figure 2.2.14 Transfer function phase for pair combinations of the GRAS 47AC set.
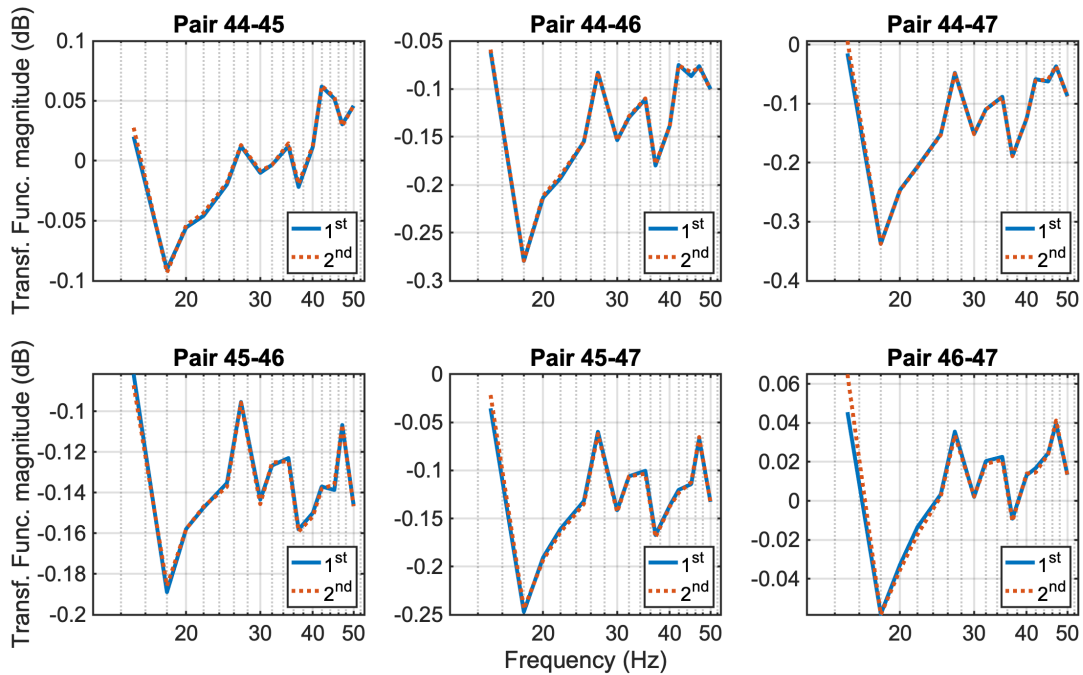
Figure 2.2.15 Transfer function magnitude for six pair combinations of the GRAS 47AC set. Two instances are shown having a close relation.

30

The values for the phase mismatch shown Figure 2.2.14, range from -0.6 to 0.2 degrees. Also, both measurements show consistency and low uncertainty.

2.2.4.2   Explanation for 46AE

This microphone set was previously phase matched for low audio and audible range, therefore the mismatch for 30 Hz and above is less than 0.5˚ up to 1 kHz. The difference between the infrasound method and the intensity calibrator method remains below 0.4˚ for 50 Hz.

2.2.5 Intensity Calibrator

An intensity calibrator was used to find the mismatch in the audible range. There are different calibrators from commercial acoustics companies. In this case, the GRAS 51AB was available. This calibrator is meant to be accurate for a frequency range between 40-6,400Hz. The intensity calibrator application follows a summary of the work given by Chung & Blaser[29].

The intensity calibrator GRAS 51AB has 2 microphone ports and an input for the signal to be played inside the calibrator's cavity. In this case, the signal used was a chirp from 40 Hz-6.4kHz with 1-second chirp duration and an equal ratio between the sampling frequency and the number of samples. The chirp shape signal allows having broadcast energy within the range of interest. Figure 2.2.16 shows the waveform of the chirp signal for one of the recordings with the 47AC microphones. The signal measured with the 46AE is near the same.
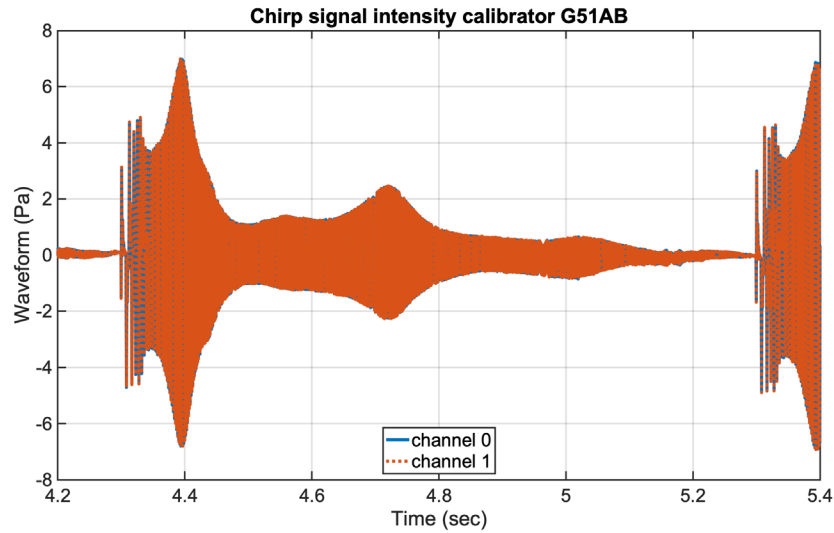
Figure 2.2.16 Waveform of the chirp signal used in one of the measurements made with GRAS 47AC microphones.

The chirp autospectrum is shown in Figure 2.2.17. The frequency resolution to compute these calculations and plots was 5 Hz. Energy distribution along the chirp's frequency range (40Hz-6.4kHz) has a peak at 600-700Hz and an overall value over 60 dB up to 3.2kHz and then has a new prominent peak at 4.5kHz and then dropping off for the last portion of the range.
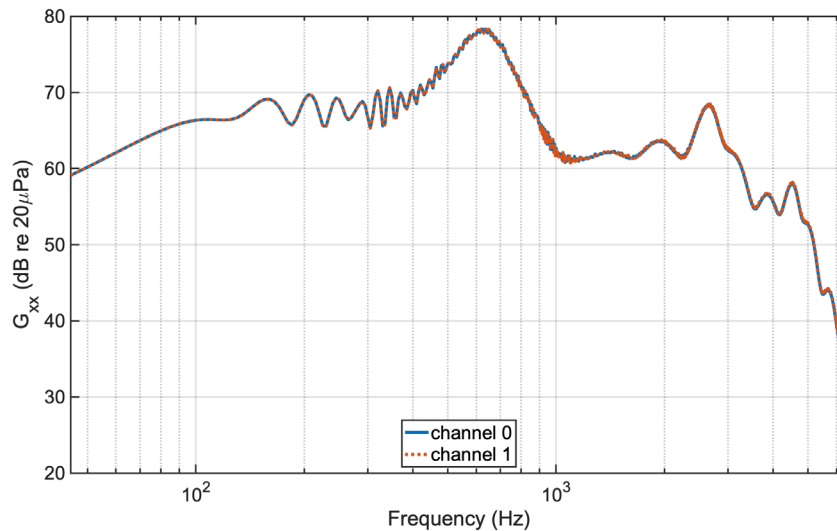
Figure 2.2.17 Chirp autospectra for one of the measurements using GRAS 47AC with 5 Hz frequency resolution

2.2.5.1 47AC analysis

Figure 2.2.18 shows the plot of coherence for the range of interest. Coherence for all of these measurements was mostly equal to 1 since no significant noise level is present inside the calibrator. Coherence, as was expected for this calibrator, is high for the range of interest. Note that a roll-off starts at ~5300 Hz, although it is still high with ~0.967 at the end of the frequency range.
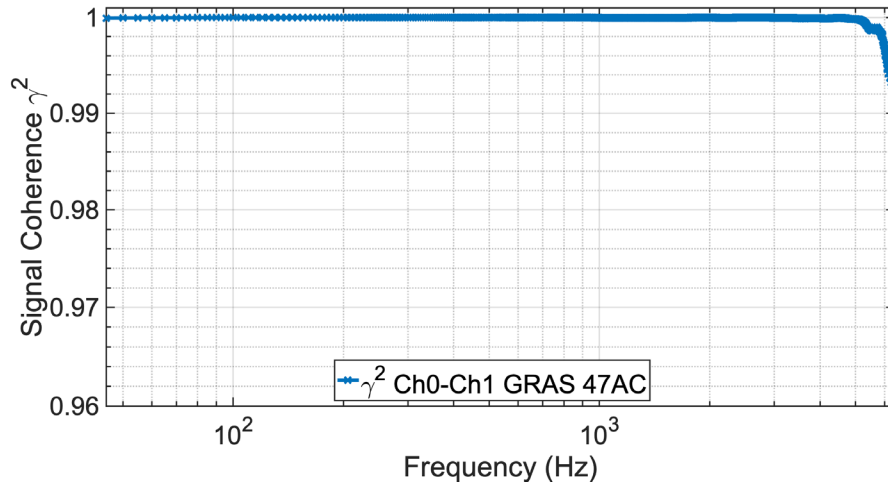
Figure 2.2.18 Coherence for one of the measurements using the intensity calibrator GRAS 51AB and GRAS 47AC microphones.

This method's primary purpose is to get the geometric mean of the transfer function for each pair combination, displayed in Figure 2.2.19 and Figure 2.2.20 for phase and amplitude, respectively. Although the intensity calibrator can go up to 6.4kHz, the purpose of this work will be limited to only up to 1kHz; therefore, the phase mismatch figures will only show up to 1 kHz.
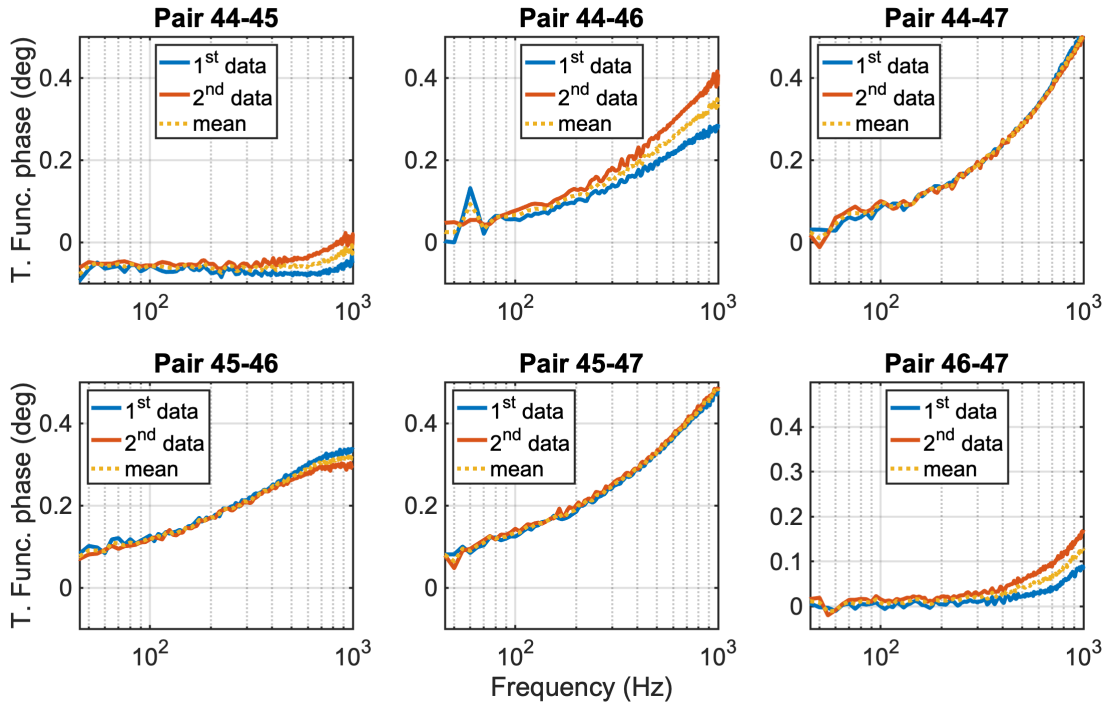
Figure 2.2.19 Phase of the geometric mean transfer function for each pair combination. 2 of 4 measurements are displayed and the mean.
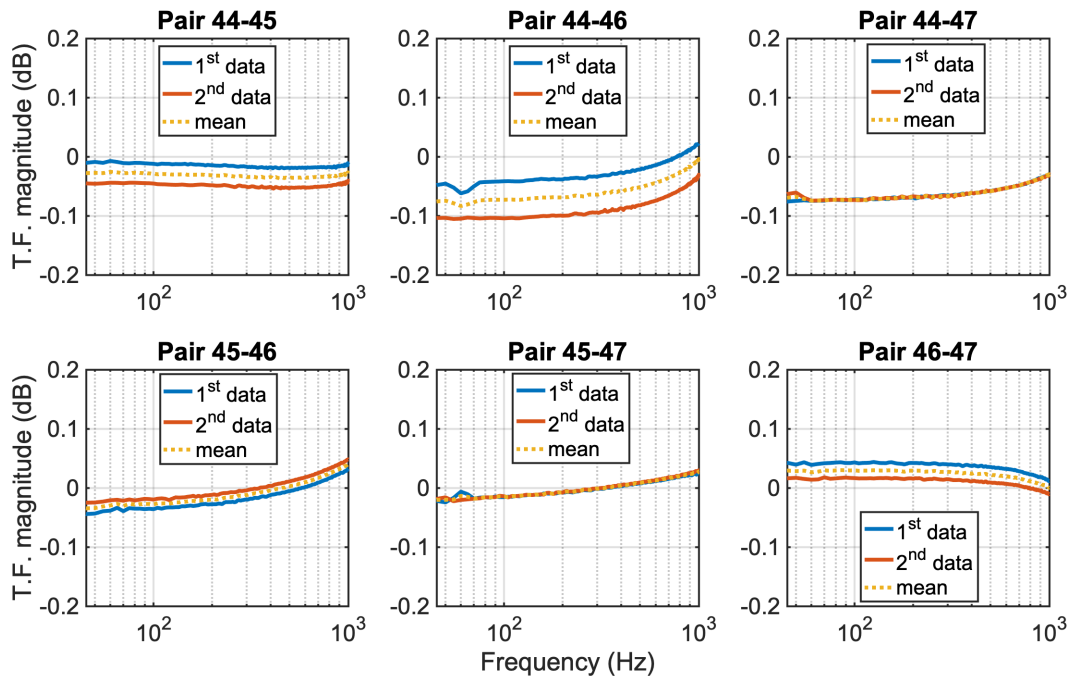
Figure 2.2.20 Geometric mean Transfer Function magnitude for GRAS 47AC pair.

34

The transfer function phase values are the instrument mismatch and are under 0.5˚ up to 1 kHz. Indeed, pair 44-45 is the best match for this frequency range having values lower than 0.05˚. Magnitude also shows a good match with values under 0.1 dB for the range analyzed.

2.2.5.2   46AE analysis

Coherence obtained from the 46AE measurements was close to one for all combinations. The first measurement coherence is shown in Figure 2.2.21. The coherence plot is consistent with the intensity calibrator expected field and with the previous 47AC coherence values
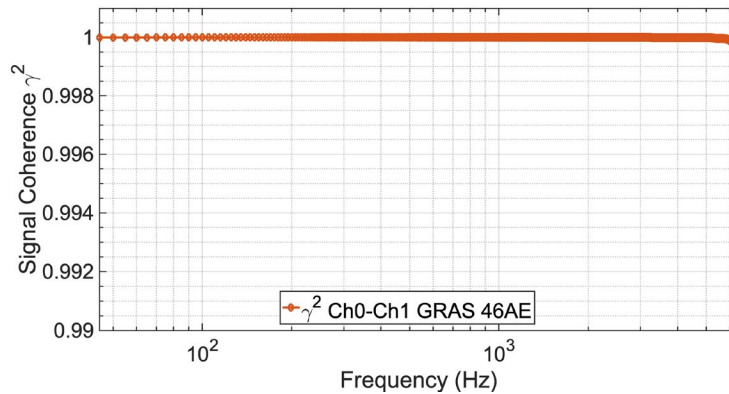
Figure 2.2.21 Coherence for one of the pair combinations using GRAS 46AE

The geometric mean transfer function for the 46AE microphone is shown in Figure 2.2.22 and Figure 2.2.23. There were 4 measurements, although only 2 are shown for simplicity and the mean for all measurements. GRAS 46AE microphones show a better match for this range compared to 47AC. The worst-case phase mismatch is pair B1-C2 at 1kHz with ~0.6˚. The other pairs show values lower than 0.4˚ and the best-matched pair is B2-C1 with values smaller than 0.05˚.
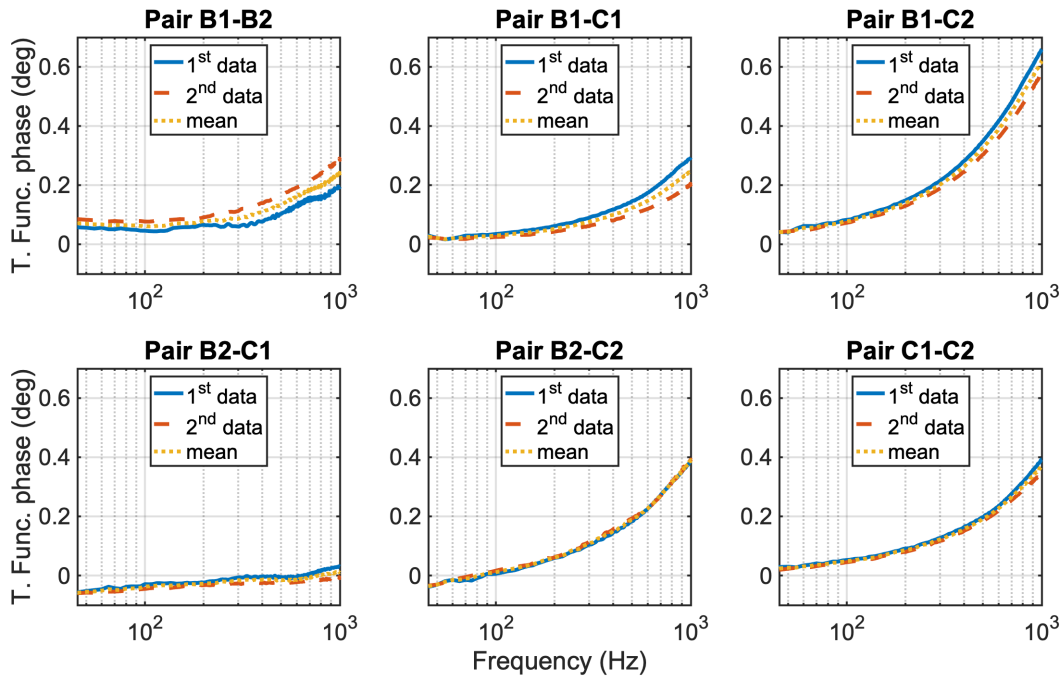
Figure 2.2.22 Phase of the geometric mean transfer function for pair combination of 46AE microphones
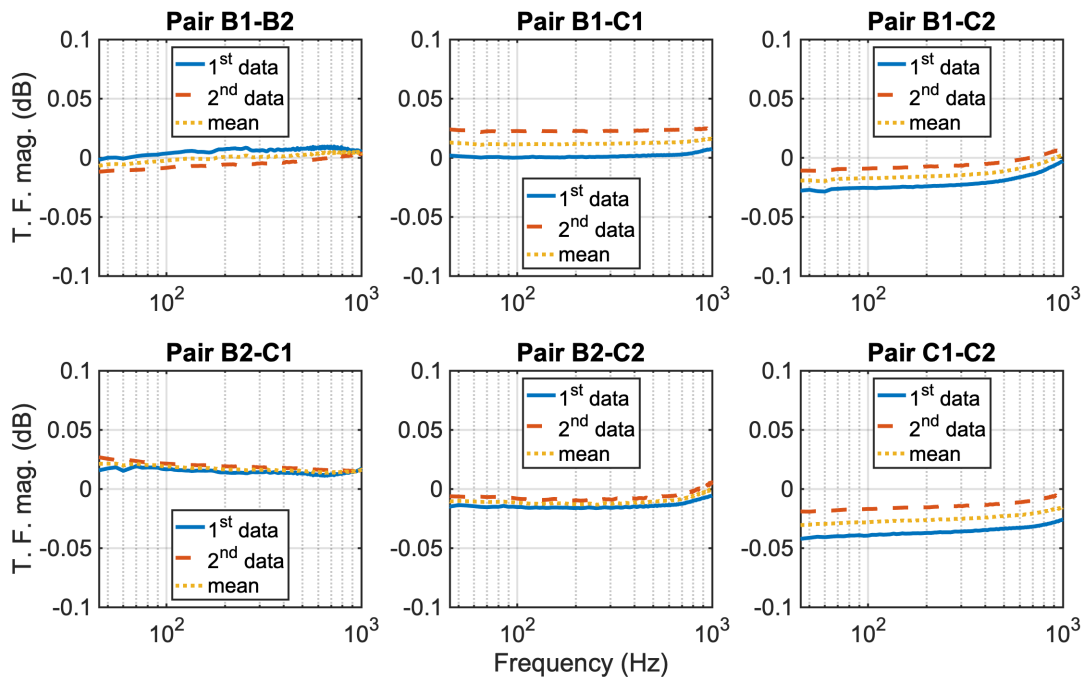
Figure 2.2.23 Geometric mean transfer function magnitude for pair combination of 46AE microphones on the intensity calibrator

36

2.2.6 Phase and amplitude correction

2.2.6.1   47AC broadband figure and math fit

The transfer function for phase and amplitude correction from 3 measurement methods is shown

in Figure 2.2.24 and Figure 2.2.25.
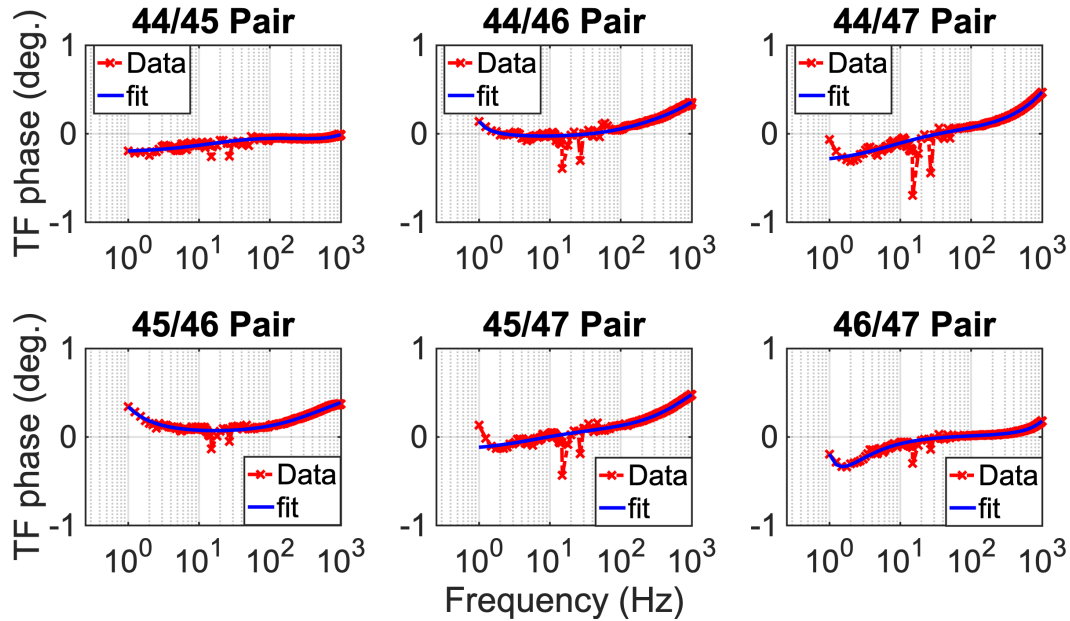
Figure 2.2.24 Fit function for transfer function phase, all pair combinations for GRAS 47AC

The fit was a rational function having different exponential for each combination. Table

2.2-2 shows the fit function.

Pair	Fit equation
44/45	$$\dfrac{.07523x^3 + .03469x^2 - .2794x - .2823}{x^2 + 5.266x + 4.959}$$
44/46	$$\dfrac{.05468x^3 + .4868x^2 - .884x - .4552}{x^2 + 3.148x + 2.322}$$
44/47	$$\dfrac{-18.07x^3 + 443.3x^2 + 1287x + 847.9}{x^2 + 3237x + 3896}$$
45/46	$$\dfrac{.5783x^2 + 1.433x + .8871}{x^2 + 4.056x + 3.395}$$
45/47	$$\dfrac{-.1108x^3 + 1.733x^2 + 5.395x + 3.746}{x^2 + 12.43x + 13.46}$$
46/47	$$\dfrac{.6482x^3 + 2.741x^2 + 3.662x + 1.569}{x^4 - 5.051x^3 + 7.556x^2 + 45.57x + 33.02}$$

Table 2.2-2 Fit functions for GRAS 47AC phase mismatch

Figure 2.2.25 shows the mismatch magnitude is below 0.2 dB, therefore the fit for magnitude mismatch is not considered.
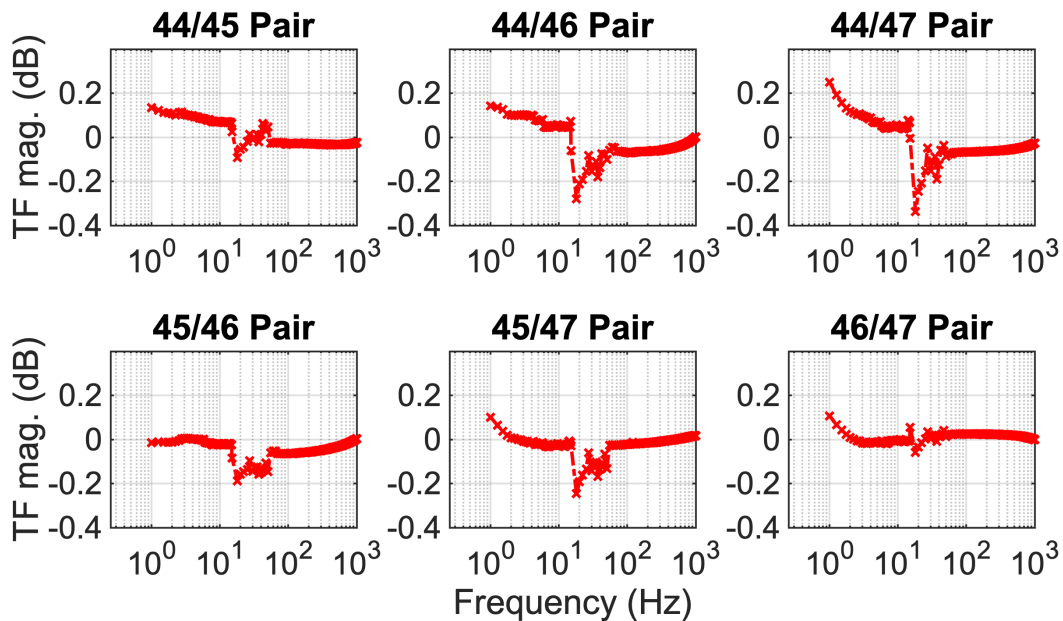
Figure 2.2.25 Transfer function magnitude with the 3 methods blend for the broadcast range up to 1kHz

38

Due to the shape of the mismatch and in order to analyze the lower band, the following exponential fit was done for the frequency range from 0.25 to 2 Hz.

Pair	Fit equation
44/45	$-.22e^{-.05x} + .01e^{-3.71x}$
44/46	$.092e^{-1.45x} + .007e^{-3.6x}$
44/47	$-19.1e^{-1.17x} + 18.9e^{-1.21x}$
45/46	$.322e^{-.526x} - .0123e^{-1.83x}$
45/47	$.361e^{-1.73x} - .326e^{-.512x}$
46/47	$.366e^{-1.74x} - .641e^{-.451x}$

Table 2.2-3 Fit equation for GRAS 47AC under 2 Hz

Fit plots are shown and compared to original data in Figure 2.2.26. The fits match closely to the original data along the range analyzed in this section.
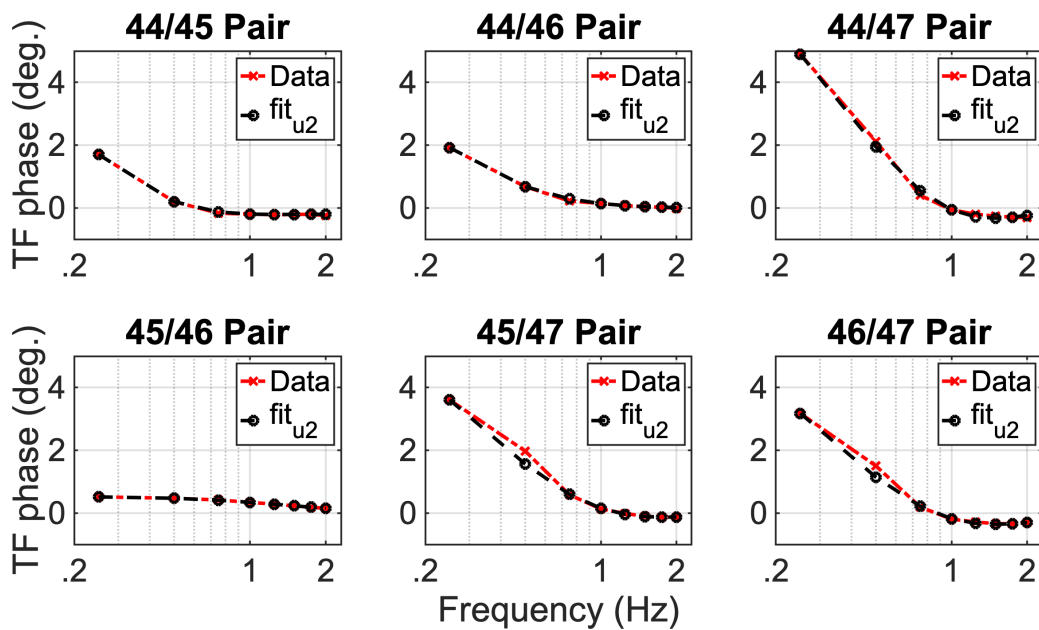
Figure 2.2.26 Transfer function phase under 2 Hz for GRAS 47AC

2.2.6.2 46AE broadband figure and math fit

Transfer functions representing the instrument mismatch for GRAS 46AE are shown in Figure 2.2.27 and Figure 2.2.28. Blend data for three frequency ranges are considered for each pair mismatch and compared with the corresponding fit function.
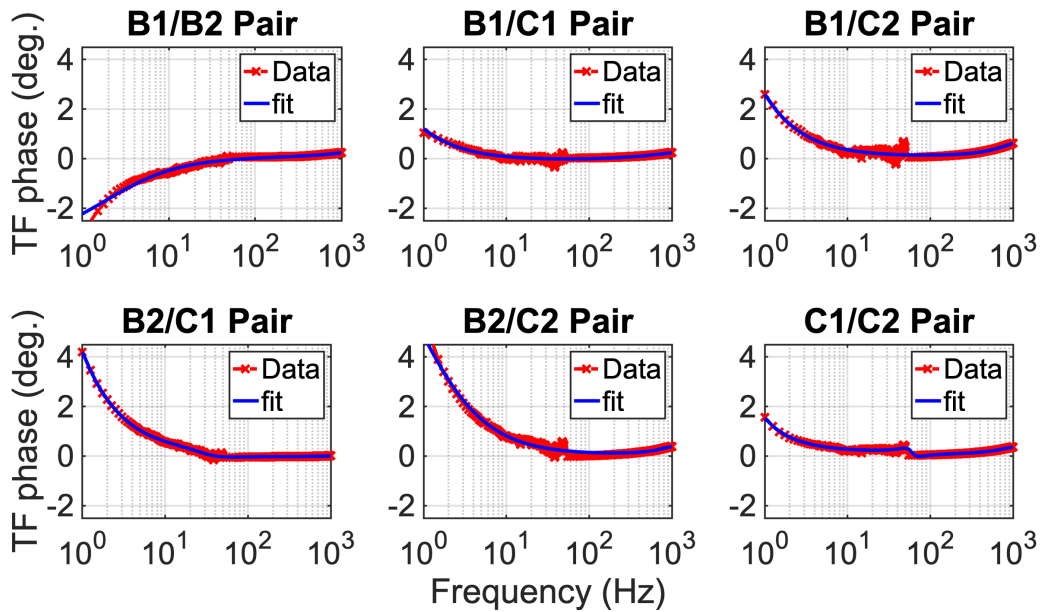
Figure 2.2.27 Transfer function phase for GRAS 46AE mismatch
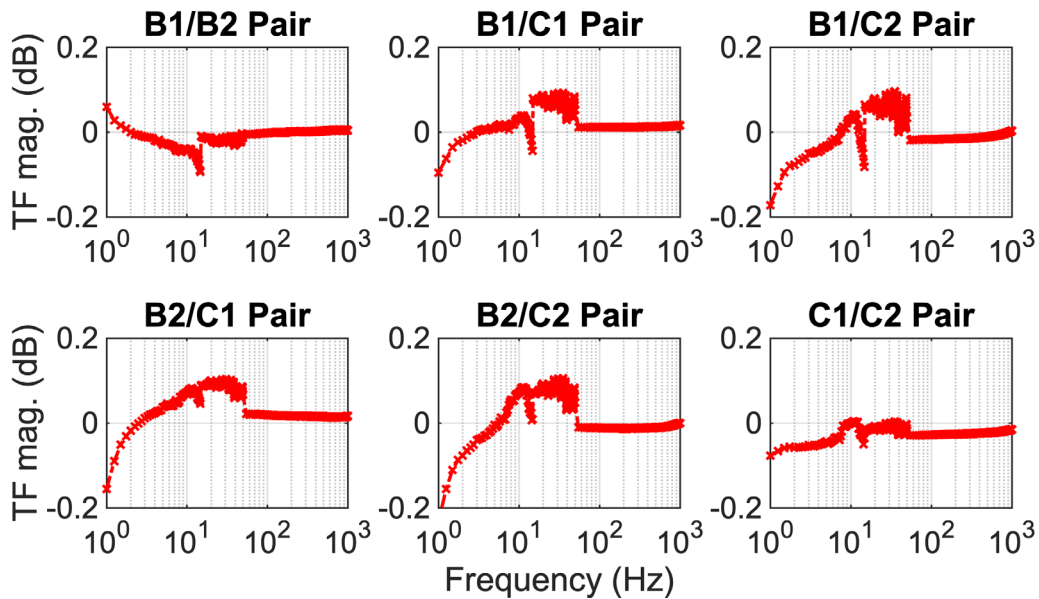
Figure 2.2.28 Transfer function magnitude for GRAS 46AE mismatch

40

The magnitude mismatch is considerably low for this set of microphones; therefore, no fit function for the magnitude is calculated.

Table 2.2-4 shows the following equations for the rational functions fit for each pair.

Pair	Fit equation
B1/B2	$$\dfrac{1440x^2 + 4088x + 1949}{x^2 + 25220x + 21830}$$
B1/C1	$$\dfrac{.6545x^2 + .8468x + .2642}{x^2 + 6.119x + 4.526}$$
B1/C2	$$\dfrac{1.356x^2 + 3.816x + 2.441}{x^3 - 3.481x^2 + 10.43x + 12.18}$$
B2/C1	$$\dfrac{-.01736x^2 - .03104x - .01341}{x^5 + 1.047x^4 - .118x^3 + .9496x^2 + 1.855x + .7159}$$
B2/C2	$$\dfrac{.257x^2 + .9615x + .9882}{x^3 - 3.653x^2 + 4.99x + 7.661}$$
C1/C2	$$\dfrac{1.294x^3 + 2.76x^2 + 1.933x + .4455}{x^5 - 2.668x^4 + .2798x^3 + 13.38x^2 + 13.38x + 3.717}$$

Table 2.2-4 Fit functions for GRAS 46AE phase mismatch

The lower band is analyzed separately in order to cover the shape of the mismatch, the following exponential fit was done for frequency range from 0.25 to 2 Hz.

Pair	Fit equation
B1/B2	$-2.81e^{-.612x} - .091e^{1.14x}$
B1/C1	$-35.7e^{-.683x} + 36.7e^{-.671x}$
B1/C2	$2.37e^{-.440x} + .0021e^{2.84x}$
B2/C1	$3.75e^{-.496x} + .0755e^{1.22x}$
B2/C2	$5.13e^{-.546x} + .107e^{1.28x}$
C1/C2	$1.37e^{-.656x} + .0253e^{1.45x}$

Table 2.2-5 Fit function for GRAS 46AE under 2 Hz

Plots for the transfer function phase fits are shown and compared to original data in Figure

2.2.29. The fit match closely to the original data along the range analyzed in this section.
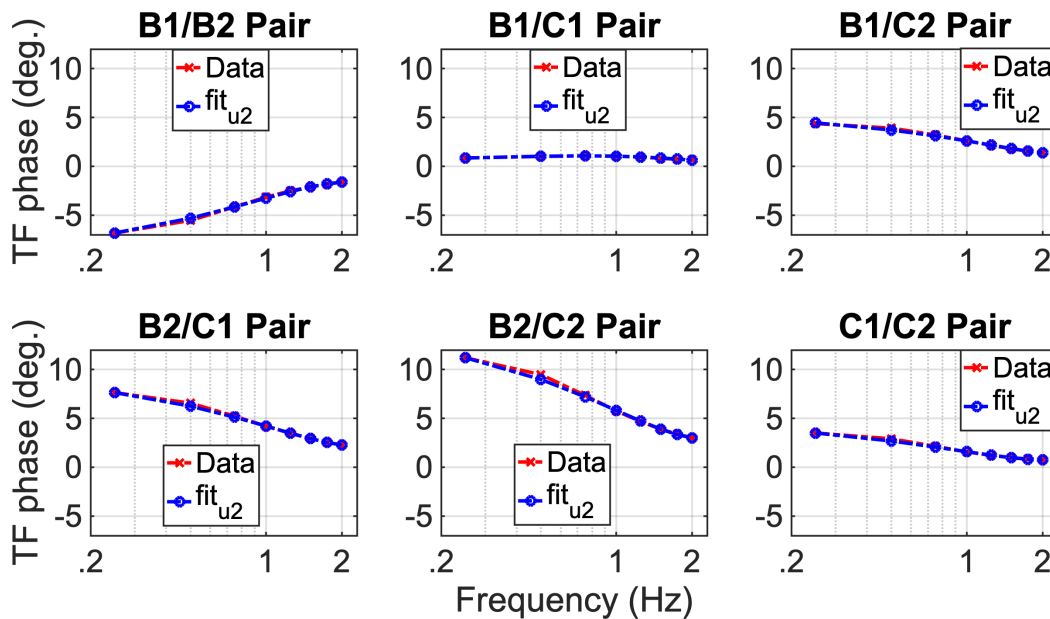
Figure 2.2.29 Fit under 2 Hz for GRAS 46AE for the transfer function phase

2.2.6.3 Frequency resolution effects

The frequency resolution is a trade-off situation. A fine frequency resolution is often desirable for infrasound to see characteristics below 20 Hz. The fine frequency resolution introduces noise because of the smaller number of averages when applying the FFT. Therefore, a longer data set is required, a challenge for infrasonic sources available for research. Figure 2.2.30 shows an example of the frequency resolution effect on the autospectra obtained from a static test of a rocket motor.
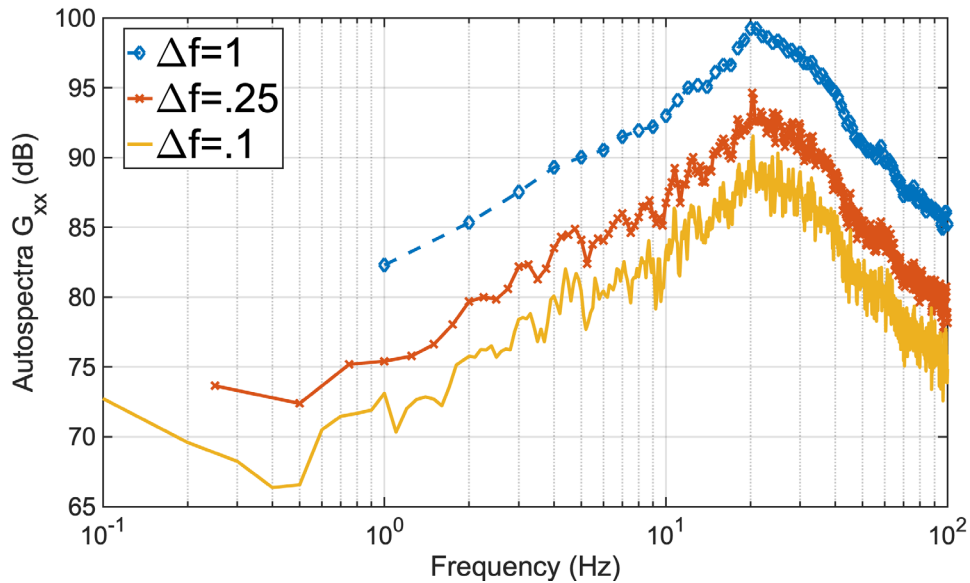
Figure 2.2.30 Frequency resolution effect on autospectra from rocket static test.

The effect of having a better frequency resolution is the noise addition. In this plot, the impact on the levels caused by the energy distribution along the bins for different frequency resolutions is visible. For a coarser frequency resolution, the levels are higher because of the energy distribution, although the total energy remains the same.

43

2.3 Verification measurement

2.3.1 Overview

This section shows the mismatch measurement using a different acoustic source and comparing to the car experiment.

2.3.2 Balloon as an acoustic source

The acoustic field is generated by the massive volume of air displaced by the expansion from the combustion of propane gas. Cycling the burner on and off at a certain period can produce an infrasonic source at any desired frequency. The acoustic approximation for this field is a monopole centered at the burner, as shown in Figure 2.3.1. The on and off cycle conducted was one second burn and 2 seconds idling.
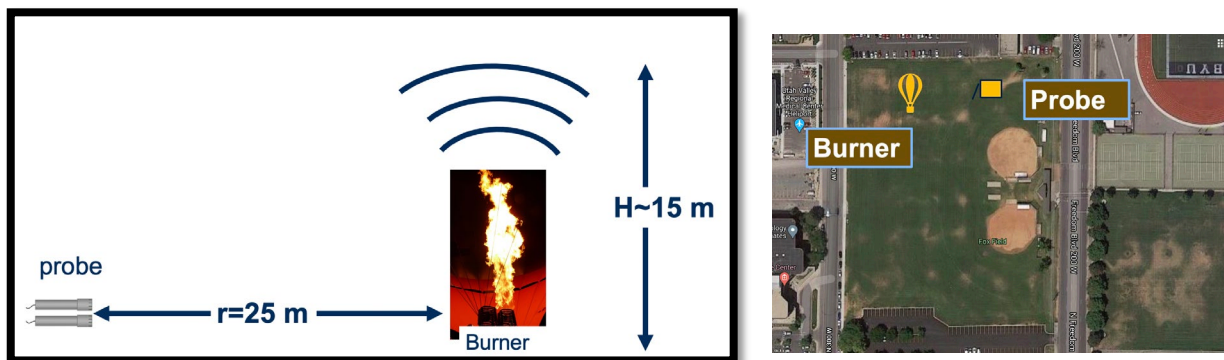
Figure 2.3.1 Gas burner sketch. A monopole is the acoustic source approximation

2.3.2.1 Near field intensity errors

Lawrence et al.[34] estimate near field errors are proportional to the ratio of the distance to the source over the microphones spacing r/d. For a 4-microphone probe, a ratio greater than 2.15 gives an error level that is going to be under 0.2 dB. According to Whiting et al.[35] the intensity error level is given by

$$\frac{I^{PAGE}}{I} = \left(\frac{1}{1-\beta^2/4}\right)^2 \qquad \qquad \textit{Equation 2.3-1}$$

In this equation the term β refers to the ratio between microphone distance d and the radius to the source r,

$$\beta = d/r \approx \frac{.075}{29} \approx .0026 \qquad \qquad \textit{Equation 2.3-2}$$

The values for this setup give an estimate intensity error of 15×10^{-6} dB. In this case the assumption made regarding the ratio between the wavelength and microphone distance is still valid.

2.3.3 Balloon measurement

2.3.3.1 Setup, source and weather condition

The measurements were made in an open field to reach a plane wave field. There was a zero to very low wind condition; this supposes the source located vertically above the flames and negligible wind noise. The microphones were placed on a reflective board and surrounded by a thick windscreen shown in Figure 2.3.2. This setup is made following the measuring work[36,37]. The probe was the same in the car experiment: line abreast array and the maximum distance between the microphone is ~6 diameters. Also, the microphones were aligned to be perpendicular to a radial line for equal excitation conditions. For this case, the distance to the source was ~29 m considering a straight line from the source to the probe.
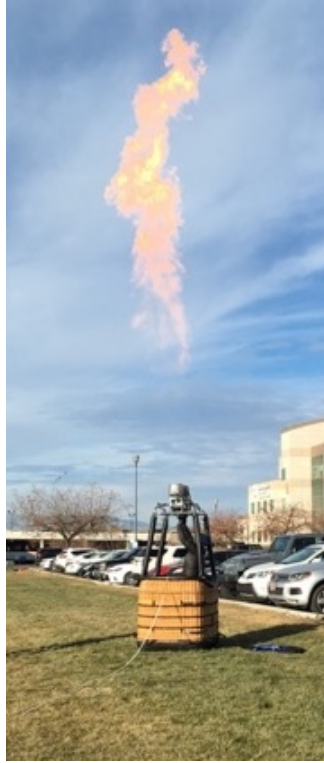
Figure 2.3.2 Left: Burner picture. Right: Microphone probe configuration with reflective board and windscreen.

2.3.4 Results

A total of 6 data set were measured for each microphone set. Autospectra and coherence plots showed good consistency between channels and between each measurement. Coherence is near to 1 from 0.5 Hz and up to 1 kHz for all the measurements. Frequency resolution for figures shown in this section is 0.1 Hz.

2.3.4.1 Sound Pressure Level, Coherence & Transfer Function for GRAS 47AC

The autospectra for six measurements are shown in Figure 2.3.3. Although the period was set to be 3 seconds, the fundamental frequency found is not an exact multiple of the designed period. This fact is due to the burner cycle has a decaying delay until it reaches its idle state.
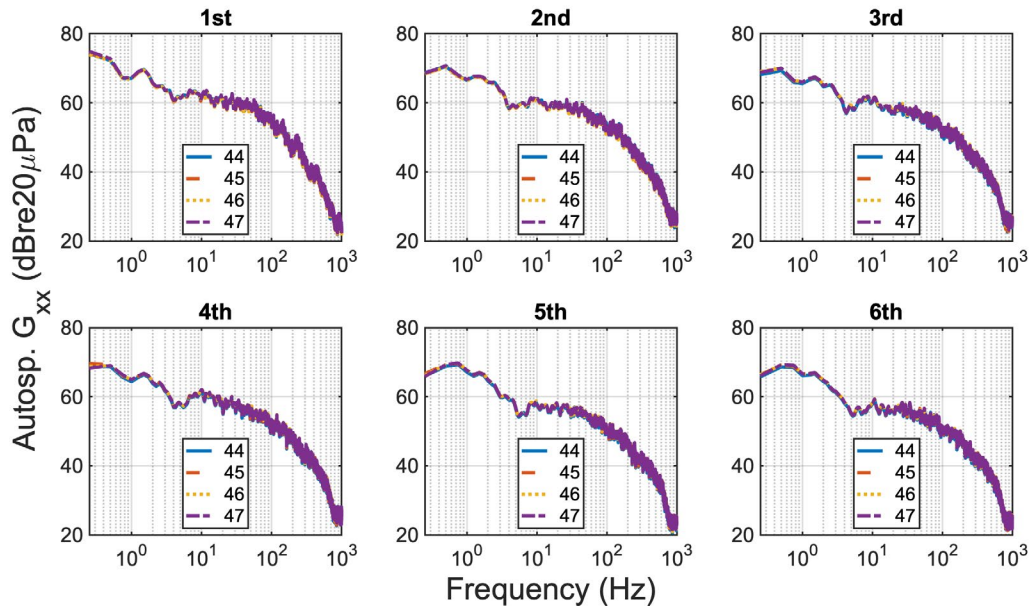
***Figure 2.3.3 GRAS 47AC autospectra from the burner field calibration. Six measurements
and 4 channels for each microphone***

Coherence is shown in Figure 2.3.4. Values are close to one for most of the range shown.

Each subplot corresponds to different measurement time and each line corresponds to the different

pair combination.
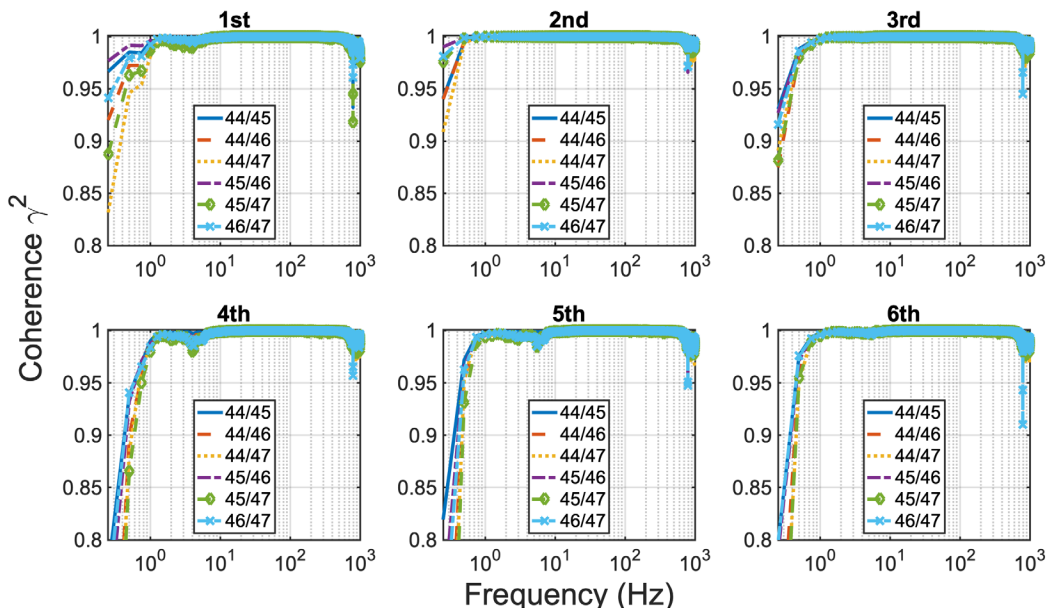
***Figure 2.3.4 GRAS 47AC coherence from six measurements at the burner calibration. Each
line represent each pair combination***

47

Figure 2.3.5 and Figure 2.3.6 show the transfer function for the six pair combination at each subplot. Besides the six measurement times are represented for the different lines.
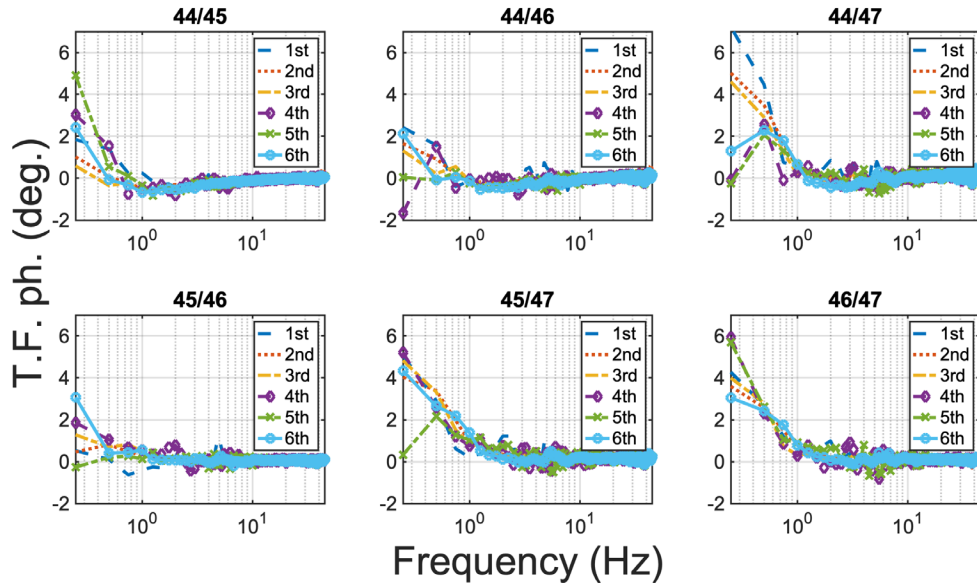
Figure 2.3.5 GRAS 47AC phase mismatch at the burner experiment. Six pair combination with the different measurement time.

Transfer function plots (phase and magnitude) represents the instrument mismatch for the GRAS 47AC microphone set.
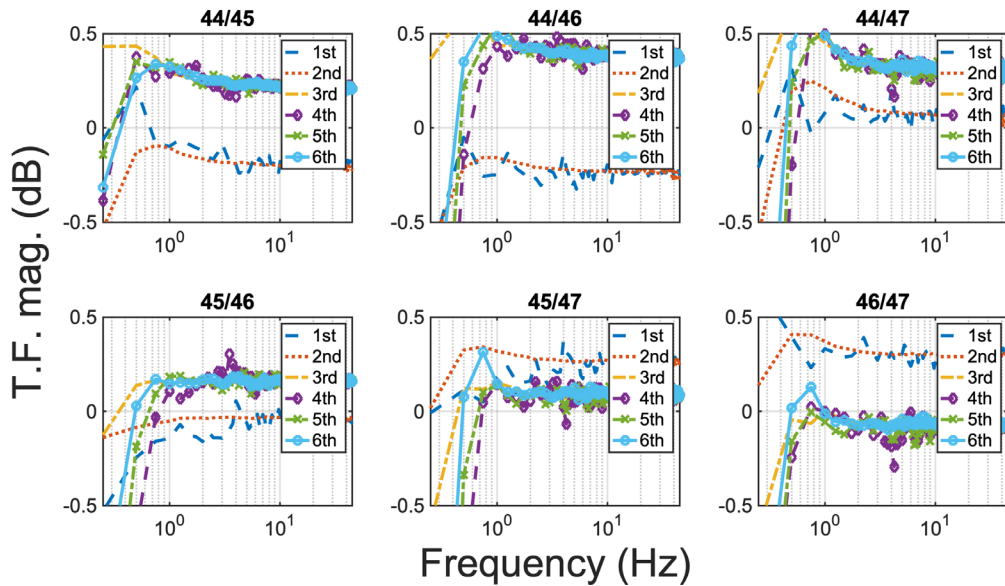
Figure 2.3.6 GRAS 47AC magnitude mismatch. Six pair combination with six measurements.

2.3.4.2 Sound Pressure Level, Coherence & Transfer Function GRAS 46AE

Similar procedure was done with the GRAS 46AE microphones. Autospectra and coherence are shown in Figure 2.3.7 and Figure 2.3.8 respectively.
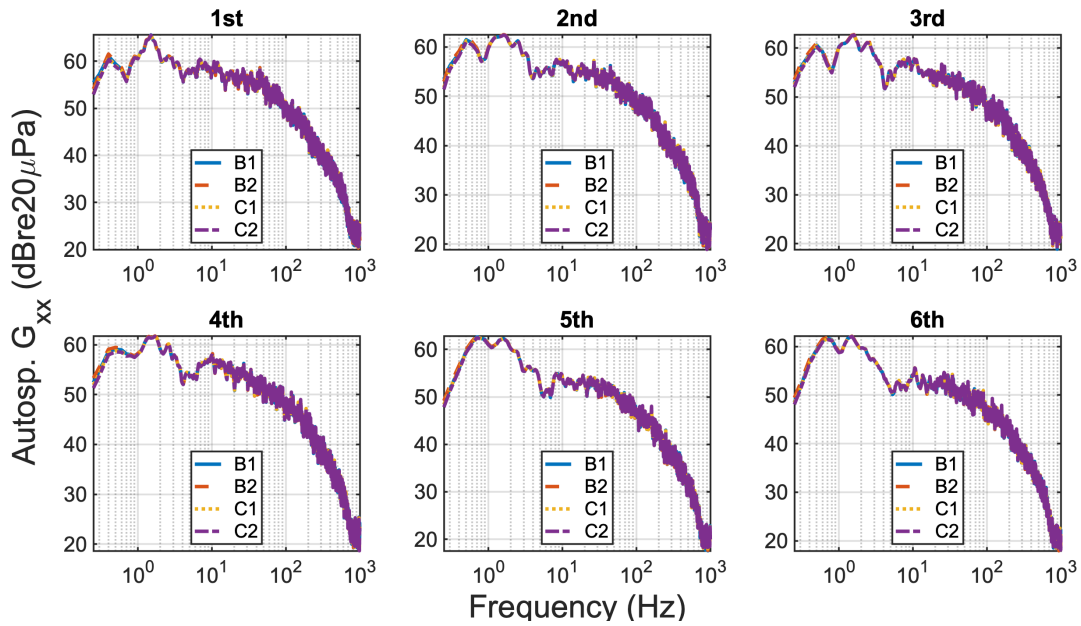
Figure 2.3.7 GRAS 46AE Autospectra. Six measurement times and 4 channels.

49
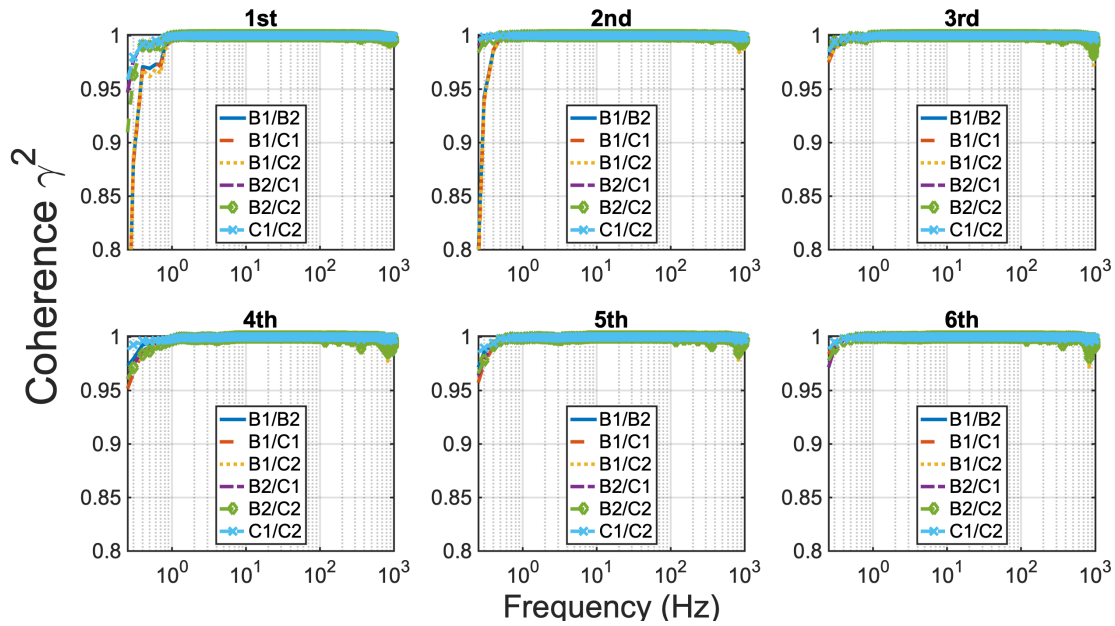
Figure 2.3.8 GRAS 46AE Coherence. Six measurement times and 6 pair combinations

Transfer function phase and magnitude are shown in Figure 2.3.9 and Figure 2.3.10 respectively. These plots represent the instrument mismatch for the burner experiment.
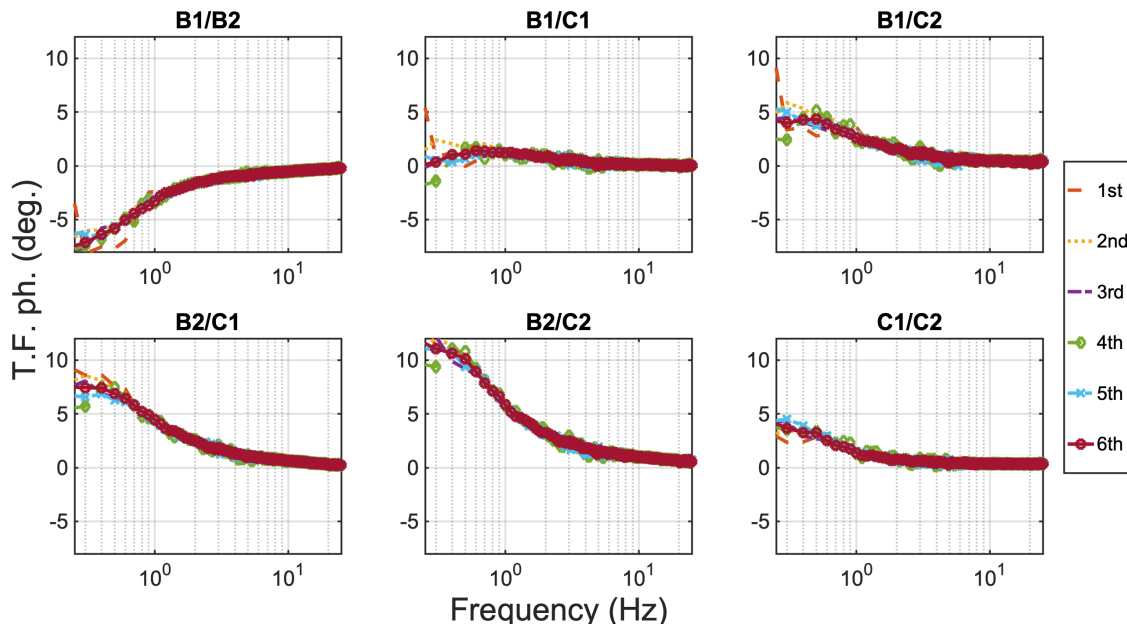
Figure 2.3.9 GRAS 46AE transfer function phase for instrument mismatch, results from burner calibration. Each subplot is the corresponding pair combination, and the lines represents the measurement time.
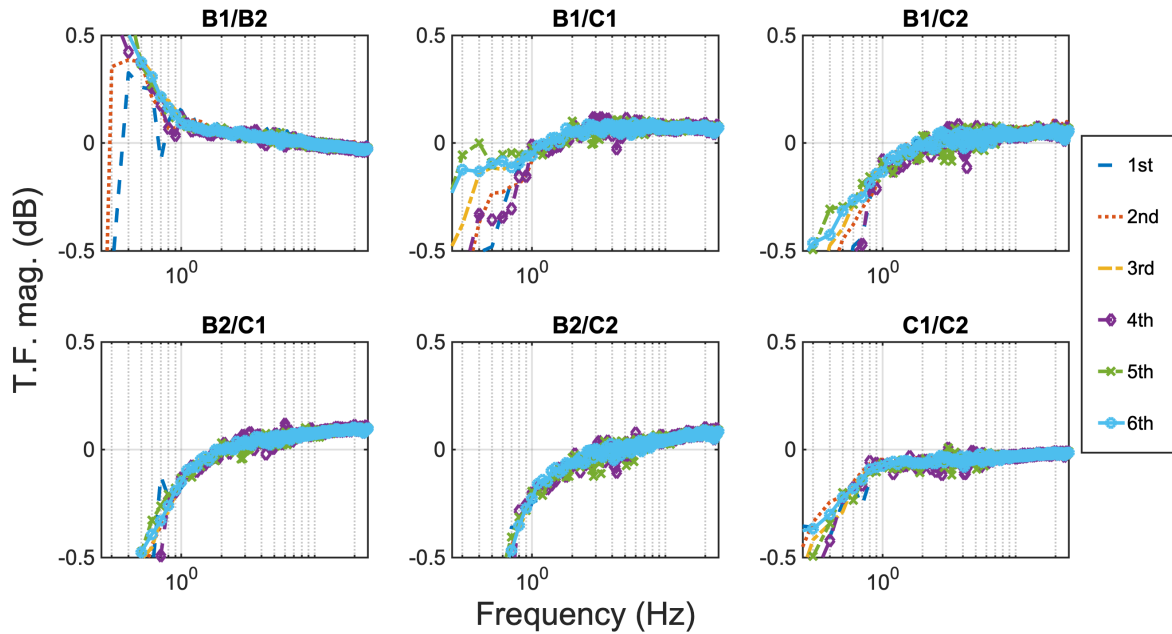
Figure 2.3.10 GRAS 46AE transfer function magnitude for instrument mismatch, results from burner calibration. Each subplot is the corresponding pair combination and the lines represents the measurement time.

2.3.5 Comparison between 2.2.6 and 2.3.4

Results from this section proved the concordance between the burner and the car experiment. The quantity to compare is the transfer function obtained for all pair combinations for the 2 sets of microphones and the 2 experiments.
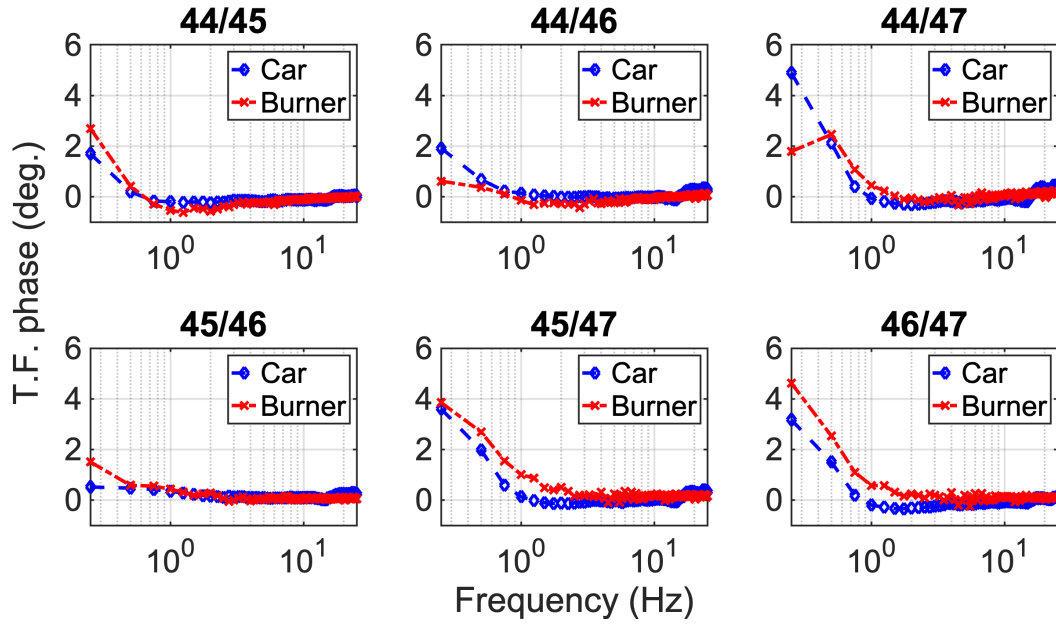
Figure 2.3.11 GRAS 47AC pairs: Phase mismatch for two sources under an equal excitation calibration
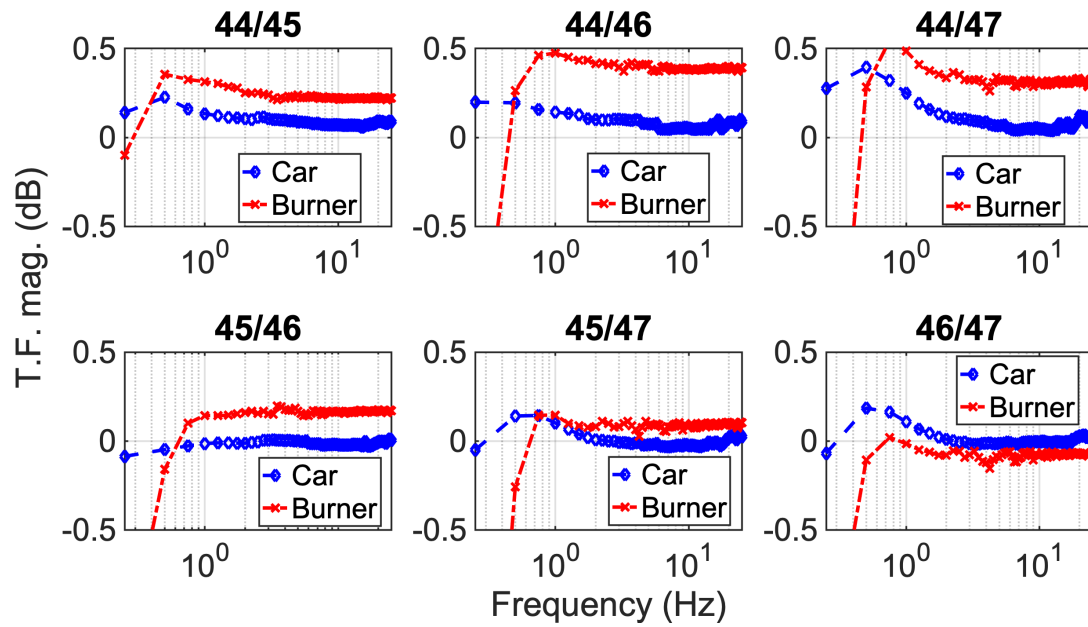
Figure 2.3.12 GRAS 47AC pairs: Magnitude mismatch for two sources under an equal excitation calibration

52
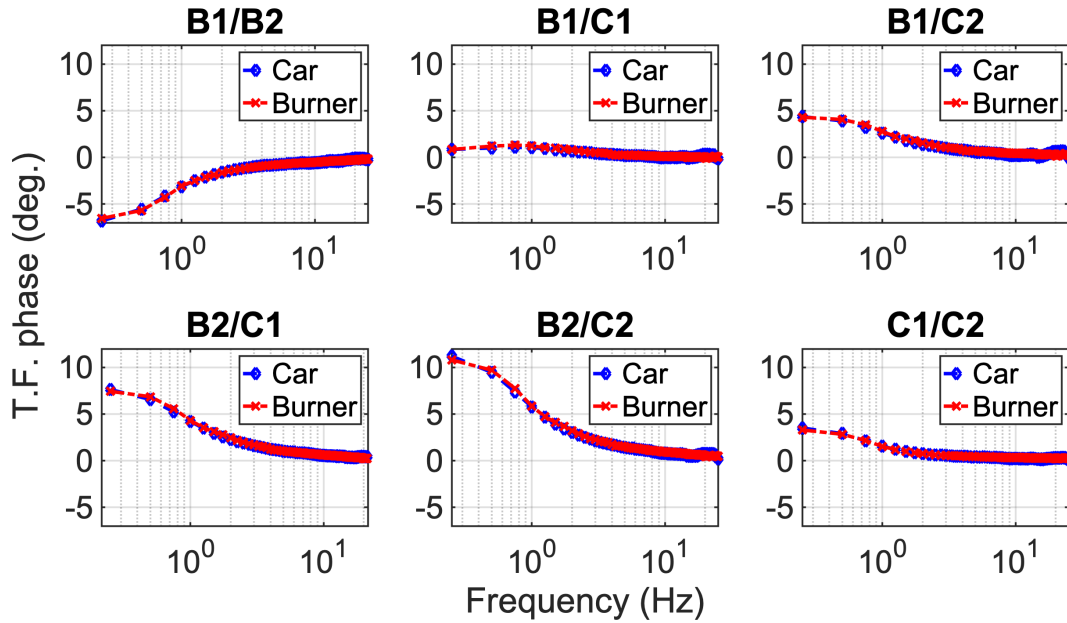
Figure 2.3.13 GRAS 46AE pairs: Phase mismatch for two sources under an equal excitation calibration
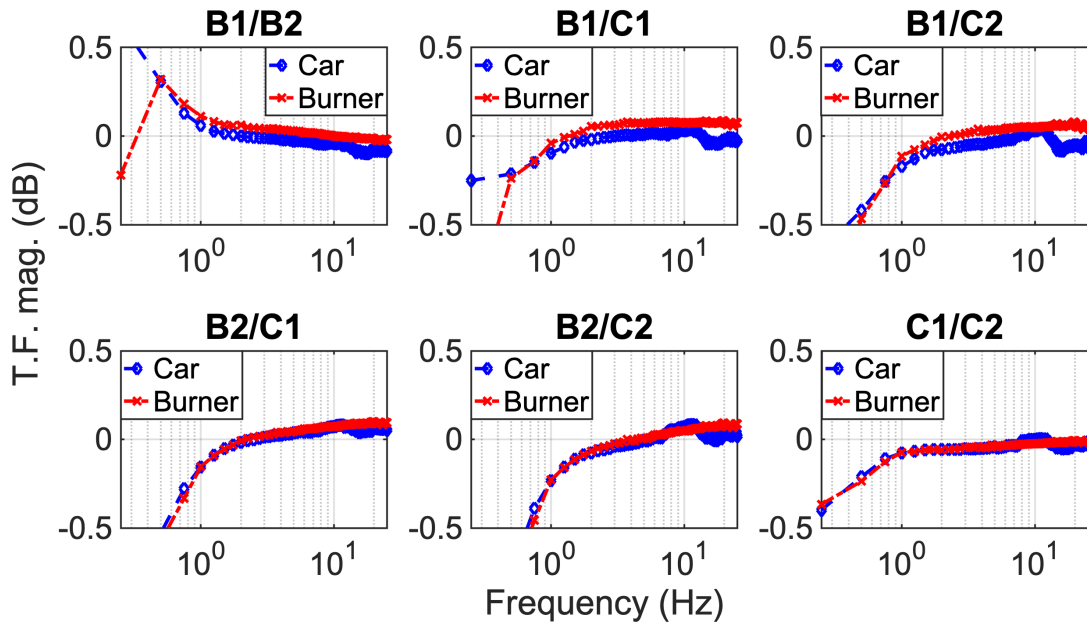
Figure 2.3.14 GRAS 46AE pairs: Magnitude mismatch for two sources under an equal excitation calibration

53

These results show a close similarity between the instrument mismatch obtained from both sources. Phase mismatch for both microphone models displayed a stable behavior and concordant for 2 different infrasound sources. Magnitude mismatch was lower for the car experiment for both models; nevertheless, the 46AE has a better match than the 47AC.

2.4 Conclusion

The instrument calibration consisted of 3 methods for each frequency range. The results will correct the instrument mismatch for each pair of microphones over a broadband range. Chapters 3 and 4 will show the application of the instrument calibration for outdoor infrasonic intensity measurements.

The infrasonic calibration, shown in Figure 2.4.1, was made only with a coherence higher than 0.99. This conservative criterion is made to assure the experimental infrasonic source level for calibration made using the moving vehicle.
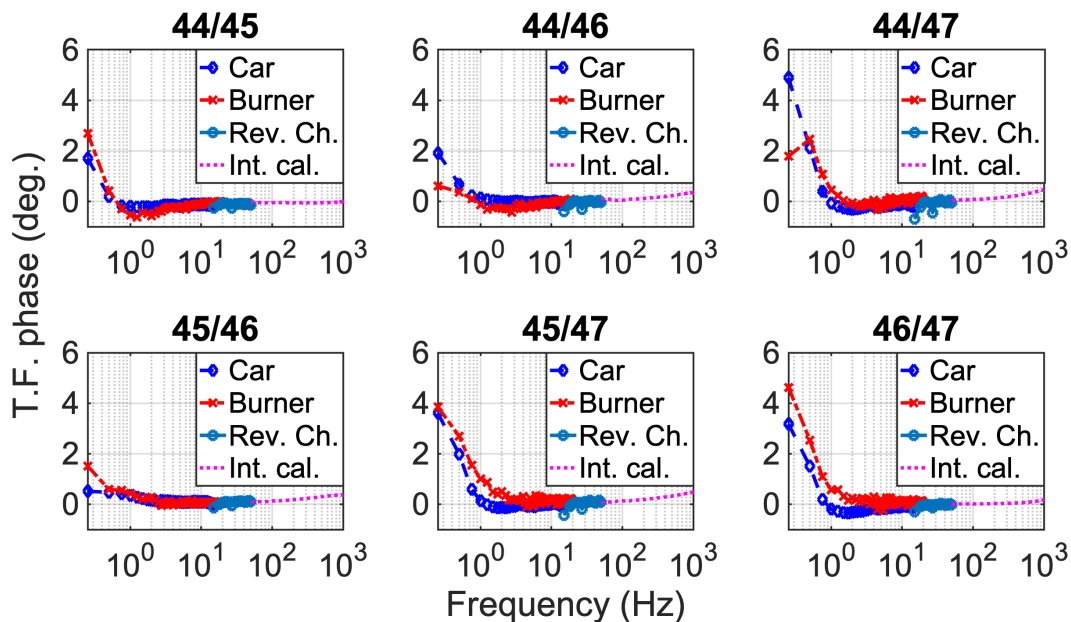
Figure 2.4.1 Final phase mismatch for GRAS 47AC

The phase mismatch shown in Figure 2.4.1 has a good agreement between the three methods. The reverberation chamber data has a dip at 27 Hz, as was shown in section 2.2.4. The drop at this point is associated with the room mode causing interference. The frequency resolution for the first segment (0.25-16.25Hz) is 0.25 Hz, where a slight difference between the burner and the car measurements can be noticed. All pairs have a decaying curve from zero to 1 Hz. Also, this curve is steeply showing a rapid change in phase at these low frequencies. For higher frequencies, the curve values are all near to zero.
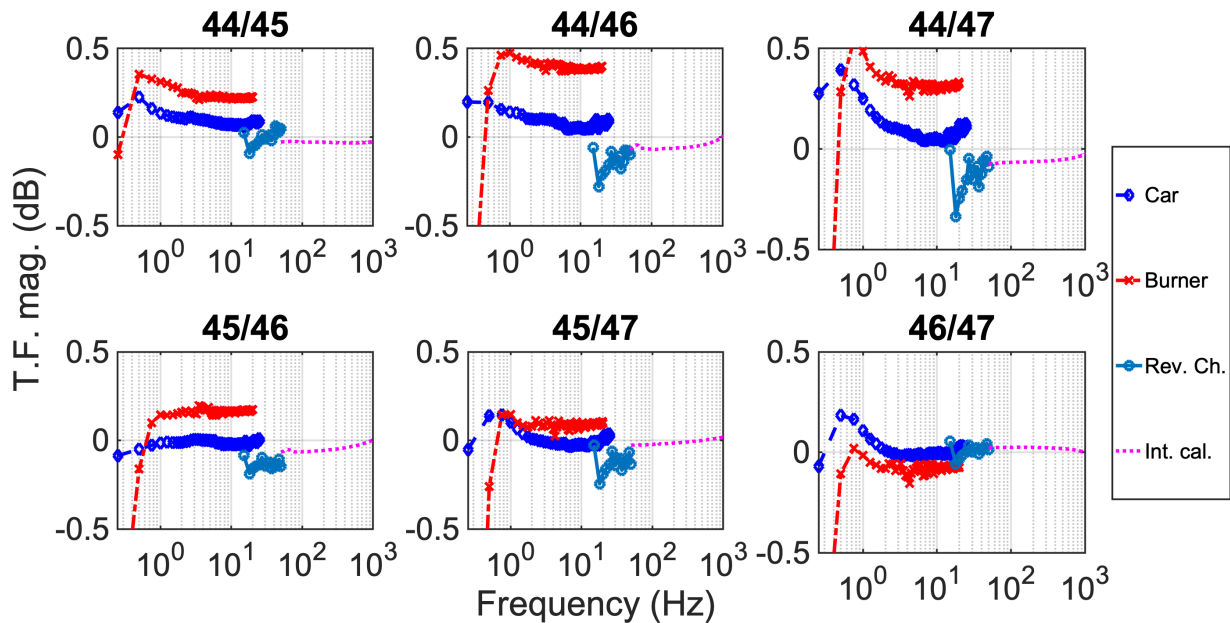
Figure 2.4.2 Final amplitude mismatch for GRAS 47AC

Figure 2.4.2 and Figure 2.4.4 shows the magnitude mismatch is under 0.5 dB for all the pairs and for all frequency range.
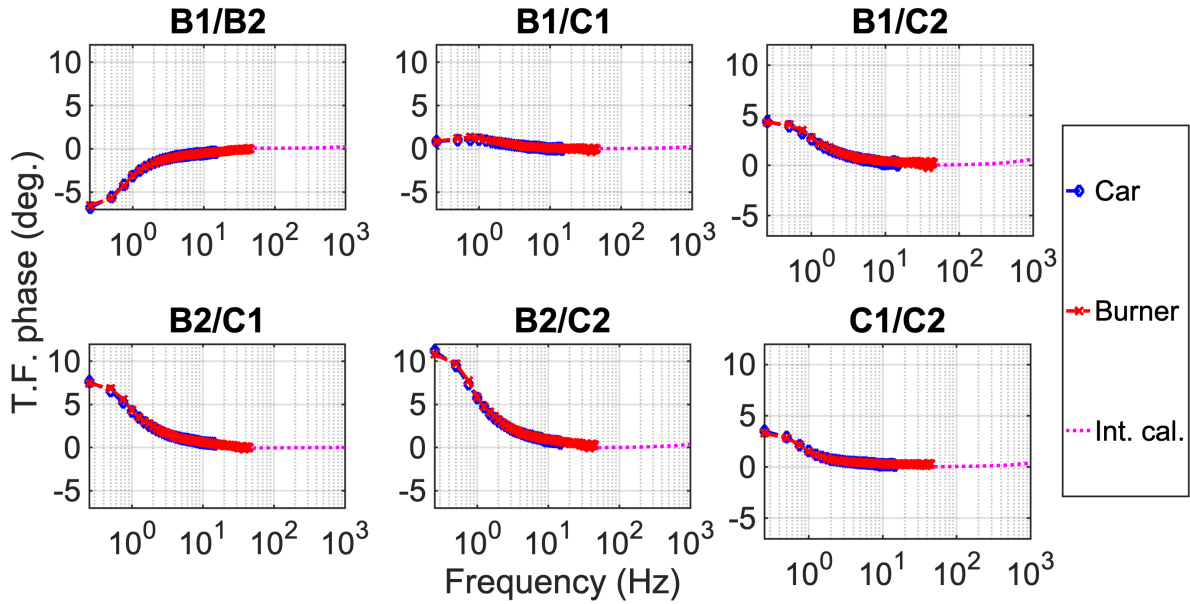
Figure 2.4.3 GRAS 46AE final phase mismatch
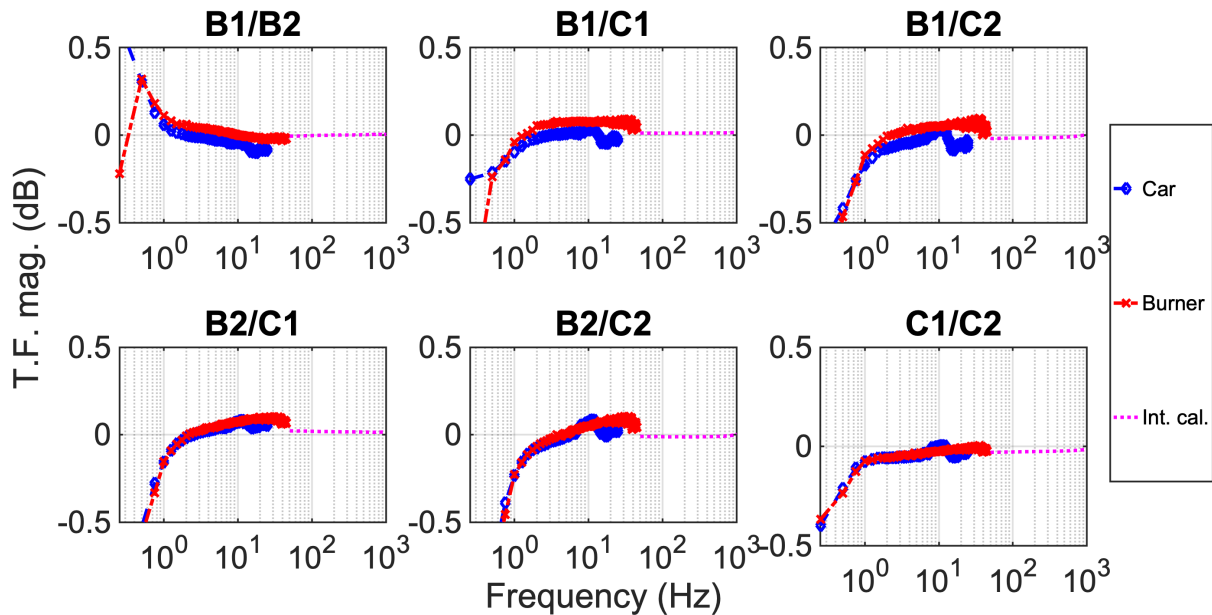
Figure 2.4.4 GRAS 46AE final magnitude mismatch

GRAS 46AE does not include the low audio frequency range for this project since the GRAS 46AE microphone set was phase-matched previously.

The infrasonic range method is limited because it assumes that the wavelength should be two orders of magnitude greater than microphone distance. Also, limitations could arise from

56

measurement's uncertainty. Several showed values of uncertainty larger than 6° for the phase mismatch from the 15 recordings. The uncertainty brings the need to make several recordings and remove low coherence data points. Finally, a fine frequency resolution is needed for the infrasonic calibration, which implies longer recordings and presenting a measuring challenge.

3 Chapter 3: Application of relative calibration to infrasound intensity measurements on hot air balloon gas burner field

3.1 Introduction and Overview

This chapter demonstrates validation of the correction proposed to the instrument mismatch found in Chapter 2. This validation requires a controlled acoustic field generated by an infrasonic source to compare intensity calculations. The validation compares intensity direction and magnitude from the known source orientation, with and without applying the instrument mismatch correction.

The source selected for this validation is a hot air balloon burner similar to the experiment conducted by Smith and Gabrielson[30]. The theoretical approach is a monopole centered at the line over the flames. The expansion during the propane gas combustion moves the air and combustion gases at different velocities generating a broadband source. Although in this case, the idea is to create a pulse with a frequency in the infrasound regime.

3.1.1 Experiment Setup

The burner used was a Cameron Balloons Ultra double burner with liquid pilot lights. This unit was manufactured in 2011. The valve operation has two modes, the main blast valve, and the whisper valve. The main blast valve produces a blue-streamlined flame over 5 meters in length; this is generally used to inflate the balloon and during flight. The whisper valve delivers a golden flame, and it is helpful for the quiet operation option, and it delivers two-thirds of the power of the main burner. In this experiment, the main blast valve operation was selected. A reference manual says the output power is 24 million Btu at 100 psi and a noise level of 99 dBA measured at 45 cm

58

below the burner. The probes were located at a distance of 7 and 8.8 meters to the burner, as shown in Figure 3.1.1. There were two orthogonal intensity probes and two models of microphones, namely GRAS 46AE and GRAS 47AC. The probe radius sizes were 0.25 and 0.5 meters spacing, respectively.
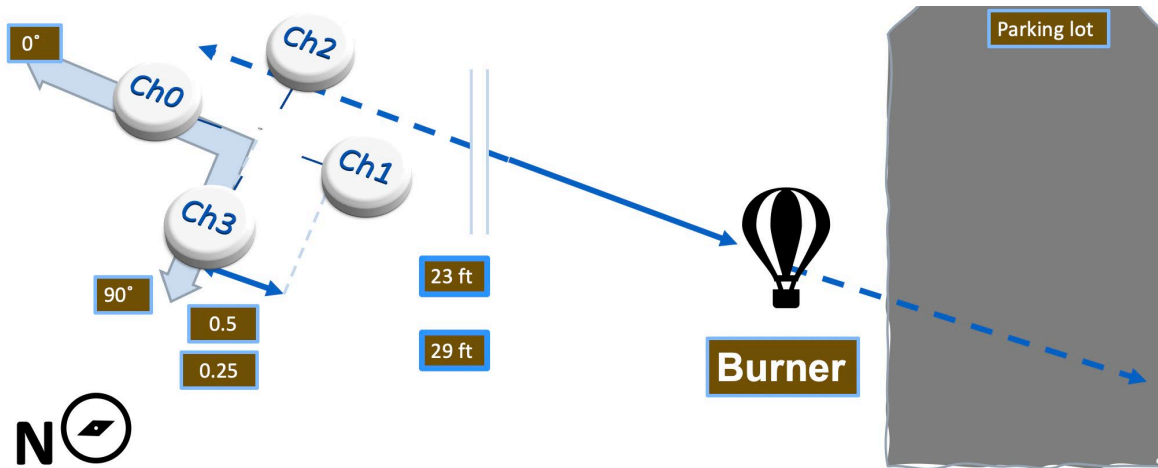
Figure 3.1.1 Burner field sketch. Two orthogonal intensity probes were used, one with 0.5 m spacing and the other with 0.25 m spacing. Axis selected was aligned to the source (0˚) and tangential (90˚).

The location was an open field cover by grass, and it was surrounded by a parking lot, medium traffic streets, and buildings, as shown in Figure 3.1.2. This configuration places the probes in the near field for an infrasound wave, as is shown in Figure 3.1.2. The recording was 1-minute length having a sequence of 1 second with the burner on and 1 second off. The off-cycle is shown on the left side, and the right shows the on-cycle. The burner was mounted on the hot air balloon basket with an approximate height of 6.5 feet. The expected intensity direction is zero or close to zero.

www.manaraa.com

Figure 3.1.2 Experiment setup, there are two probes, both are aligned to have a zero-degree intensity direction. Left: Burner off cycle. Right: Burner on cycle.

The measurements were done at dusk with an ambient temperature of 6°C and zero wind speed at the moment of recording. All the weather data was taken with a Kestrel 4500 weather meter.

3.1.2 Acoustic Signal from burner

Figure 3.1.3 shows the time data signal. The burst pulses create a short response of an approximately 1-second length. The pulse is not regular in amplitude or length, although the average over-the-minute length recording shows the peak for 0.5 Hz fundamental corresponding to the 2 second period. Besides, the amplitude irregularity shows the evidence of the field characteristics, which is not perfectly anechoic. Also, the burner operation was done manually with the aid of an audible pulse cue.
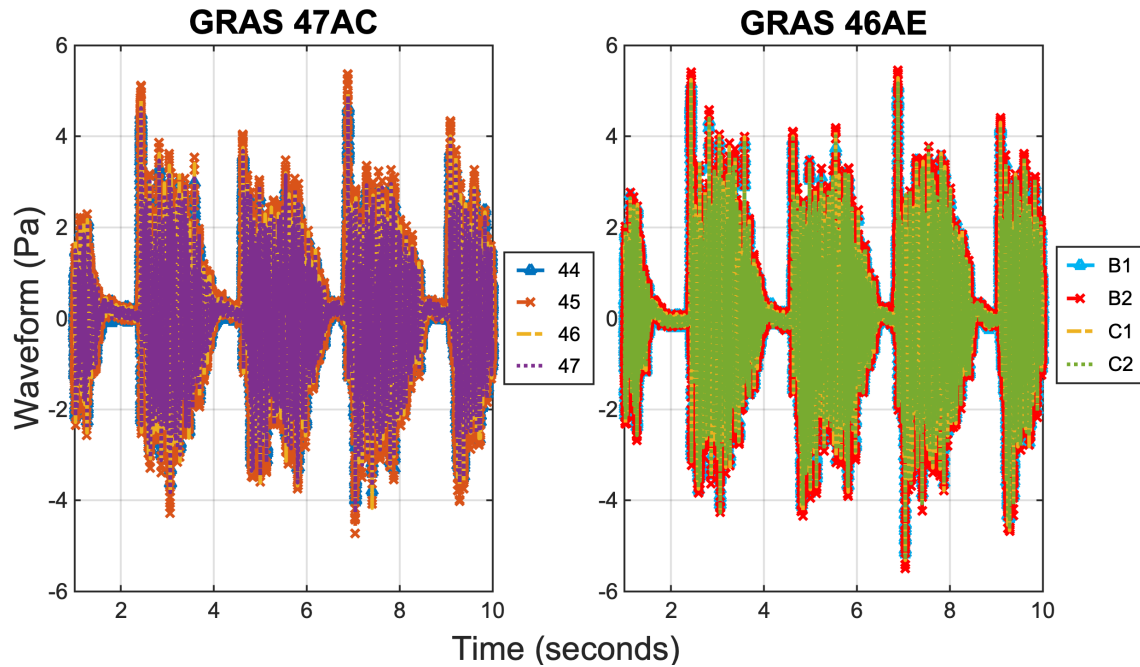
Figure 3.1.3 Signal in the time domain. Left: GRAS 47AC microphones measurement. Right: GRAS 46AE time signal.

Figure 3.1.4 shows the autospectra for both microphone sets, with a frequency resolution of 0.25 Hz. The recording length was 58 seconds and 50% of overlapping, giving 28 averages. The spectra show higher levels at the fundamental frequency for the GRAS 47AC compared to the GRAS 46AE. The sensitivity for 47AC microphones is specially designed for low-frequencies giving a higher amplitude.
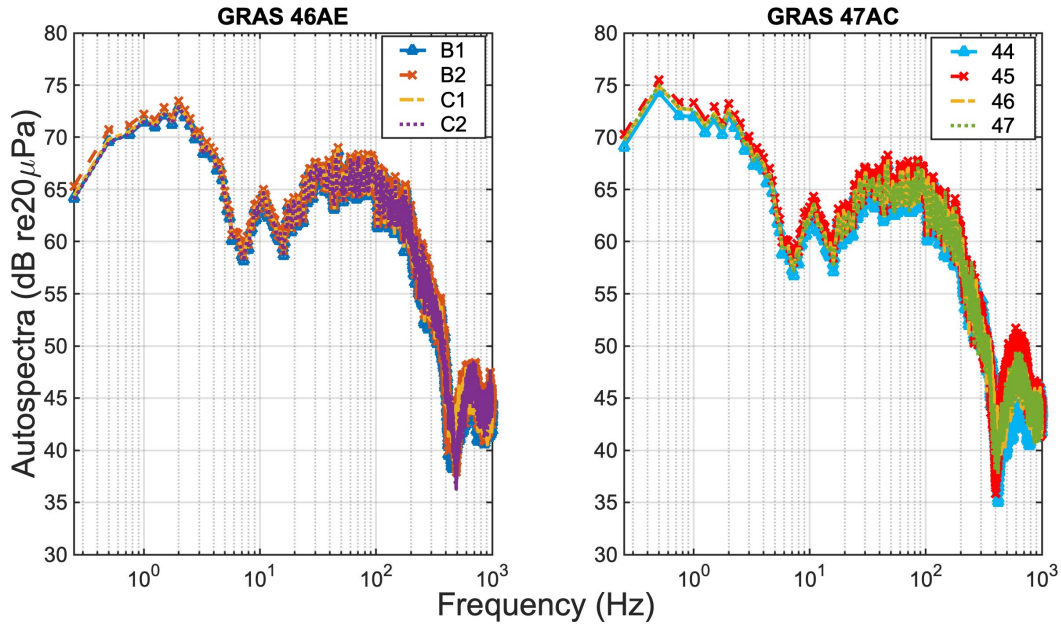
Figure 3.1.4 Burner Signal in the frequency domain with a resolution of 0.25 Hz. Left: Spectra for GRAS 46 AE microphone set. Right: GRAS 47AC spectra

3.2 Results: GRAS 47AC with 0.5-meter probe

The coherence and autospectra for the GRAS 47AC and 0.5-meter probe are shown in Figure 3.2.1, the fundamental at 0.5 Hz shows a spectral level of 75 dB with 20×10^{-6} Pa reference. Coherence is near to 1 for the infrasonic range and up to 60 Hz. The spectral level below 0.5 Hz shows a steep roll-off, meaning that these low frequencies' wind noise is minimal. Zero wind speed is related to this fact.
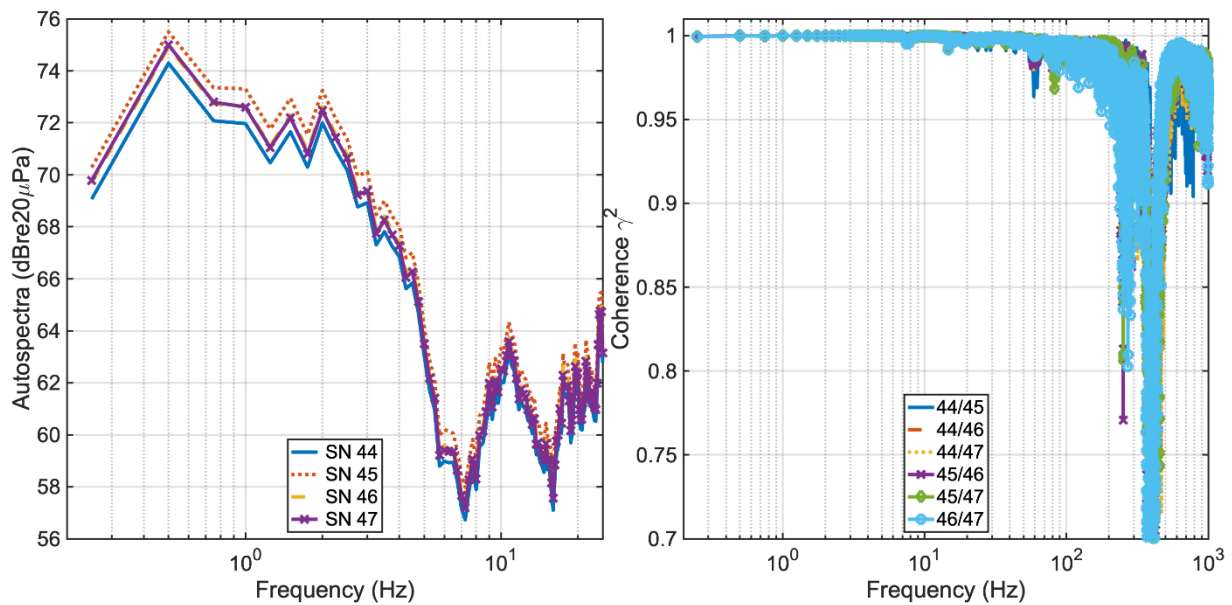
Figure 3.2.1 Autospectra and coherence for burner measurements using GRAS 47AC and 0.5-meter spacing probe.

The autospectra shown in Figure 3.2.1 covers only the infrasonic range to highlight the signal peaks with the fundamental at 0.5 Hz and visible harmonics up to 5 Hz. From this point and above, a new broader peak appears centered at ~11 Hz, and the harmonics for the first fundamental start to mask and merging with a more broadband signal.

The ambient noise level shown in Figure 3.2.2 is under the signal harmonics levels for the whole frequency range analyzed, giving a desirable broadband signal-to-noise ratio. The ambient recording was taken before the experiment for 103 seconds.

63
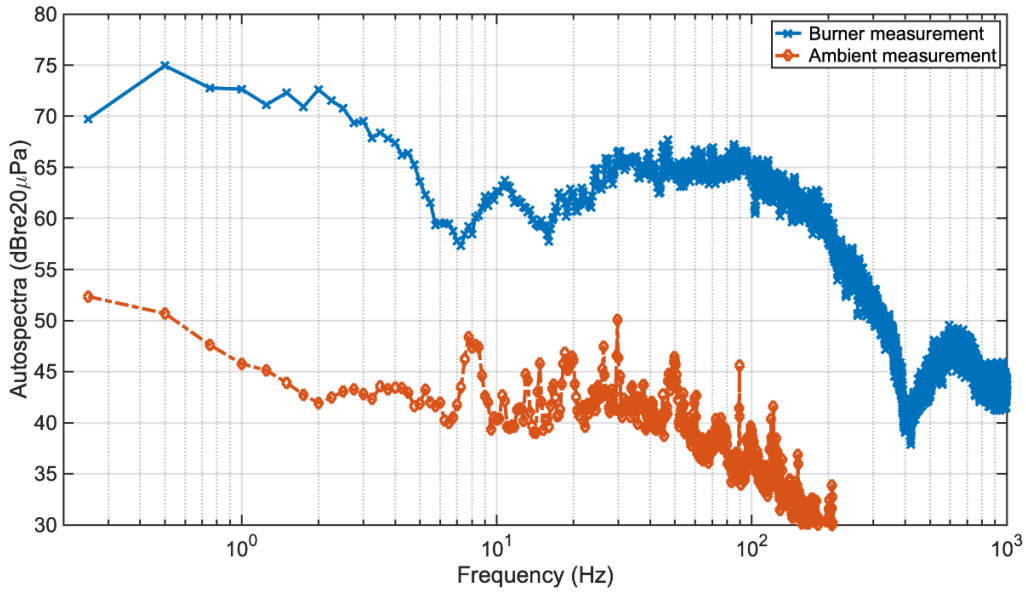
Figure 3.2.2 Ambient recording spectra compared with burner spectra. The ambient noise level is around 20-25 dB down which is low compared with the levels shown by the signal.

Intensity calculations for GRAS 47AC microphones using a frequency resolution of 0.25 Hz are shown in Figure 3.2.3. Here the dotted-blue line with diamond markers shows the calculations with the calibration applied. The dash-orange line with x markers is the intensity direction with no correction applied.
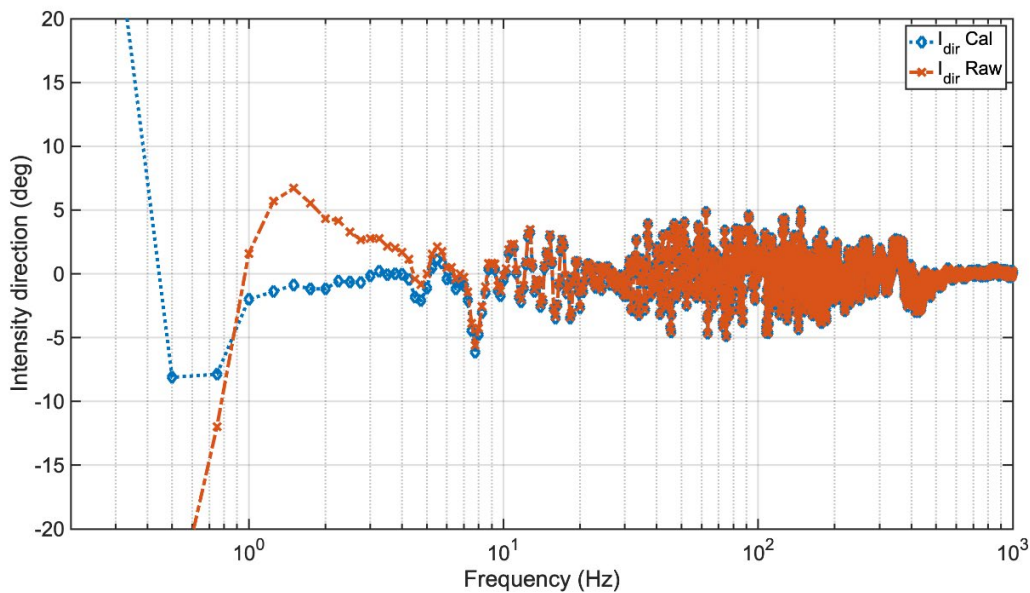
Figure 3.2.3 Intensity calculation for Burner with GRAS 47AC and 0.5-meter probe. Intensity direction for the 0.2Hz-1kHz range, logarithmic scale, and 0.25 Hz frequency resolution

The calibration application shows an improvement for the fundamental and its harmonics values. For example, raw data shows an intensity direction of 25° at 0.5 Hz; meanwhile, the corrected value is 8°, having an error reduction of 17°. The direction is expected to be 0° ±3°. The following harmonics corrections are ~3.0° for 1 Hz and ~6.6° for 1.5 Hz. The correction data improves over the raw data up to 5 Hz, having a slight difference from raw data after 5 Hz. This fact is caused by the decrease of the instrument phase mismatch at higher frequencies.

Figure 3.2.4 shows the magnitude calculations for this experiment. The blue line corresponds to the calibrated data, the dashed-red line is the data without calibration and the dotted yellow line is the autospectrum level.
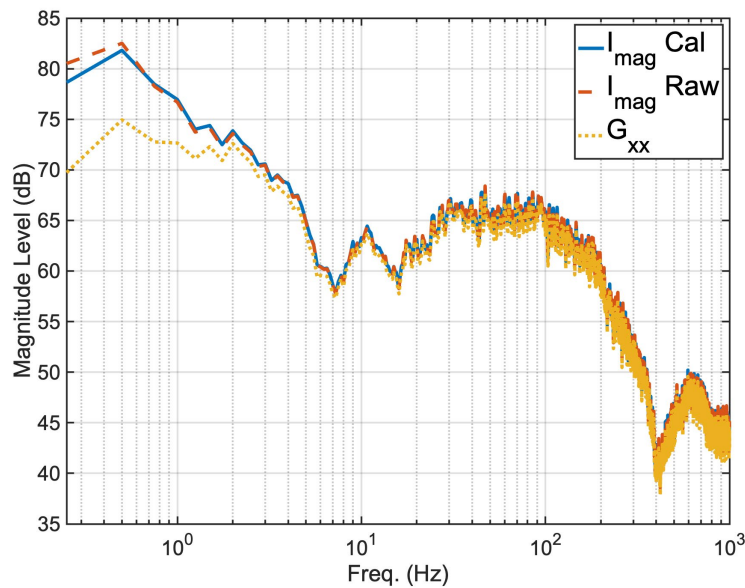
Figure 3.2.4 Intensity magnitude for Burner with GRAS 47AC microphones in the 0.5-meter spacing probe

In this case, intensity magnitude correction doesn't show a difference with the raw data, as is shown in Figure 3.2.4. At the fundamental frequency, the autospectral level shows a difference of ~7 dB with intensity magnitude, and this difference decreases with the following harmonics

down to ~0.8 dB at 5 Hz. The error source is related to the near field effects combined with microphone mismatch below 2 Hz, although this needs further revision.

3.3 Results: GRAS 46AE with 0.25-meter probe

The autospectra and coherence plots for GRAS 46AE microphones are shown in Figure 3.3.1. These plots look pretty consistent with the ones shown in Figure 3.2.1, although in this case, the peak is at 2 Hz. The frequency roll-off causes the higher peak value for these microphones, which is ~3 Hz.
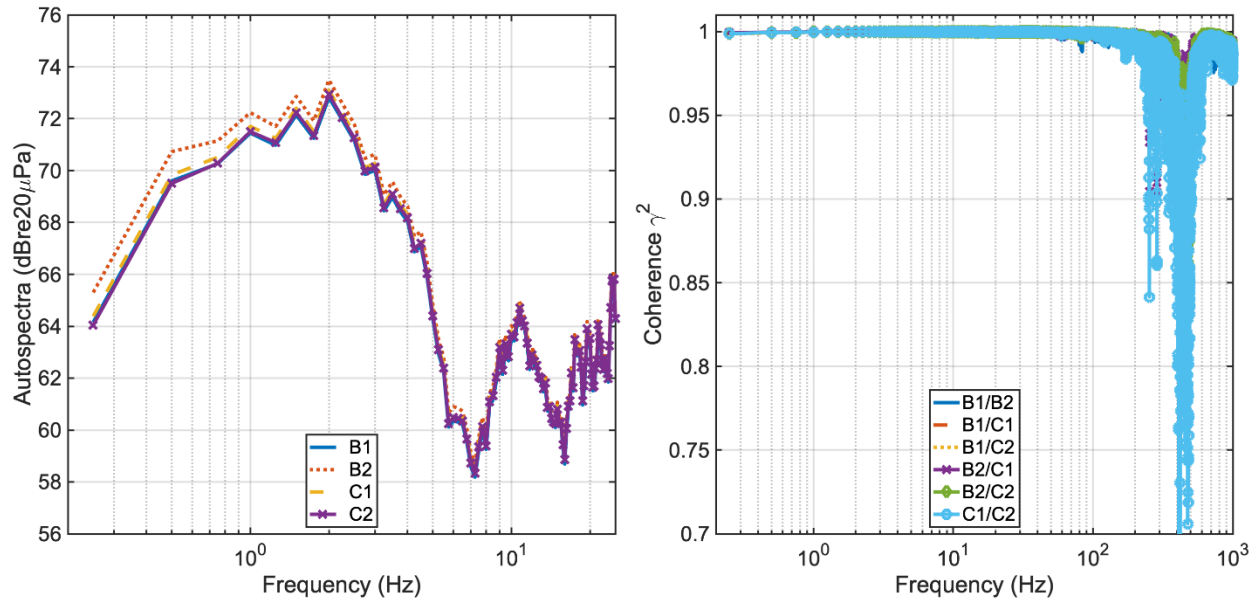
Figure 3.3.1 Burner with GRAS 46AE and 0.25-meter probe. Left: Autospectra for GRAS 46AE. Right: Coherence between GRAS 46AE pairs

Intensity direction calculations for the GRAS 46AE microphones in the 0.25 m spacing probe are shown in Figure 3.3.2.
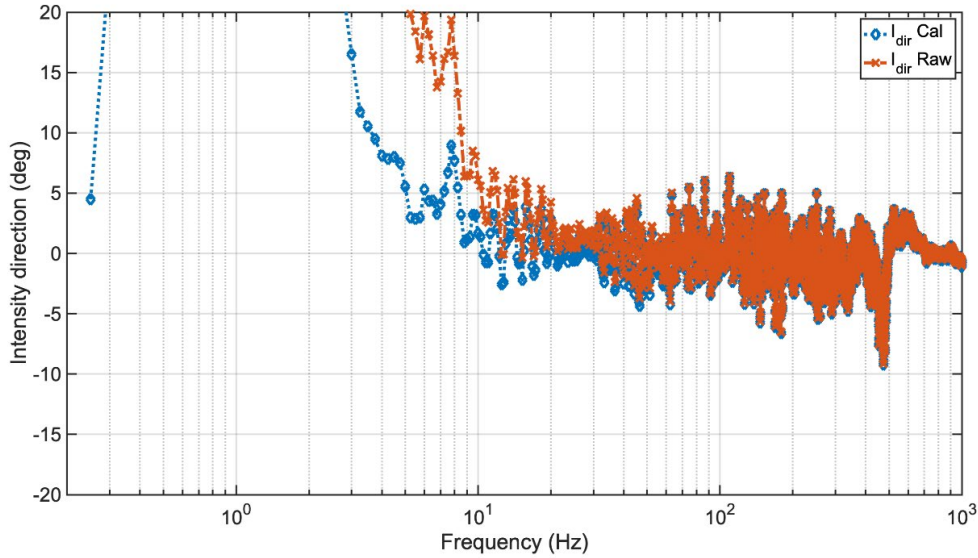
Figure 3.3.2 Intensity calculations for Burner with GRAS 46AE and 0.25 m probe

In this case, the intensity direction estimation has a more significant error compared with 47AC between 0.5 to 5 Hz. This fact is associated with a higher frequency roll-off. The GRAS 46AE microphones have a higher instrument mismatch below 3 Hz. The convergence to the ±5˚ tolerance does not happen until 5 Hz (except for a noise peak at 7.8 Hz). The 46AE results show the necessity of having a larger probe spacing for these microphones to increase the acoustic phase over the instrument mismatch ratio.

Intensity magnitude plots and comparison to autospectra are shown in Figure 3.3.3.
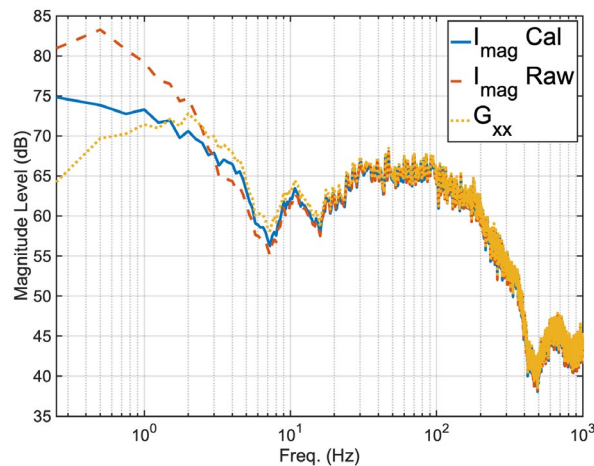
Figure 3.3.3 GRAS 46AE Intensity magnitude results and comparation to autospectra level

67

The intensity magnitude in Figure 3.3.3 shows the correction effect, although it is still overestimating up to 1.5 Hz and then underestimates until ~10 Hz.

The raw data overestimate the spectral level until 3 Hz. These errors are also related with microphone response and near field effects. The raw data magnitude error plot looks similar to GRAS 47AC raw data plot. Although in this case, since the acoustic phase is lower (since a small probe), the correction improves more significantly than for GRAS 47AC. Also, the microphone mismatch is higher; therefore, the correction is more effective for GRAS 46AE.

3.4 Conclusion and comparison between microphones and probes

Figure 3.2.3 and Figure 3.3.2 show the error reduction given by applying the mismatch correction found in this research. Intensity direction calculation shown lower error compared to the original data.

The magnitude correction has no apparent effect for GRAS 47AC microphones because those microphones are mounted in a larger probe and have a better response for low frequencies. On the contrary, GRAS 46AE microphones have an apparent magnitude correction effect below 5 Hz. This is because the reduced microphone spacing has some extra impact on this low-limit frequency response and weak microphone response for ultra-low frequency.

Figure 3.4.1 shows a comparison in the level measured with the two microphone sets. It is clear that for extremely low frequency (below 1.5 Hz), GRAS 47AC is 5 dB higher than levels for GRAS 46AE microphones. This result is due to the lower GRAS 47AC frequency cut-off. GRAS 47AC has a frequency cut-off of 0.1 Hz for 2 dB down criteria, and the 46AE set has a frequency

cut-off of ~3 Hz for the 2 dB down. Also, the microphones' response below its frequency cut-off usually exhibits a 90° shift becoming a measurement error source.
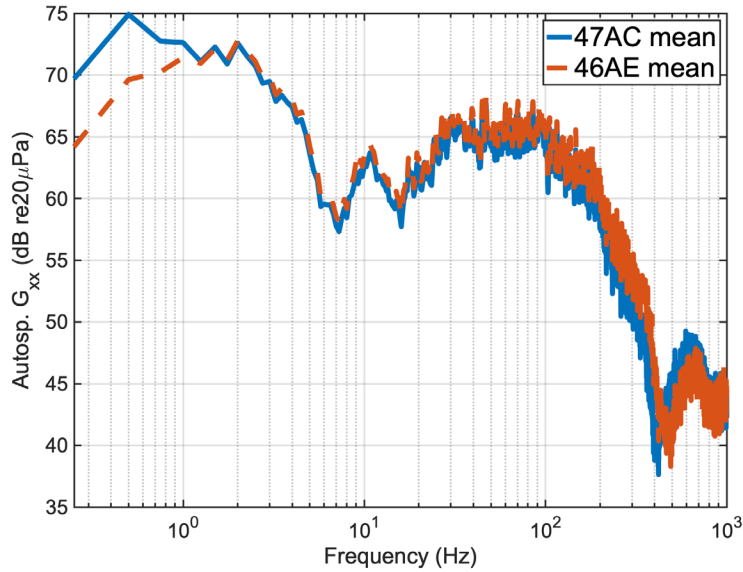
Figure 3.4.1 Autospectra comparison for two microphone sets. Solid and blue line represents GRAS 47AC, dashed and orange GRAS 46AE.

The error effect on the intensity calculations can also be observed in Figure 3.4.2, where the transfer function phase has been compared for the two sets. Besides the better low-frequency response, GRAS 47AC has a larger probe spacing demonstrated by the phase curve below 2 Hz. In this case, GRAS 46AE shows a larger phase below 2 Hz even though they were placed closer than the spacing for 47AC. This distance reduction should make 46AE phase measurement lower than 47AC. Since the microphone response for 46AE is not accurate below 2 Hz, the phase measurement is higher when it is expected to be lower.

The source of error is coming from the distance and from the microphone response although in this case the microphone response has a higher contribution. GRAS 46AE is not sensing the acoustic phase as GRAS 47AC is doing. Figure 3.4.2 show GRAS 46AE is measuring primarily instrument mismatch up to 5 Hz.

69
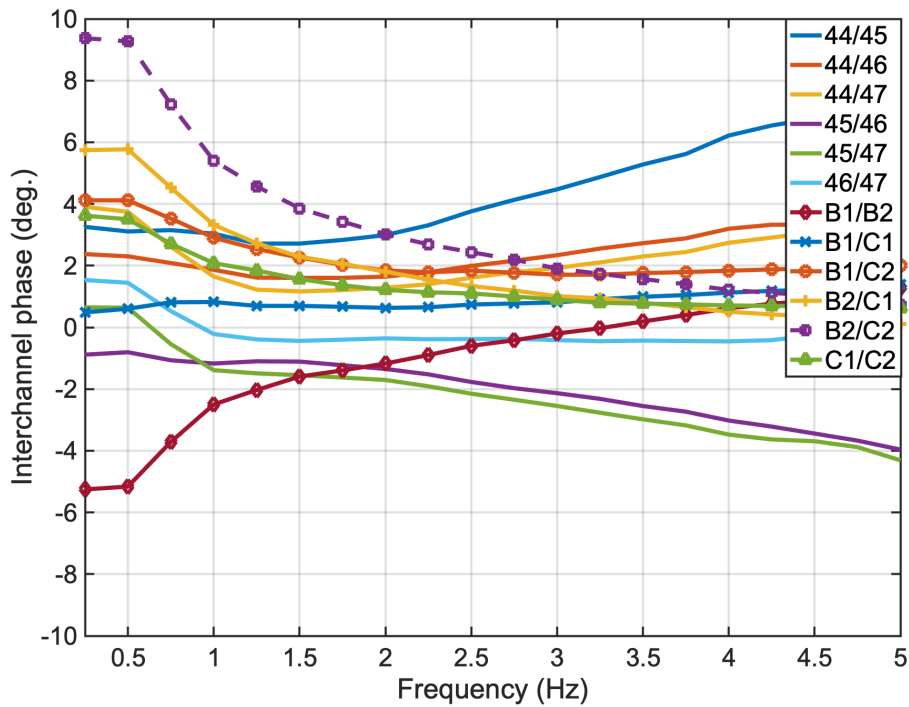
Figure 3.4.2 Channels transfer function phase comparison for two microphone sets. All solid lines are GRAS 47AC pairs and marked lines are GRAS 46AE pairs.

Even when a perfect coherence and a high signal-to-noise ratio, there are still errors in intensity calculations for the lower frequencies. The acoustic phase to instrument mismatch ratio is causing errors and making a lower limit for accurate calculations. The GRAS 47AC microphones and 0.5-meter probe radius showed intensity direction within ±3˚ range below 1 Hz, and for GRAS 46AE and 0.25-meter probe radius, the direction results are within the range for 5 Hz and above.

Contrary to the reference article by M. Pawlaczyk-Luszczynska[23], the current measurements went beyond the near-field intensity direction limits proposed. The reference concluded the distance from an infrasonic spheric wave source is ten times the wavelength, and in this case, we measured closer with lower errors.

70

4 Chapter 4: Acoustic intensity analysis of large rocket motor noise using the infrasonic correction

4.1 Overview

Major challenges measuring acoustic intensity from infrasonic sources are instrument mismatch and signal coherence. Chapter 2 described the determination of the phase and amplitude correction of 12.7 mm diameter, Type-1 microphones for three frequency ranges, including the infrasound region. This Chapter shows another way to address the measurement challenge. By modifying the interchannel spacing considered for the probe, the acoustic phase difference becomes greater than the mismatch for a broader range of frequencies, improving accuracy.

As the microphone spacing increases, the acoustic phase of a plane wave also increases for a given wavelength. As an example, consider a 1 Hz plane wave and one probe with 1 m microphone spacing and another with 10 m. The acoustic phase for a distance "d" of 1 m is ~1.05˚, and for 10 m spacing the acoustic phase is ~10.5˚. If the inter-channel mismatch is determined to be 0.4˚ for 1 Hz, the error level for intensity calculation is 13.4 dB for 1 m spacing and 4.78 dB for 10 m microphone spacing. This simple exercise shows the error reduction just by taking a larger distance between microphones.

In this chapter, rockets measurements made with two set of microphones (GRAS 46AE & GRAS 47AC) are analyzed to show the effect of larger inter-channel separation distance. Previous measurements were shown in Chapter 3 where the GRAS 47AC had improved intensity directions results by using a larger probe.

The effects of wind noise and terrain scatter were the significant challenges for rocket motors' outdoor intensity measurements. Therefore, this chapter is divided into 3 sections:

- Reduced probe spacing with standard windscreen

- Large probe spacing with enhanced wind screen

Table 4.1-1 shows a summary of chapter measurements. Finally, the chapter conclusions are included.

	April 4th GEM63		September 2nd Artemis FSB-1	
	46AE	47AC	46AE	47AC
Probe radius and type	0.25 m orthogonal	0.5 m orthogonal	5 m triangle	5 m triangle
Wind screen	90 mm diameter ball	90 mm diameter ball	38.1 mm thick dome	38.1 mm thick dome

Table 4.1-1 Chapter measurements summary

4.2 Rocket measurements for reduced probe spacing with standard wind screen

4.2.1 Experimental setup

This rocket test was conducted during a horizontal static firing of a large solid-fuel rocket motor and took place at the Northrop Grumman facilities in Promontory, Utah on the afternoon of 4 April 2019. The motor is a GEM 63 solid-fuel booster with a graphite-epoxy casing type being developed for the Atlas V launch vehicle. It has 373,000 lbf of thrust with a burning time of 86 s.
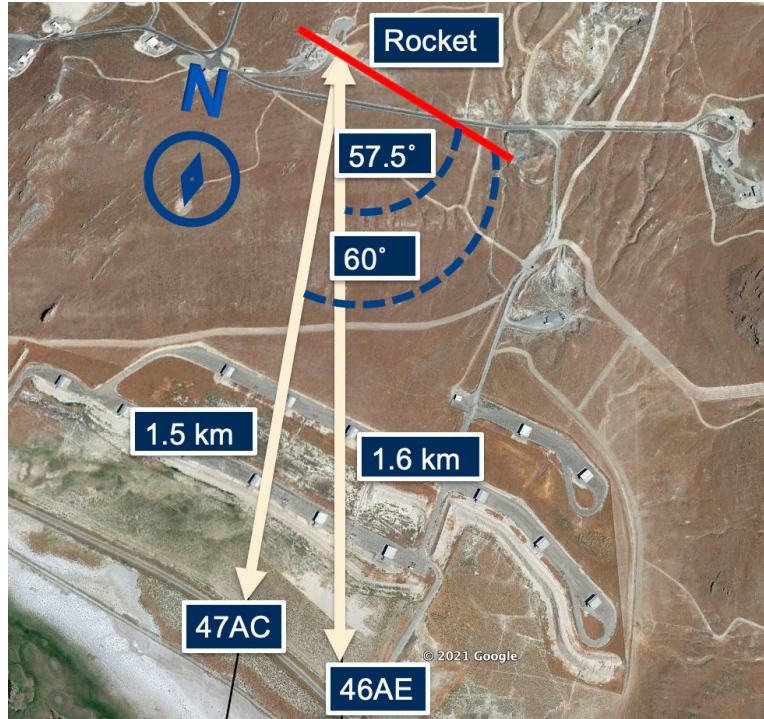
Figure 4.2.1 Experiment layout for GEM63 April 4th 2019, probe location for two microphone sets.

The probe location for both microphone sets are shown in Figure 4.2.1. The microphones were arranged as an orthogonal probe, as shown in Figure 4.2.2, and a 90 mm diameter ball windscreen covered each microphone. The probe was mounted on a tripod which height was 1.5 m off the ground. The microphones in each pair were separated by a distance of 0.5 m for GRAS 46AE and 1 m for GRAS 47AC, resulting in a one-dimensional (1D) spatial Nyquist frequency of ~340 Hz and ~170 Hz respectively.
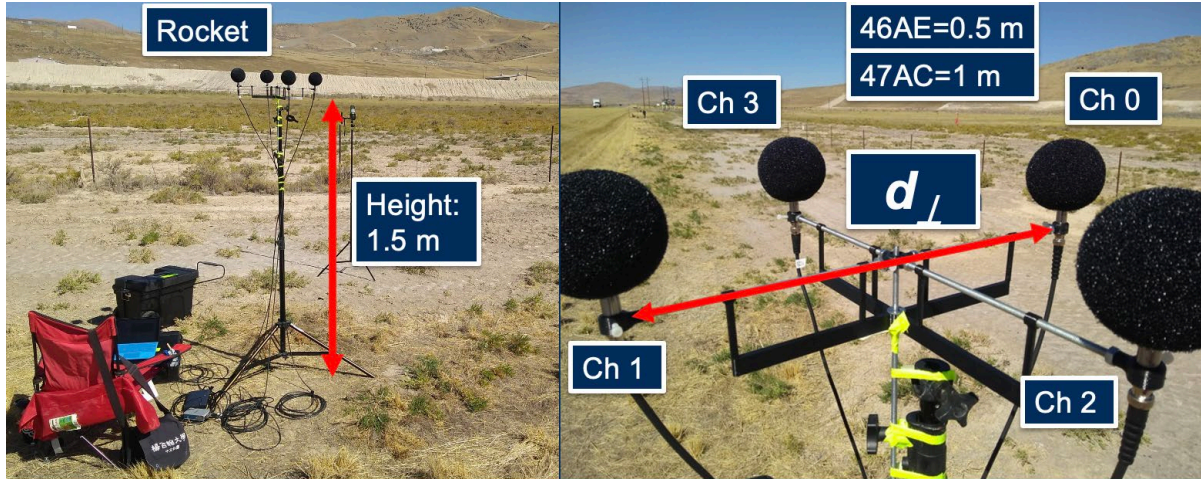
Figure 4.2.2 Orthogonal probe typical installation

The probe orientation was such that one microphone pair's axis pointed to/away from the source and the other pair was perpendicular. The probe's orientation was such that 0° corresponds to the expected sound intensity direction from the rocket. Although prior near-field intensity measurements of a similar GEM-60 rocket motor[38] described the extreme non-compactness and frequency dependence of the source, at this measurement distance, the source location can be separated into high frequency and low-frequency origin.

From NASA SP-8072[39] Figure 14, the noise generation can be distributed along with the exhaust flow related to its Strouhal number. The rocket core exhaust diameter can be approximately 1.47 m, and the jet velocity is approximately 2,500 m/s. With those data the Strouhal number for 1 Hz is roughly 0.001, and for 1kHz is 0.5.
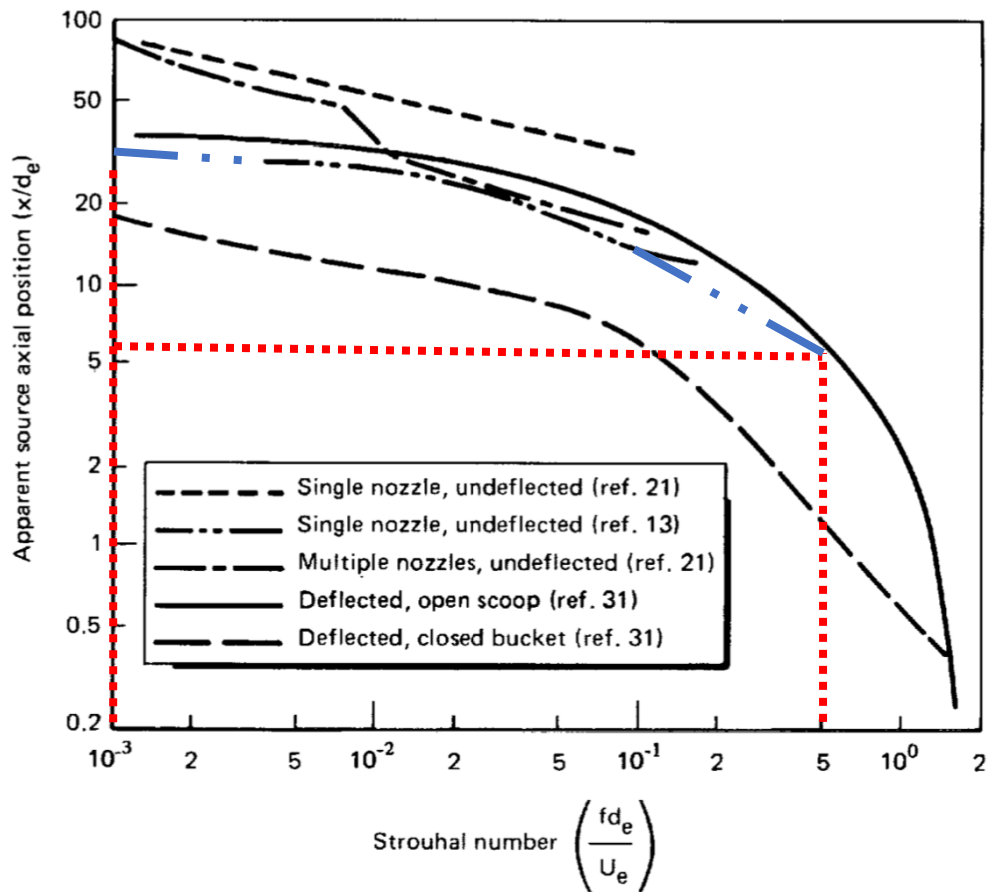
Figure 4.2.3 Axial location of apparent sources as a function of Strouhal number for chemical rockets.

A short analysis of this figure shows that the location difference between 1 Hz and 1 kHz is 30 diameters following the ref. 13 extrapolated line, as is shown in Figure 4.2.3. Dotted red lines mark the intersection for the selected frequencies. Assuming there is no interference between the plume and the microphones, the source location differs 30 nozzle diameters between 1 Hz and 1 kHz. The geometric relation between the probe and the rocket for the 30 diameters shift would show a change in intensity direction ranging between 3°-6°, depending on the measuring station location.

4.2.1.1 GRAS 46AE probe location

The probe was located 1.6 km away from the source, at 57.5 degrees relative to the nozzle centerline, as is shown in Figure 4.2.1; check reference[24] document for more details. The environment included propellant storage buildings and terrain variation; this is believed to affect the sound propagation and the measured results. Microphone B1 was at the North corner labeled as channel 0, B2 was at the south labeled as channel 1, C1 was at the East labeled as channel 2, and C2 was at the West side labeled as channel 3.

4.2.1.2 GRAS 47AC probe location

The probe was located at 60˚ angle relative to the nozzle centerline as shown in Figure 4.2.1. This location was close to the GRAS 46AE having similar energy content and acoustical field characteristics. The probe configuration for GRAS 47AC has the microphone SN44 at the northwest, SN45 at the northeast, SN46 at southwest and SN47 at southeast. The axis orientation was set to be align with the source, so the expected sound intensity direction is 0˚ as it was oriented for the GRAS 46AE probe.

4.2.2 Measurement analysis for GRAS 46AE

The autospectra and coherence are shown in Figure 4.2.4. In this measurement, the test location's wind condition generated a high noise in the lower infrasound region. Therefore, the coherence drop, starting at around 3 Hz and below, is expected to be related with wind noise.

76

Figure 4.2.4 Autospectra and coherence for GEM63 Apr. 4 rocket test with GRAS 46AE and 0.25-meter probe. Frequency resolution for this plot is 0.25 Hz.

The autospectra level shows disagreement below 2 Hz, which is associated with the microphone response (below cutoff frequency) and random error produced by the wind noise. Above 40 Hz, there is also disagreement between the levels measured, but the mismatch is produced by the turbulence created between the path arrivals.

The intensity direction is shown Figure 4.2.5. The calculations made with the original data are labeled as "raw" meaning there are no correction applied and the calculations made with the calibration are labeled as "Cal".

77
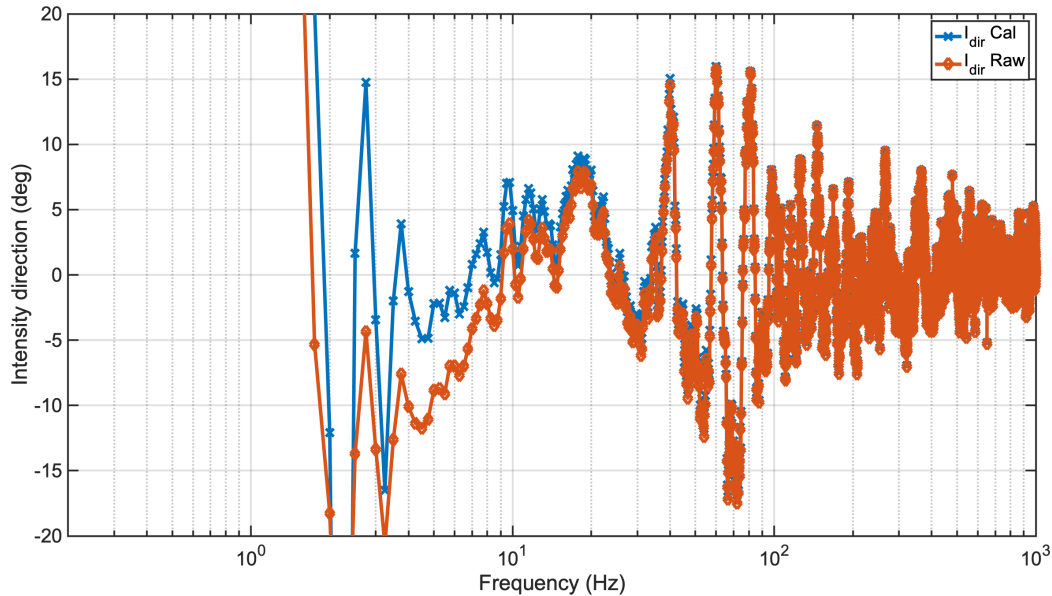
Figure 4.2.5 Intensity calculations for GEM63 April 4th, 2019 with GRAS 46AE and 0.25-meter radius probe. "x" marked line is the results with the calibration applied.

The intensity direction shows a high error below 3 Hz, assumed to be due to low coherence as was explained before. From 3 Hz and up to 20 Hz a drift in the direction can be observed having a bottom value of -20˚ and a top value +8˚ having a span of 30˚ which is considered to be excessive for source localization. Beginning around 20 Hz a ringing behavior is observed which is believed to be related with the field response having harmonics at 40, 60 and 80 Hz. The calibration shows an error reduction from 3 Hz and above.

Another point to highlight in this plot is the large jump around 2 Hz, which matches with the 2 Hz peak observed in Figure 4.2.6. This peak and direction may be associated with extraneous noise due to resonance generated in the terrain and/or buildings.

The intensity magnitude is show in Figure 4.2.6. The dotted line is the autospectrum, averaged across microphones, plotted for reference.

78
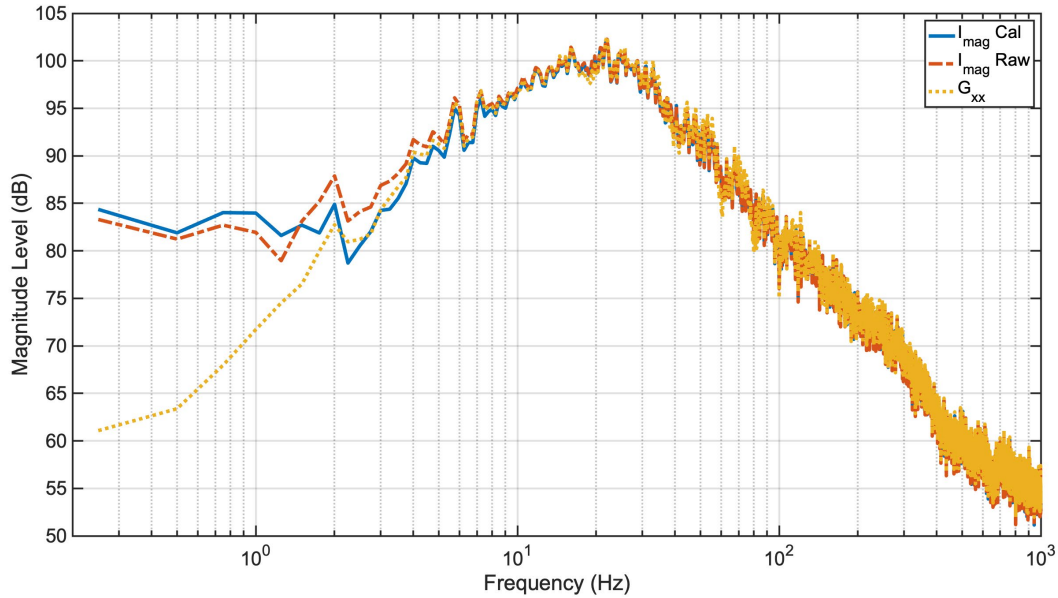
Figure 4.2.6 Intensity magnitude for GEM 63, April 4th 2019 with GRAS 46AE and 0.25-meter radius probe. Intensity magnitude relative to 1x10^{-12} W. Autospectra level is relative to 20x10^{-6} Pa

The comparison between autospectra and intensity magnitude shows large errors below 3 Hz, which is attributed to the low coherence. The calibration correction shows improvement from 1.5 Hz and up to 9 Hz matching the autospectra within ±0.5 dB from 2.5 Hz.

4.2.3 Measurement analysis for GRAS 47AC

Autospectra and coherence are shown in Figure 4.2.7. The frequency resolution is 0.25 Hz. The peak energy is centered at 20 Hz. The peak at 2 Hz is also visible in these measurements. The coherence starts to fall at 3 Hz and at 1 Hz is under 0.5, which suggests the presence of wind noise at this location.
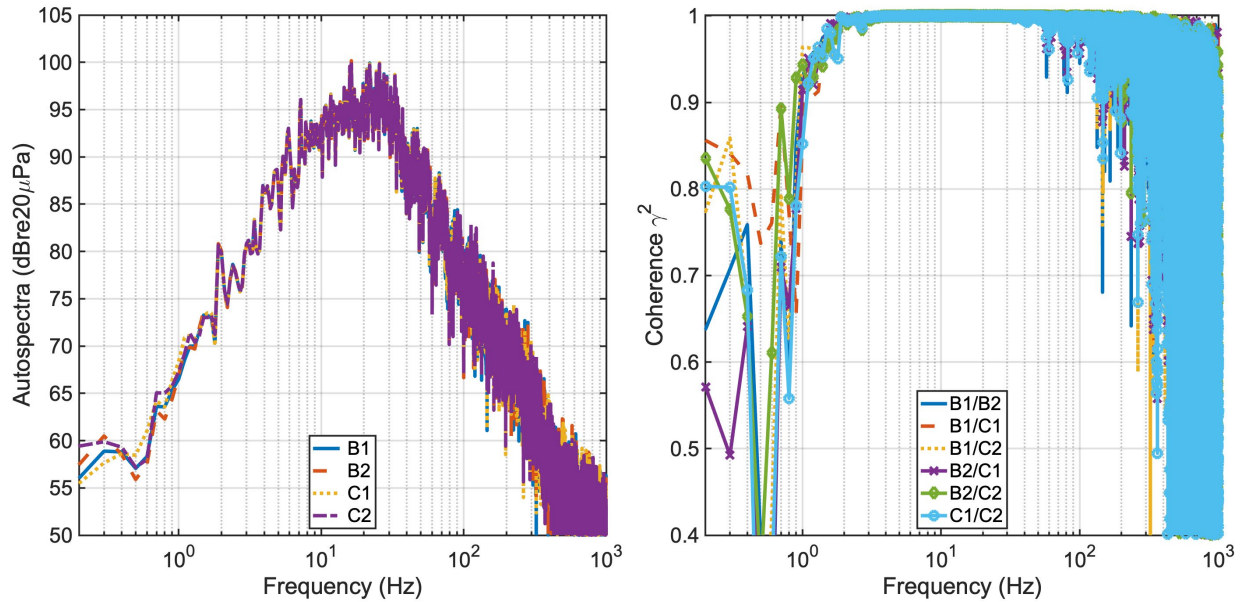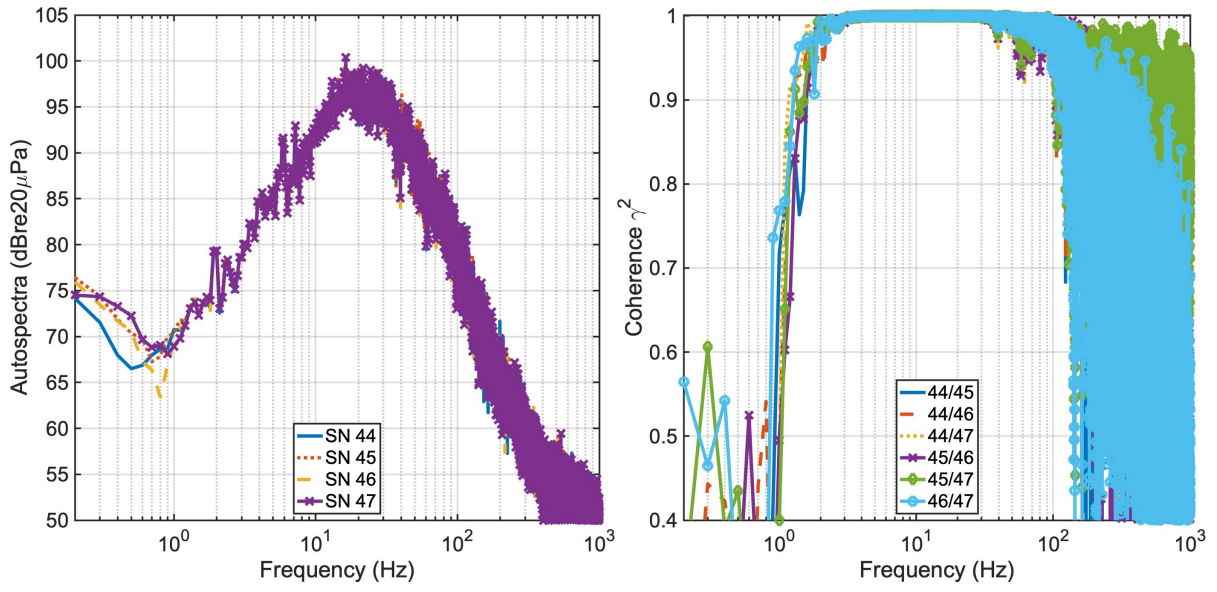
Figure 4.2.7 Autospectra and coherence for GEM63 Apr. 4th, 2019 rocket test with GRAS 47AC and 0.5 m radius probe. Frequency resolution for this plot is 0.25 Hz

Intensity calculation is shown in Figure 4.2.8 for direction and magnitude.
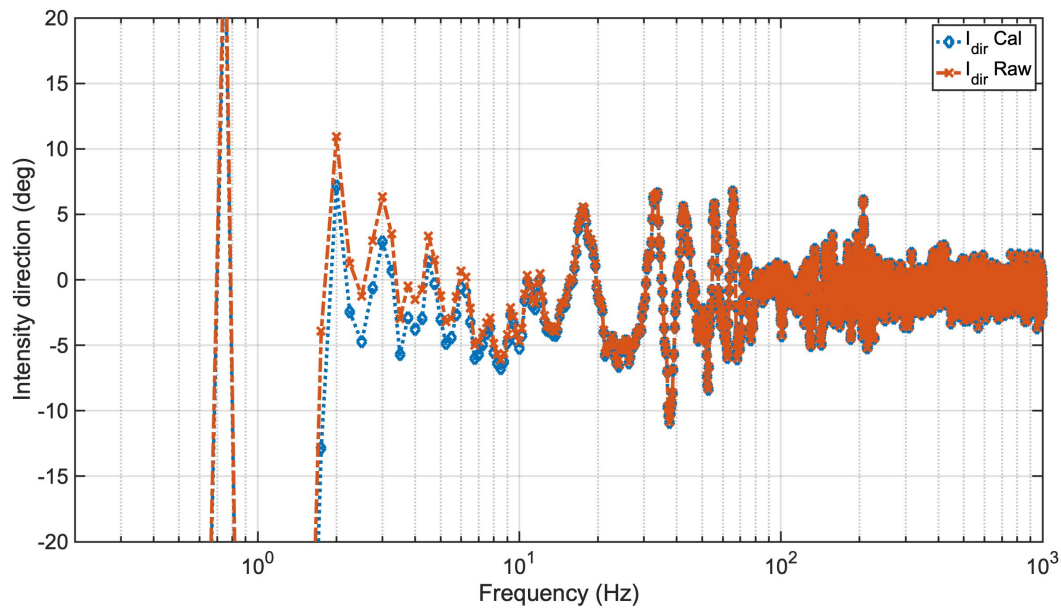
Figure 4.2.8 Intensity direction for GEM63 April 4 with GRAS 47AC and 0.5 m radius probe. Frequency resolution is 0.25 Hz

This set of microphone shows less drift and a much narrow span with ±5° for intensity direction. The intensity magnitude is compared to the autospectra level (considering a propagating plane wave) and is overestimated until 3 Hz, as is shown in Figure 4.2.9. Also, the direction

80

calculations start to narrow at 3 Hz. This means that the calculations improve from this point due mainly to the probe inter-channel distance.

It can be noticed the improvement on calculations for this probe, this improvement is related with the lower microphone mismatch and most likely for the microphone spacing (double).
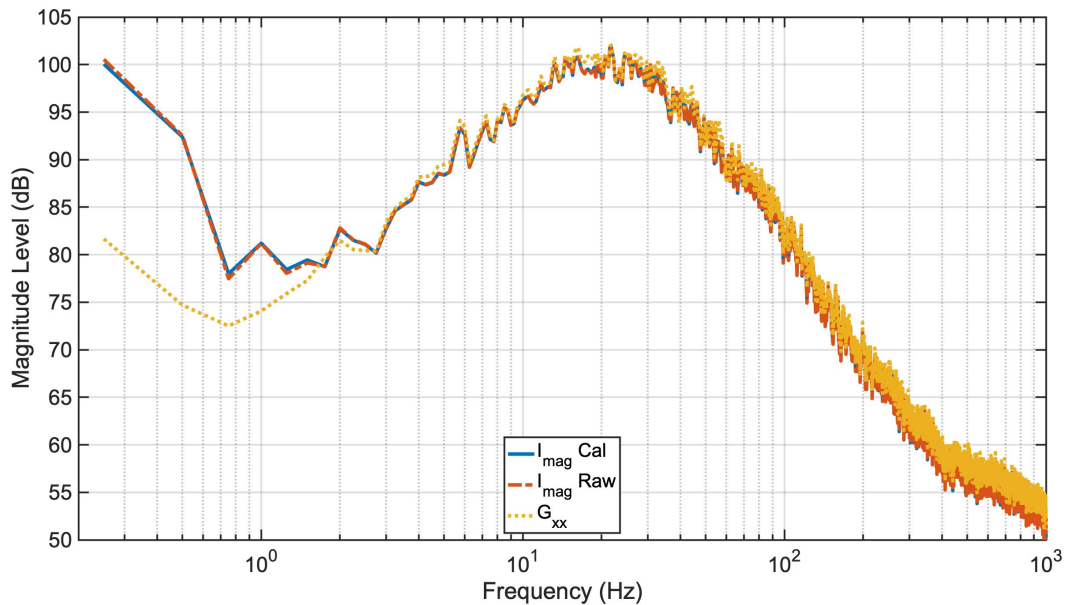
Figure 4.2.9 Intensity magnitude for GEM63 April 4th with GRAS 47AC and 0.5 m radius probe.

4.3 Rocket Measurements with large microphone spacing probe and GRAS 46AE

4.3.1 Experimental setup

The rocket test was a static horizontal firing of the FSB-1 booster, which has a maximum of 1,800,000 lbs of thrust. This booster is part of the Artemis NASA mission. The FSB-1 motor is 46.9 meters in length and a nozzle with a 3.88 meters exit diameter. The test is near 120 s of firing time.

The equilateral triangular probe uses four microphones, as is shown in Figure 4.3.1, one at the center and one at each vertex. The 'x' axis of the probe for this particular test was deviated by approximately 21˚ from the source's direct line. The circle circumscribed by the probe equilateral has a radius of 5 m.
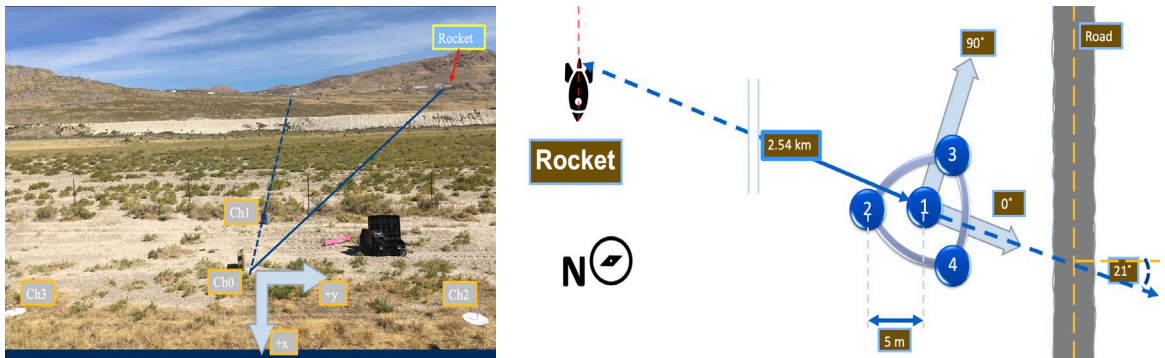
Figure 4.3.1 Equilateral triangle probe layout, generic setup for 5 m spacing probe installation. For this test the "x" axis was deviated by -21˚. Left side: Picture of the installation. Right side: Probe location sketch

The GRAS 46AE was located at an angle of 105˚ while GRAS 47AC at 115˚ relative to the nozzle centerline. Figure 4.3.2 shows the experiment sketch. The levels expected at this location are lower than the other rocket test conducted in previous subsections. The microphones were placed on a reflective board and surrounded with a thick windscreen as was described in Section 2.3.3 in Chapter 2.
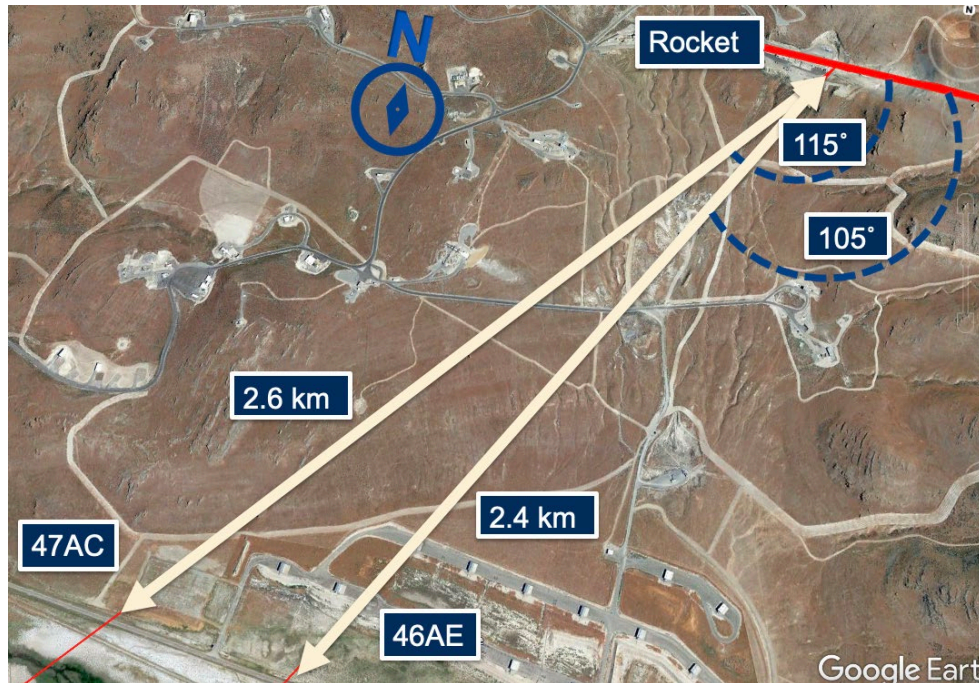
Figure 4.3.2 Large spacing probe location for the Artemis booster rocket static test using 5 m triangle.

4.3.2 Measurement analysis for GRAS 46AE

The autospectra have a maximum at 4-5 Hz, as is shown in Figure 4.3.3. This peak is present at a much lower frequency value than the previous rocket at 20-25 Hz. The rocket motor diameter is larger than GEM63, therefore the lower frequency value for the autospectra peak. The curve below 1 Hz shows a roll-off and better agreement between the four channels compared to previous GEM63 test. The frequency resolution for these plots is 0.1 Hz due to the more extended recording available.

Note in Figure 4.3.3, the coherence is much higher compared to the previous section's results; this means the signal was not contaminated. The drop starts at 1 Hz approximately although the values remain high below that point. The explanation is the weather since lower wind speed

generates lower wind noise. Besides, because of the rocket motor characteristics, the peak of energy is at a lower frequency range compared to the GEM63 rocket.
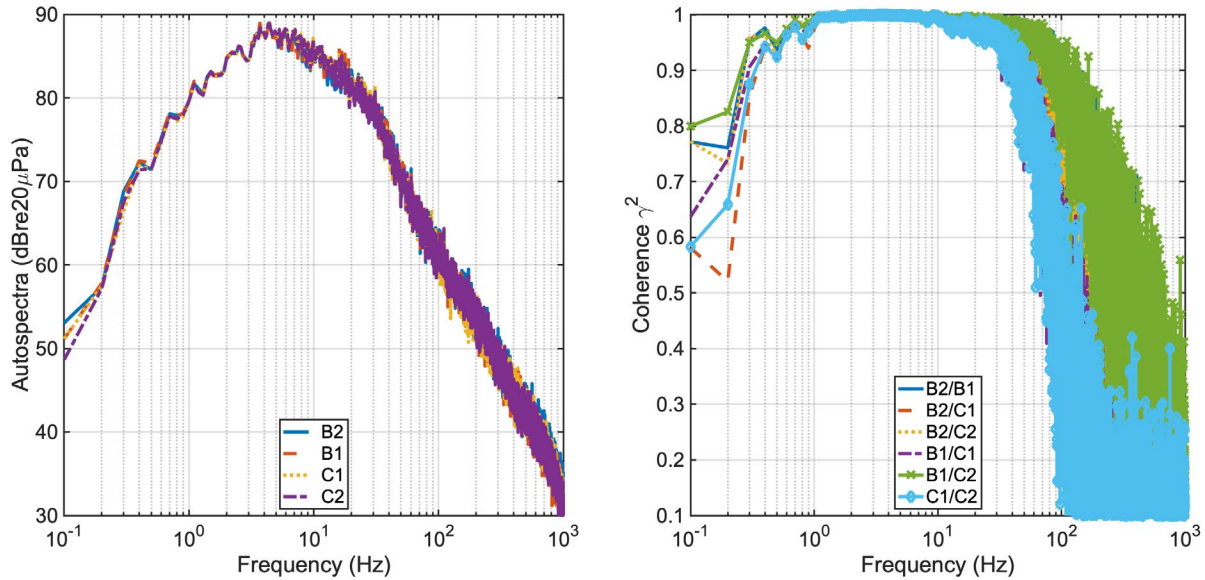
Figure 4.3.3 Autospectra and coherence with the GRAS 46AE and triangle probe. Frequency resolution is 0.1 Hz

Even though the experimental setup differs for each rocket, this analysis compares the match between intensity direction and probe orientation and the similarity of the autospectra level and intensity magnitude at each location. Figure 4.3.4 shows the intensity calculations. In this case, a frequency resolution of 0.25 Hz is used to make the plots match the last rocket measurement criteria.

The error reduction in the intensity direction is not so evident in this case. The calibration improves the results, but the correction amount is not as much as it was for the smaller probe. The acoustic phase increase due to the microphone spacing explains this by increasing the ratio between acoustic phase and instrument mismatch.
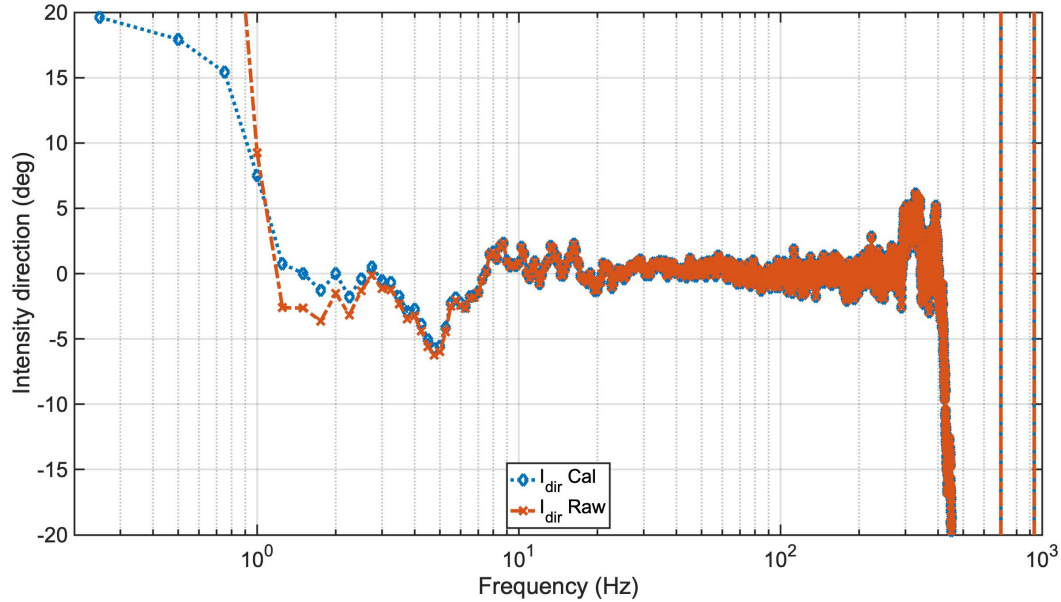
Figure 4.3.4 Intensity direction comparison between calibration and original data for Artemis rocket test using GRAS 46AE and triangle probe. Plots made with 0.25 Hz frequency resolution.

The variation shown in these intensity direction results is also present as it was for GEM63 rocket tests. Noise and random scatter present at test field affect the intensity direction, with variations of ±3° above 8 Hz, and less than ±5° between 1-8 Hz range. Also, above 400 Hz, the intensity direction becomes random. The low autospectra levels cause this error surge for frequencies over 400 Hz, reaching the acquisition system floor noise. Coherence has a steep roll-off starting at 100 Hz; therefore, the signal at higher frequencies is contaminated or just random. This limitation is part of the trade-off between the instrument separation distance and coherence.

The drift and ringing do not affect the results so hard compared to the small spacing probe. The difference between the calibrated direction and the raw data is higher in this case, having +8° for 1 Hz and more than 30° below 0.75 Hz. Besides, for the 1.5-6 Hz range, the intensity direction converges to -2° approximately, which is in agreement with the experiment setup. The direction trend difference between the 1.5-6 Hz range and higher frequencies is about 2° to 3°. It is related

85

to the source location characteristics, which are not compact, having a difference of 30 nozzle diameters between the lowest and highest frequencies, as is shown in Figure 4.2.3.
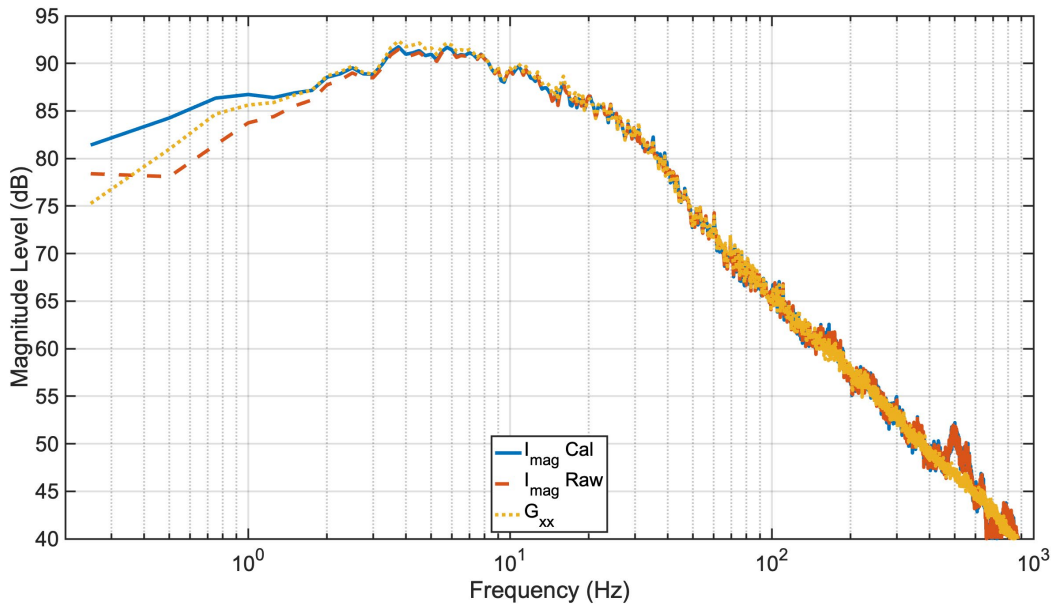
Figure 4.3.5 Intensity magnitude comparison with correction, original data and autospectra for Artemis rocket test using GRAS 46AE and triangle probe. Plots made with 0.25 Hz frequency resolution.

The acoustic intensity magnitude is underestimated below 2.5 Hz and shows disagreement with the raw data level until it reaches 0.5 Hz. The magnitude error is related to the instrument mismatch below 3 Hz. The probe spacing of 5 m reduces the error below the limit shown for 0.25 m spacing, having an intensity calculation improvement from 18 Hz to 3 Hz. The difference between calibrated data and raw data shows a small disagreement until ~3 Hz, where the instrument mismatch becomes small relative to the acoustic phase obtained with the 5 m spacing.

4.3.3 Measurement analysis for GRAS 47AC

The autospectra show a maximum of 88.5 dB at 4-5 Hz, as is shown in Figure 4.3.6. The microphone with serial number ending in 47 had a faulty cable; therefore, it will not be included in this section. The frequency resolution for autospectra and coherence plots is 0.1 Hz.
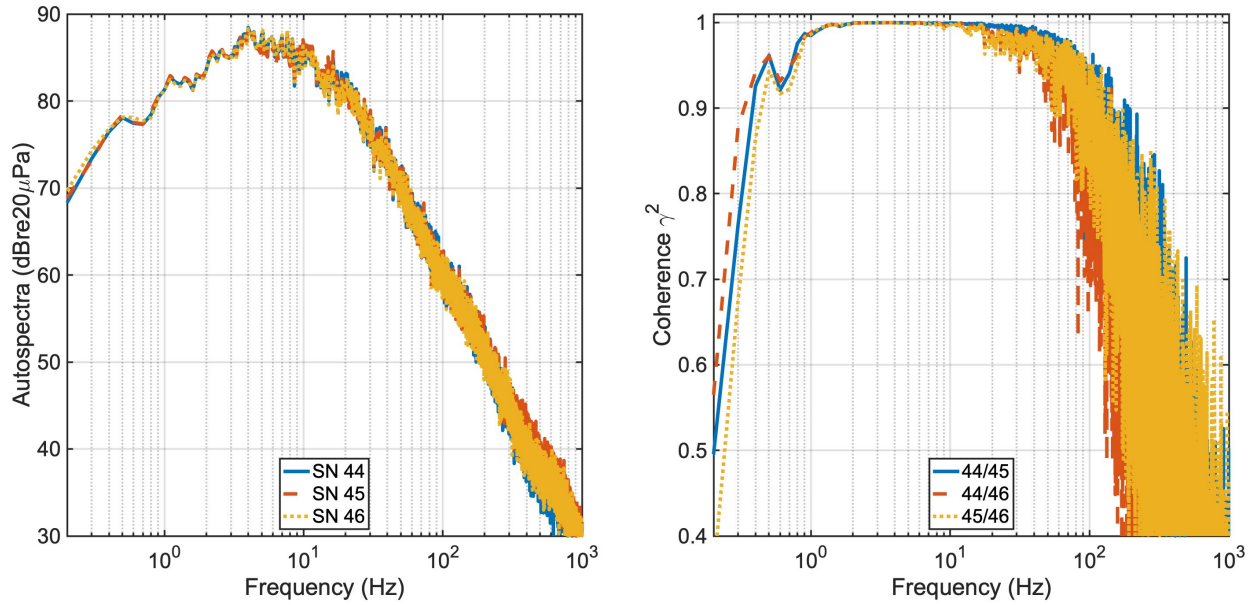
Figure 4.3.6 Autospectra and coherence with the GRAS 47AC and 5-meter probe. Frequency resolution of 0.1 Hz

The coherence is high from 1 Hz and up to 100 Hz, as is shown in Figure 4.3.6. The high coherence for low frequencies is explained by the lower wind noise and thicker windscreen. Above 100 Hz, coherence and autospectra show a steep roll-off. Because of the coherence drop, the upper limit for intensity calculations using this probe is 800 Hz, as shown in Figure 4.3.7.

Figure 4.3.7 shows the intensity calculations. In this case, a frequency resolution of 0.25 Hz matches the last rocket measurement plots.
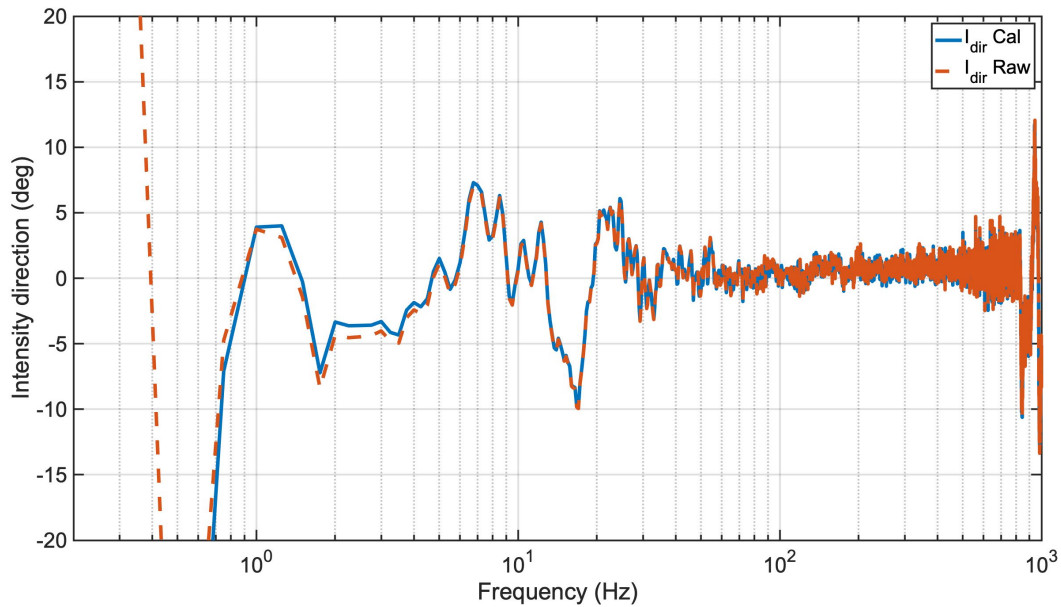
Figure 4.3.7 Intensity direction for larger spacing probe using GRAS 47AC. Plots made with 0.25 Hz frequency resolution. Raw and calibrated data show a small difference between 0.5 and 6 Hz.

As before, the intensity direction difference between calibrated and original data is not so evident for the 47AC microphones. The correction has improved compared to the small spacing probe because the lower variation below 2 Hz, intensity direction values are within ±5° from a lower frequency range. This is explained by the acoustic phase increase due to the microphone spacing, which increases the ratio between instrument mismatch and acoustic phase.

The results for intensity direction still show more significant variation for frequencies below 1 Hz. Wind noise below 1 Hz combined with test field noise makes the intensity direction contaminated at lower frequencies, showing different intensity direction values at 17 Hz and random values below 0.8 Hz.

The calibrated intensity magnitude is in agreement with the autospectra for the entire frequency range. The original data matches the autospectra from 0.7 Hz and above, as shown in Figure 4.3.8.
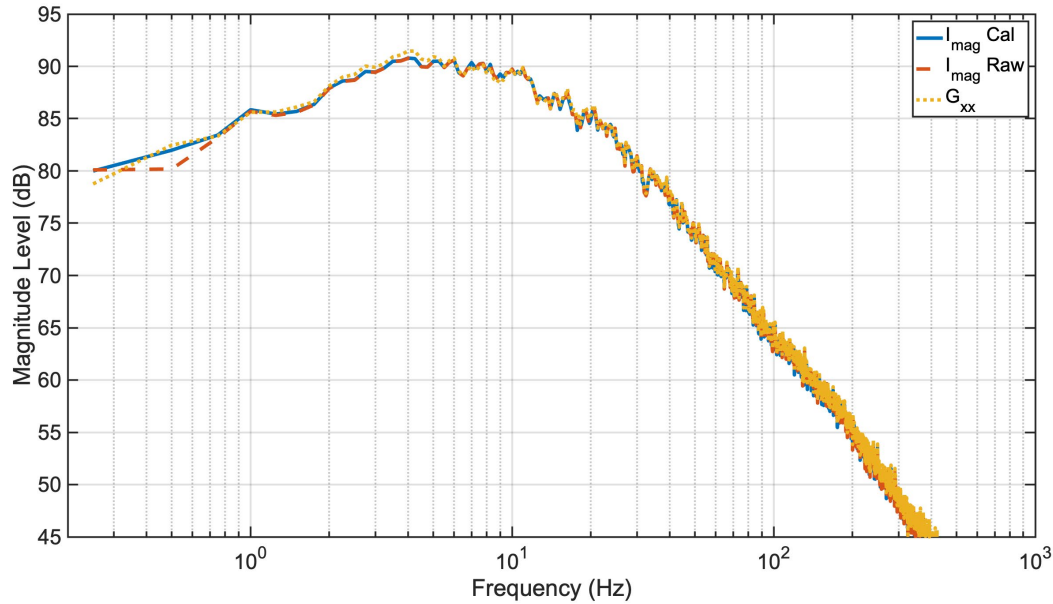
Figure 4.3.8 Intensity magnitude comparison with correction, original data and autospectra

The probe spacing of 5 m reduces the error for intensity calculations compared to the 0.25 m spacing probe. The difference between calibrated and raw data shows a small disagreement because the instrument mismatch becomes small for the acoustic phase obtained with 5 m spacing.

4.4 Rocket analysis conclusions

This chapter has shown the intensity measurements extension to lower frequencies by the calibration application and increased microphone spacing. The nature of the acoustic far-field from a static rocket test showed limitations for intensity measurement verification. The presence of contaminating noise from buildings and terrain scatters, and wind generates uncertainty on the intensity estimations. Resonance and ringing tendency showed deviation from the expected intensity direction, while intensity magnitude errors due to wind noise (below 1 Hz) are present for the lower frequency band.

Increased microphone spacing probes showed a considerable improvement in the acoustic intensity. The intensity direction for the larger probe spacing showed a lower direction variation for GRAS 46AE and GRAS 47AC microphones. However, a remark should be made on the source location drift between lower and higher frequencies explained in Figure 4.2.3. Particularly for GRAS 46AE, the results are within ±5˚ from 1 Hz, having an improvement from 18 Hz observed for the small spacing probe.

The low frequency increased coherence observed in larger probes is explained by meteorological conditions (lower noise level) and the ability to filter wind noise using a thicker windscreen and place the microphones on the ground level. The improvement in low-frequency coherence generates improvement in the intensity magnitude calculations. The autospectra matched the intensity magnitude at 6 Hz for the small probe and the larger probe at 3 Hz. From these results, the recommendation for the GRAS 46AE using a 0.25 m probe is the calibration would not correct below 6 Hz. Whereas the GRAS 47AC with a 1-meter probe, the calibration would not go under 2 Hz.

The main challenge showed for outdoor rocket intensity measurements was wind noise, and other randomness assumed at this point from field scatters. Larger microphone spacing improves the measurements, although it showed an upper limit for the two microphone sets; therefore, the recommendation includes analyzing windscreen capability, microphone spacing versus high-frequency limit, distance to the source, and path interference with the terrain.

5 Chapter 5: Conclusions and Recommendations

5.1 Summary

The thesis shows intensity measurements down to the infrasound regime using the PAGE method for vector intensity. Application to two types of acoustic fields (from hot air balloon burner and rocket motors) shows the limitations of using different probe sizes in outdoor environments. A relative calibration using an infrasonic source generated inside a passenger car was used to find the instrument mismatch correction.

The relative calibration for the infrasound and low audio ranges consisted of applying the equal excitation principle to find the instrument mismatch. The infrasound levels measured at the car for relative calibration agreed with the preceding related scientific literature. On the other hand, the burner provided an alternative acoustic source to benchmark results into the infrasonic and low audio ranges (up to 50 Hz). Both infrasound sources were helpful for relative calibration, although the burner source showed lower levels than the car in the infrasound regime.

The relative calibration allows correction of the intensity measurements. The 5 m spacing probe and GRAS 47AC microphones allowed intensity direction within ±5° tolerance to go down to 1 Hz. For the GRAS 46AE microphones, intensity direction measurements were within the tolerance range down to 2 Hz for the same configuration probe. Intensity magnitude calculations were also improved down to 1.5 Hz for GRAS 46AE and down to 0.4 Hz for GRAS 47AC and 5 m spacing probe.

The correction effects are more significant when the acoustic phase is not significantly greater than the instrument mismatch, as shown in Section 4.3.3. If the acoustic phase is greater than the instrument mismatch by at least 10 times, the intensity direction correction does not

91

significantly change the original data. Figure 4.3.7 showed that the correction does not affect the intensity direction for a more extensive acoustic phase (5 m spacing probe). On the other hand, intensity magnitude calculations showed more change for larger probes than for smaller ones. Intensity measurements for all probes showed the correction becomes smaller for higher frequencies because the instrument mismatch is small for higher frequencies.

5.2 Contributions

This thesis describes a convenient approach to find the relative calibration between microphones for intensity measurements in the infrasound and low-audio regimes. Although infrasound inside vehicles has been studied before, its use for relative calibration under equal excitation has not been explored previously. This work is also unique in that conventional half-inch microphones are used into the infrasound regime. Additionally, sensor arrays used for this work were compact compared to state-of-the-art infrasonic arrays, while being much larger than typical intensity arrays. And, although larger spacing is used, the PAGE method allows the analysis extension to higher frequencies when sources are broadband through phase unwrapping. All these combinations constitute a significant contribution to infrasonic vector intensity measurements.

5.3 Recommendations

The thesis has consisted of microphone relative calibration and its application to intensity measurements into the infrasound regime. Recommendations are thus divided into relative calibration and intensity measurement considerations.

5.3.1 Relative Calibration

Relative calibration utilizing the infrasound field from a passenger car is a convenient method for instrument mismatch determination. According to the references, the levels of infrasound depend

on the vehicle's speed and size. The two passenger cars used in this research showed infrasound levels in the 65-95 dB range with a traveling speed between 35-70 MPH. For higher infrasound levels, large car size and highway speeds are recommended. Also, the microphones models showed different levels; therefore, a microphone with lower sensitivity and frequency cut-off would show higher infrasound levels. In this case, GRAS 47AC microphones with a frequency cut-off of 0.1 Hz and a sensitivity of 8 mV/Pa recorded higher infrasound levels than the GRAS 46AE, which have a frequency cut-off of 3.15 Hz and 50 mV/Pa sensitivity. The "pole-shifting" digital filtering technique developed by Gabrielson and recently applied to sonic boom analysis[40,37] might be used to improve the absolute low-frequency response of the 46AE. Combined with the relative calibration described here, conventional half-inch microphones, which cost appreciably less than their extended infrasound-range counterparts, can be calibrated down to 1-2 Hz.

5.3.2 Outdoor Intensity Measurement

In addition to instrument mismatch, the major challenges for outdoor infrasound intensity measurements were reductions in coherence due to turbulence: wind noise at low frequencies and partially randomized phases at high frequencies. Reflections/scattering from unknown low-frequency sources was also a challenge that could not be fully analyzed in this thesis. The 5 m spacing, ground-based probe equipped with a windscreen helped reduce wind noise and improve low-frequency estimates. However, the disadvantage with this probe was that it reduced the upper-frequency limit for accurate calculations, and required extensive area to place the microphones. Ultimately, achieving a fair accuracy for intensity measurements involves combining more extensive microphone spacing, lower frequency cut-off microphone, and robust wind screening (noise filtering) depending on the microphone availability and field conditions. All these elements showed an improvement in outdoor intensity measurements.

5.4 Future Work

Future work should focus on improving the infrasonic intensity measurement limitations found in the two outdoor sources. Errors are still present in the lower infrasound band, related to acoustic and instrument mismatch ratios. Also, outdoor environments like the rocket are affected by additional noise, becoming an excellent opportunity to further investigate the application of a coherent-based intensity method[41].

From the outdoor measurement point of view, current probes were two-dimensional only. Future research work could include outdoor three-dimensional probes. Optimizing windscreens for infrasonic intensity is an additional topic of research.

Another interesting scope for future work is developing an infrasonic intensity calibrator using a pistonphone or speakerphone designed for infrasound. This would help to apply a comprehensive relative and absolute microphone calibration.

REFERENCES

[1] Crocker and Jacobsen "Springer Handbook of acoustics, Encyclopedia of Acoustic Vol. 4 Ch 156," John Wiley Sons Inc., 1997

[2] F. Jacobsen, "Sound intensity," in Springer Handbook of acoustics, edited by T.D. Rossing (Springer, New York, 2007), pp. 961-1017.

[3] D. C. Thomas, B. Y. Christensen and K. L. Gee, "Phase and amplitude gradient method for the estimation of acoustic vector quantities," J. Acoust. Soc. Am. **137**, 3366-3376 (2015).

[4] K. L. Gee, T. B. Nielsen, S. D. Sommerfeldt, M. Akamine, K. Okamoto. "Experimental validation of acoustics intensity bandwidth extension by phase unwrapping." J. Acoust. Soc. Am. 141, EL357 (2017)

[5] F. J. Fahy, "Measurement of acoustic intensity using the cross-spectral density of two microphone signals," J. Acoust. Soc. Am. **62**, 1057 (1977).

[6] F.J. Fahy *Sound Intensity*, 2nd ed., E&FN Spon, London, 1995.

[7] F. Jacobsen and H. E. De Bree, "A comparison of two different sound intensity measurements principles," J. Acoust. Soc. Am. **118**, 1510-1517 (2015).

[8] W. F. Druyvesteyn and H. E. De Bree, "A novel sound intensity probe comparison with the pair of pressure microphones intensity probe," J. Audio Eng. Soc. **48**, 49-56 (2000).

[9] J. H. Giraud, K. L. Gee, and J. E. Ellsworth, "Acoustic temperature measurement in a rocket noise field," J. Acoust. Soc. Am.**127**, EL 179-EL 184 (2010).

[10] J. K. Thomson and D. R. Tree, "Finite-difference approximation errors in acoustics intensity measurements," J. Sound Vib. **75**, 229-238 (1981).

[11] E. B. Whiting, J. S. Lawrence, K. L. Gee, T. B. Neilsen and S. D. Sommerfeldt, "Bias errors analysis for phase and amplitude gradient estimation of acoustic intensity and specific acoustic impedance," J. Acoust. Soc. Am. **142**, 2208-2018 (2017).

[12] T. B. Gabrielson, "Infrasound" in Springer Handbook of acoustics, edited by M. J. Crocker (John Wiley & Sons, Inc., 1998), pp. 331-336.

[13] W. Tempest et al., "Infrasound and low frequency vibration," (Academic Press, 1976), pp. 1-35.

[14] J. Vanderkooy, "Infrasound in Vehicles—Theory, Measurement, and Analysis," Audio Engineering Society, Convention Paper 9049, (April 2014).

[15] Ulf Sandberg, "Combined effect of noise, infrasound and vibration on driver performance," Internoise, Procedings, Volume **2**, pp. 887-890, (July 1983).

[16] G. Nowacki, I. Mitraszewska, T. Kaminski, A. Wierzejski, "Research of infrasound noise in heavy goods vehicle and busses," The 8th International Conference "Reliability and Statistics in Transportation and Communication-2008", pp. 209-215 Riga Latvia, (October 2008).

[17] H. Spannheimer, R. Freymann, "Infrasound and Low Frequency Noise in the Passenger Compartment of Vehicles," Journal of Low Frequency Noise, Vibration and Active Control, **16**(4), pp. 219-227 (1997).

[18] C. L. Szuberla, J. V. Olson, "Uncertainties associated with parameter estimation in atmospheric infrasound arrays," J. Acoust. Soc. Am. **115**, 253 (2004).

[19] E. T. Herrin et al., "High-altitude infrasound calibration experiments," Acoustics today, April 2008.

[20] G. E. Greene, J. Howard, "Natural Infrasound," NOAA Technical report ERL 317-WPL 37, Boulder, Colorado March 1975.

[21] M. L. Barlett, T. G. Muir, C. M. Slack, M. F. Hamilton, "Acoustical characterization of a portable pneumatic infrasound source," J. Acoust. Soc. Am. **148**, 3818 (2020).

[22] D. Ming-rong, C. Ke-an, X. Xue-zhong, Z. Min, R. Hao-zhong, L. Xu-bin, and H. Bin, "Theoretical and experimental study of a prototype high-intensity infrasonic acoustic generator," Journal of low frequency noise, vibration and active control, Vol. **30,** No. 1, 2011, pp. 31-43.

[23] M. Pawlaczyk-Luszczynska, "Infrasound in the occupational and general environment: a three-element microphone measuring method for locating distant sources of infrasound," International Journal of Occupational Medicine and Environmental Health, Vol. **9**, No. 1, 1996, pp. 17-27.

[24] F. J. Irarrazabal, M. R. Cook, K. L. Gee, P. Nelson, D. J. Novakovich, and S. D. Sommerfeldt, "Initial Infrasound source characterization using the phase and amplitude gradient estimator method," Proc. Mtgs. Acoust., **36**, 045004 (2019).

[25] Ulf Sandberg, "Identification of infrasound generation mechanism in a bus," Journal of low frequency noise and vibration, **7**, No. 3, pp. 110-116 (1998).

[26] J. B. Westin, "Infrasound: a short review of effects on man," Aviation, Space, and Environmental Medicine, **46** (9), pp.1135-1140, (Sep 1975).

[27] T. W. Leishman, "Physics 660 Class Notes" Brigham Young University, Provo, 2019.

[28] G. Rasmussen, K. M. Nielson, "Technical Note low frequency calibration of measurement microphones," Journal of low frequency noise, vibration and active control, **28** (3), pp. 223-228 (2009).

[29] J. Y. Chung, D. A. Blaser, "Transfer function method of measuring in-duct acoustic properties. I. Theory," J. Acoust. Soc. Am. **68**, 907 (1980).

[30] C. M. Smith, T. B. Gabrielson, "Measurements and modelling of a gas-combustion infrasound source," Proc. Mtgs. Acoust. **35**, 045004 (2018).

[31] S. D. Haddad, C. T. Marks, "An experimental study of infrasound associated with passenger cars," International Journal of Vehicle Design, **10** (1), pp. 64-78 (2014).

[32] T. E. Burton, R. D. Blevins, "Vortex-shedding noise from oscillating cylinders," J. Acoust. Soc. Am. **60**, 599 (1976).

[33] D. J. Moreau, L. A. Brooks, C. J. Doolan, "On the acoustic tonal noise generation mechanism of a sharp-edged plate," J. Acoust. Soc. Am. **129**, EL 154 (2011).

[34] J. S. Lawrence, K. L. Gee, T. B. Neilsen, S. D. Sommerfeldt, "High-order estimation of active and reactive acoustic intensity," Proc. Mtgs. Acoust. **30**, 055004 (2017).

[35] E. B. Whiting, J. S. Lawrence, K. L. Gee, T. B. Neilsen and S. D. Sommerfeldt, "Bias errors analysis for phase and amplitude gradient estimation of acoustic intensity and specific acoustic impedance," J. Acoust. Soc. Am. 142, 2208-2018 (2017).

[36] National Academies of Sciences, Engineering, and Medicine. 2020. "Commercial Space Operations Noise and Sonic Boom Measurements". Washington, DC: The National Academies Press. https://doi.org/10.17226/25834.

[37] K. L. Gee, D. J. Novakovich, L. T. Mathews, M. C. Anderson, R. D. Rasband, "Development of a Weather-Robust Ground-Based System for Sonic Boom Measurements," NASA/CR-2020-5001870.

[38] K. L. Gee, E. B. Whiting, T. B. Neilsen, M. M. James, A. R. Salton, "Development of a Near-field Intensity Measurement Capability for Static Rocket Firings," Trans. JSASS Aerospace Tech. Japan, **14**, No. ISTS30, pp. Po_2_9-Po_2_15, 2016.

[39] NASA SP-8072, "Acoustic loads generated by the propulsion system," 1971.

[40] R. D. Rasband, K. L. Gee, T. B. Gabrielson, A. Loubeau, "Employing digital pole-shift filters to improve low-frequency response of sonic boom measurements," J. Acoust. Soc. Am. Submitted (2021).

[41] M. R. Cook, K. L. Gee, S. D. Sommerfeldt, T. D. Neilsen, "Coherent-based phase unwrapping for broadband acoustic signals," Proc. Mtgs. Acoust. **30**, 055005 (2017).